

AD-A076 622

ILLINOIS UNIV AT URBANA-CHAMPAIGN DEPT OF ELECTRICAL --ETC F/6 20/14
STUDIES OF EQUATORIAL SCINTILLATION PROBLEMS.(U)

SEP 79 K C YEH , C H LIU

DAA629-76-6-0286

UNCLASSIFIED

UILU-ENG-79-2559

ARO-14260.8-ELX

NL

1 OF 3

AD
A076622



AD A 076622

ARO 14260.8-ELX

Technical Report No. 65
UIIU-ENG-79-2559

LEVEL

12

STUDIES OF EQUATORIAL SCINTILLATION PROBLEMS

by

K. C. Yeh and C. H. Liu



September 1979

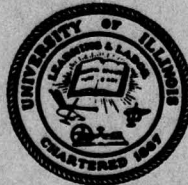
Final Report

This document has been approved
for public release and sale; its
distribution is unlimited.

Sponsored by

U.S. Army Research Office
P.O. Box 12211
Research Triangle Park, N.C. 27709

DAAG 29-76-G-0286
DAAG 29-78-G-0101



Ionosphere Radio Laboratory
Department of Electrical Engineering
University of Illinois at Urbana-Champaign
61801

DDC FILE COPY

79 11 07 068

UNCLASSIFIED

SECURITY CLASSIFICATION OF THIS PAGE (When Data Entered)

REPORT DOCUMENTATION PAGE		READ INSTRUCTIONS BEFORE COMPLETING FORM
1. REPORT NUMBER	2. GOVT ACCESSION NO. <u>14</u>	3. RECIPIENT'S CATALOG NUMBER <u>UILU-ENG-79-2559, 71A-65</u>
4. TITLE (and Subtitle) <u>Studies of Equatorial Scintillation Problems.</u>	5. TYPE OF REPORT <u>Final Report</u> June 21, 1976-Sept. 30, 1979	
7. AUTHOR(s) <u>K. C. Yeh and C. H. Liu</u>	6. PERFORMING ORG. REPORT NUMBER	
9. PERFORMING ORGANIZATION NAME AND ADDRESS Department of Electrical Engineering University of Illinois at Urbana-Champaign Urbana, IL. 61801	10. PROGRAM ELEMENT, PROJECT, TASK AREA & WORK UNIT NUMBERS <u>12 235</u>	
11. CONTROLLING OFFICE NAME AND ADDRESS U.S. Army Research Office P.O. Box 12211 Research Triangle Park, N.C. 27709	12. REPORT DATE <u>Sept 1979</u>	
14. MONITORING AGENCY NAME & ADDRESS (if different from Controlling Office) <u>ARO</u> <u>14260.7-ELT</u>	13. NUMBER OF PAGES 62	
15. SECURITY CLASS. (of this report) UNCLASSIFIED		15a. DECLASSIFICATION DOWNGRADING SCHEDULE
16. DISTRIBUTION STATEMENT (of this Report) Approved for public release; distribution unlimited.		
17. DISTRIBUTION STATEMENT (of the abstract entered in Block 20, if different from Report) <u>Final rept. 21 Jun 76 - 30 Sep 79</u>		
18. SUPPLEMENTARY NOTES THE VIEW, OPINIONS, AND/OR FINDINGS CONTAINED IN THIS REPORT ARE THOSE OF THE AUTHOR(S) AND SHOULD NOT BE CONSTRUED AS AN OFFICIAL DEPARTMENT OF THE ARMY POSITION, POLICY, OR DECISION, UNLESS SO DESIGNATED BY OTHER DOCUMENTATION.		
19. KEY WORDS (Continue on reverse side if necessary and identify by block number) Digital Data Logging System Equatorial Scintillation Ionospheric Bubbles		
20. ABSTRACT (Continue on reverse side if necessary and identify by block number) This report describes the experimental set-up, observations and results of satellite radio signals received at an equatorial station. The effects of dispersion and scattering of a pulse propagating through the ionosphere are also investigated theoretically.		

DD FORM 1 JAN 73 1473

EDITION OF 1 NOV 65 IS OBSOLETE

UNCLASSIFIED

SECURITY CLASSIFICATION OF THIS PAGE (When Data Entered)

176 009

TABLE OF CONTENTS

	Page
1. Introduction	1
2. Equipment Development.	3
2.1 Digital Data Logging System	3
2.2 Receivers	4
2.3 Data Retrieval and Processing System.	5
3. Station Operation.	6
4. Scientific Findings.	8
4.1 Equatorial ionospheric bubbles and their relations to scintillations	8
4.2 Drift speeds of equatorial irregularities	9
4.3 Theoretical study of the effects due to random scattering in the ionosphere on radio communication and ranging systems	10
5. Personnel.	11
6. Publication List	12
7. Appendix	14
A. "Pulse delay and pulse distortion by random scattering in the ionosphere", by K. C. Yeh and C. H. Liu.	
B. "Mean arrival time and mean pulse width of signals propagating through an inhomogeneous ionosphere with random irregularities", by Y. K. Wong, K. C. Yeh and C. H. Liu.	
C. "Ionospheric bubbles observed by the Faraday rotation method at Natal, Brazil", by K. C. Yeh, H. Soicher, C. H. Liu and E. Bonelli.	
D. "Ionospheric effects on radio communication and ranging pulses", by K. C. Yeh and C. H. Liu.	
E. "Scintillation observations at Natal", by K. C. Yeh, J. P. Mullen, J. R. Medeiros, R. F. da Silva and R. T. Medeiros.	
F. "Observations of equatorial ionospheric bubbles by the radio propagation method", by K. C. Yeh, H. Soicher and C. H. Liu.	

Appendix cont.

- G. "Implementation of an L-band and C-band receivers",
by Y. P. Wei.
- H. "A computer scheme for studying scintillation
observations at Natal", by S. J. Meros.

Accession For	
NTIS GRA&I	<input checked="checked" type="checkbox"/>
DDC TAB	<input type="checkbox"/>
Unannounced	<input type="checkbox"/>
Justification	
By _____	
Distribution/	
Availability Codes	
Dist	Availand/or special
A	

1. Introduction

This project is concerned with the study of scintillations of transionospheric radio signals at a number of radio frequencies, up to GHz frequencies. A suitable geostationary satellite that can provide the desired transmissions is ATS-6. This satellite has a Radio Beacon Experiment on board, which together with the Satellite Instructional Television Experiment and Millimeter Wave Propagation Experiment can provide transmissions in a number of bands, from VHF through UHF to L- and C-bands. At the time of proposal writing NASA intended to reposition ATS-6 in June 1976 at 105°W longitude and consequently Natal, Brazil (35.23°W, 5.85°S) was proposed as a site for making these observations. Later, NASA decided to move ATS-6's parking orbit further west to 140°W longitude which would be below the horizon when viewed from Natal. Obviously because of this change the experiment in the originally proposed mode could not be carried out. After close consultation with Dr. Haim Soicher of U.S. Army Communications Research and Development Command and weighing various technical and logistic factors, it was finally decided to stay at Natal but to select a different satellite. The satellite selected was Marisat 1 (15.4°W) which transmits circularly polarized signals at 257.55, 1541.5, 3945.5 MHz and a number of other frequencies. Since these frequencies are different from those transmitted by ATS-6, all the receivers had to be re-designed.

In the following we report the equipment developed for the project in section 2, the field station operation in section 3, the major scientific findings in section 4, and other housekeeping information in succeeding sections. The detailed technical findings and experimental results have been reported in several papers and these are attached in the Appendix.

2. Equipment Development

Several pieces of equipment have been developed specifically for the project. They include the digital data logging system, UHF, L-band and C-band receivers, and the digital data processing system. They are discussed in the following.

2.1 Digital Data Logging System

It has been recognized that in scintillation studies it is desirable to obtain data both in analog form on chart records and in digital form on magnetic tapes. The reason is that the chart records can provide a visual presentation of data which will facilitate morphological studies and help to locate a specific and particularly interesting piece of data for detailed analysis. On the other hand, analysis of scintillation data invariably involve statistical computations such as correlations and spectra which are most convenient to be carried out if the data are given in digital form. Therefore, it was decided to run the chart recorder on a fairly continuous basis for studies of long term behavior and to run the digital system on a chosen schedule for detailed statistical analysis.

A digital data logging system was designed and built in the Laboratory. The system is capable of recording up to 8 channels of input data at a selectable sampling rate of 1, 20, 50 or 100 Hz. This system has been described in detail in a technical report "A multi-channel digital data logging system for ionospheric scintillation studies" by

K. S. Yang and A. L. Hearn published in 1977 and will not be repeated here; interested readers should consult that report for details.

2.2 Receivers

In a previous grant from NASA we have in the Laboratory many Magnavox model "B" receivers which are no longer in use. With change of a crystal and adjustment of tank circuits these receivers can be tuned to an input frequency of 20 to 50 MHz with a bandwidth of 2.5 KHz. The sensitivity of the receiver is -135 dBm and the overall gain is 130 dB. Therefore, in all our receiver designs we have used the model "B" as the backend. The three receivers designed and constructed are the UHF receiver at 257.55 MHz, the L-band receiver at 1541.5 MHz and the C-band receiver at 3945.5 MHz.

For UHF frequency, a helix antenna to receive the right circular polarization is used. The antenna gain is approximately 10 dB. After pre-amplification, the signal is down-converted to a lower frequency that can be accepted by model "B". The expected over all signal-to-noise ratio is about 20 dB which seems to be in agreement with the operational value.

The receivers for the L-band and C-band are naturally more complicated. At L-band, the incoming signal is mixed with a crystal controlled local oscillator at 1430 MHz and then mixed again with 102.14286 MHz to produce a frequency of 9.35714 MHz as an input to the model "B". At C-band, we

are concerned with the problem of frequency stability. For this purpose all frequencies are derived from the oven controlled 10 Mhz reference oscillator (HP Model 10544 A) and the receiver is considerably more complicated. The detailed descriptions of these receivers can be found in Appendix G and will not be repeated here.

2.3 Data Retrieval and Processing System

The received data are recorded on chart recorder in analog form and on 7 inch audio magnetic tape in digital form. The analog data are generally scaled by hand for scintillation index, the rate of scintillation and the drift speed. The digital data must be retrieved through an interface circuits to a computer for later processing. Central to our data retrieval and processing system is the HP 9825A calculator. An interface network has been built, which can retrieve the scintillation data and store the data in the internal memory of the calculator or on the tape cartridge. Computer softwares have been written to error detect and correct for any data dropouts and to carry out statistical computations such as autocorrelation function, cross correlation function, power spectrum and S_4 scintillation index. A detailed write-up of the system as well as some sample computations can be found in Appendix H.

3. Station Operation

Initially, the equipment in three boxes was flown from Washington, D.C. to Natal, Brazil by the Brazilian Air Force in mid-1977. Immediately after the arrival of the equipment, Dr. Allen Hearn flew to Natal to set up the experiment in July 1977. It was then decided to set up our station in a second floor room of the Departamento de Fisica Teorica e Experimental, Centro de Ciencias Exatas, Universidade Federal do Rio Grande do Norte, Natal, Brazil. Both the UHF helix antenna and the 6-ft. parabolic reflector were installed outside of the building. Approximately 278 meters to the East (actually in a direction of 78° east of geographic north or 99.5° east of geomagnetic north) the U.S. Air Force has equipment to record satellite signals using a 30-ft. reflector. A cable was installed that transmitted the 257.55 MHz scintillation signals received by the Air Force equipment to be recorded on the same recorder as our signal for later comparisons. Such comparisons through cross-correlation analysis can yield information such as drift velocity.

The station was visited again in March 1978 and October 1978, each time for one to two weeks, to bring in new supplies and new equipment and to discuss experiment with the local personnel. Currently the station is recording scintillation signals at 257.55 MHz at two stations and the L-band signal at 1541.5 MHz. Additionally, since October a U.S. Army polarimeter has been installed. The device has been providing the

polarization rotation measurements. Once all these data are collected and accumulated to a certain degree, Prof. Bonnelli of UFRN sends them to Illinois by air mail. The received data are being scaled and processed. Some of these results have been incorporated into several papers. These are reprinted in the Appendix.

4. Scientific Findings

In this section we summarize the principle scientific results of this project. The details can be found in the Appendices.

4.1 Equatorial ionospheric bubbles and their relations to scintillations

Recently, there are increasing number of experimental evidences indicating that ionospheric perturbations described variously as ionization depletions, bubbles, plumes, etc. occur in the evening hours at the magnetic equator. There are also indications that the occurrence of these bubbles are correlated with the onset of scintillations. Theoretical studies show that the under-side of the ionosphere is subjected to Rayleigh-Taylor type of instabilities which will cause a region of depleted ionization to rise as bubbles. Sharp gradients may exist in the bubbles forming what are described as the ionization walls. When such regions are traversed by a probing radio wave, the associated Faraday effect is expected to show depletions of electron content. At the same time, the amplitude of the wave will fluctuate if there are related scintillations. By monitoring signals transmitted by the geostationary satellite MARISAT 1 and SMS 1 at the station in Natal, Brazil, we have observed the occurrence of these bubbles and studied their statistical characteristics and relations to scintillations. It is found that the most probably content depletions for the propagation

path under study have values in the range 1 to 4×10^{16} electrons per meter², but depletions as large as 1.2×10^{17} electrons per meter² have also been observed. The average durations for each observed bubble may vary from less than 2 minutes to over 30 minutes with an average of 8 minutes. There is a high correlation between the occurrence of bubbles and high UHF scintillation activities, especially in the early evening part of the activities. The data further show that the scintillation rate may increase suddenly when the bubbles either form along or drift across the propagation path. The observed phenomena suggest strongly the existence of these bubbles and their close relations to scintillations. Simultaneous UHF and L-band recordings are used in our efforts to interpret the experimental data. The results have been written up as two papers (Appendices C and F).

4.2 Drift speeds of equatorial irregularities

As stated in section 3, spaced receiver scintillation observations were performed at the Natal station. The signal from MARISAT 1 at 257.55 MHz were recorded at two receivers spaced on a 278 meter baseline. During the period 27 February to 13 March 1978, night time scintillations were observed on 10 of the 15 nights with signal fluctuations commonly exceeding 20 dB peak to peak. The spaced receiver data yield eastward irregularity velocities of approximately 30~ 150 m/s during the night time hours. The fading rates observed ranged

from 1 per second to 6 per minute. The results have been written as a paper (Appendix E). More data are available for investigations of the statistics of the drift speeds.

4.3 Theoretical study of the effects due to random scattering in the ionosphere on radio communication and ranging systems

Using the newly developed "temporal moments" method, the combined dispersive and scattering effects on radio pulses in the ionosphere are investigated. In particular, the mean arrival time and the root mean square pulse width are derived for various ionospheric conditions. It is found that under strong scintillation conditions, the scattering effects may be very important in broadening the pulses. The results are included in Appendices A, B and D.

5. Personnel

At various times the following people have worked on the project.

K. C. Yeh, Principal Investigator

C. H. Liu, Co-Principal Investigator

A. L. Hearn, Research Associate

K. S. Yang, Senior Research Engineer

S. J. Meros, Research Assistant

Y. P. Wei, Research Assistant

As a result of their work supported by this project Y. P. Wei received his M.S. degree in December 1978 and S. J. Meros received his M.S. degree in June 1979.

6. Publication List

K. S. Yang and A. L. Hearn, "A multi-channel digital data logging system for ionospheric scintillation studies". Technical Report No. 61, Ionosphere Radio Laboratory, Department of Electrical Engineering, University of Illinois, July 1977.

K. C. Yeh and C. H. Liu, "Pulse delay and pulse distortion by random scattering in the ionosphere". AGARD Conference Proceedings No.244 on "Aspects of Electromagnetic Wave Scattering in Radio Communications", pp.9-1 to 9-7, 1978.

Y. K. Wong, K. C. Yeh and C. H. Liu, "Mean arrival time and mean pulse width of signals propagating through an inhomogeneous ionosphere with random irregularities". In "Effects of the Ionosphere on Space and Terrestrial Systems" edited by J. M. Goodman, pp.470-478, 1978.

K. C. Yeh, H. Soicher, C. H. Liu and E. Bonelli, "Ionospheric bubbles observed by the Faraday rotation method at Natal, Brazil". Geophysical Research Letters, vol. 6, 473-475, June 1979.

K. C. Yeh and C. H. Liu, "Ionospheric effects on radio communication and ranging pulses". To appear in IEEE Transactions on Antennas and Propagation.

K. C. Yeh, J. P. Mullen, J. R. Medeiros, R. F. daSilva and R. T. Medeiros, "Scintillation observations at Natal". Submitted to Revista Brasileira de Fisica.

K. C. Yeh, H. Soicher and C. H. Liu, "Observations of equatorial ionospheric bubbles by the radio propagation method". To appear in Journal of Geophysical Research.

Y. P. Wei, "Implementation of an L-band and C-band receivers". M.S. thesis.

S. J. Meros, "A computer scheme for studying scintillation observations at Natal". M.S. thesis.

With the exception of the first publication which appeared as a technical report all others are reprinted in the Appendix.

Appendix A

AGARD

ADVISORY GROUP FOR AEROSPACE RESEARCH & DEVELOPMENT

7 RUE ANCELLE 92200 NEUILLY SUR SEINE FRANCE

Paper Reprinted from
Conference Proceedings No. 244
Aspects of Electromagnetic Wave
Scattering in Radio Communications

NORTH ATLANTIC TREATY ORGANIZATION



9.

PULSE DELAY AND PULSE DISTORTION BY RANDOM
SCATTERING IN THE IONOSPHERE

K. C. Yeh and C. H. Liu
Department of Electrical Engineering
University of Illinois at Urbana-Champaign
Urbana, Illinois 61801

SUMMARY

The dispersive effects of the ionosphere on propagating electromagnetic pulses are well known. Because of the frequency dependence of the refractive index, the speed of the propagation is given by the group velocity which is slower than the free-space velocity of light. The dispersion also affects the pulse shape by smearing and lengthening it, resulting in general degradation of the communication signal. However, the ionosphere has often been found to be permeated with random irregularities of electron density. Through scattering from these irregularities additional distortion of the signal may come about. The purpose of this paper is to investigate the effects of the random scattering on the pulse delay and the pulse width. This problem is mathematically formulated and solved. All multiple scattering effects are taken into account except the backscattering. The solutions are given in terms of many parameters which can be classified into three kinds: signal parameters, ionospheric parameters and irregularity parameters. It is found that under certain conditions effects caused by random scattering can be more important than those caused by dispersion. Various numerical examples will be given to show the importance of the effects. The implication on precise ranging systems and communication systems will be discussed.

Additional factors must be considered when the signal is weak and must therefore compete against the noise. The effect of noise on the determination of the arrival time is to introduce an error which depends on the signal-to-noise ratio. Its effect on the pulse width depends on a number of parameters. The nature of this dependence will be discussed.

1. INTRODUCTION

The dispersive effects of the ionospheric plasma on propagation of electromagnetic pulses is well known. For a narrow band pulse the transit time between two fixed points is determined by the group velocity which is slower than the free-space speed of light. That is, for a fixed distance the pulse will take longer time to arrive at the receiver than that in free-space. The excess, known as the excess time delay, is proportional to the integrated electron density along the path or electron content in the high frequency approximation. The effect of finite bandwidth has also been looked into; it contributes to pulse distortion and lengthening.

In addition to dispersion, the ionospheric plasma is often found in the turbulent state. The electrons form density irregularities. These irregularities can scatter electromagnetic energy and result in further degradation of radio signals propagating through the ionosphere. The purpose of this paper is to investigate the combined effects on electromagnetic pulses caused by dispersion and scattering. We first review the propagation geometry and the range of parameters involved in section 2. Next we introduce in section 3 the temporal moments and show how they are related to the mean arrival time and the mean pulse width. Also shown in section 3 are expressions and numerical values and curves for the mean arrival time and the mean pulse width. These expressions are derived for the ideal, noiseless communication channel. If there is present noise uncorrelated with the signal these quantities must be modified. This is discussed in section 4. The paper is concluded in section 5.

2. PROPAGATION GEOMETRY AND PARAMETERS

The propagation geometry is shown in Fig. 1. A plane wave signal is supposed to be impressed on top of a slab containing electron density irregularities. Scattering takes place inside the slab so that random perturbations are imparted on the wave when it leaves the base of the slab. These random perturbations are further randomized in the homogeneous region below the slab through diffractive effects before it is finally received.

In a problem such as this there are many parameters involved. In the following is a list of nine parameters and their approximate range of values pertinent to the ionosphere.

carrier frequency of the signal f : 100 - 5000 MHz
signal bandwidth (Hz) Δf : less than 10 MHz
plasma frequency f_p : 2 - 15 MHz

propagation distance z : 100 - 1000 km
 rms electron density fluctuations σ_N : 0 - 0.5
 slab thickness L : 10 - 500 km
 power law spectral exponent m : approximately 2
 inner scale r_i : 10^{-3} - 10^2 m
 outer scale r_o : 10^4 - 10^5 m

In the above list the first two parameters are signal parameters, the next two are ionospheric parameters and the last five are all irregularity parameters. The carrier frequency of the signal can of course vary over a wide range. For frequencies near the lower end of VHF band the ray bending, which is ignored in this paper, may be very important. Therefore, the lower bound of carrier frequency is taken as 100 MHz. When the frequency is raised to the SHF band, the ionospheric effects are expected to become very minimal and hence an upper bound of 5 GHz is chosen. The second parameter in the above list is the signal bandwidth which is defined by the equation

$$\sqrt{B} = (2\pi)^{-1} \int_{-\infty}^{\infty} |F(2\pi\nu)|^2 \nu^2 d\nu \quad (1)$$

where F is the spectrum of the transmitted signal as a function of the modulation frequency ν . For a Gaussian signal spectrum of the form

$$F(2\pi\nu) = (2\sigma^2/\pi)^{-1/2} \exp(-2\nu^2/\sigma^2) \quad (2)$$

the bandwidth (1) can be computed to be

$$\sqrt{B} = \sigma^2/\sqrt{\pi} \quad (3)$$

The value of the bandwidth can vary from 0, which corresponds to a pure carrier, to about 10 MHz. For most computations a value of 1 MHz is used. The third parameter f_0 is an ionospheric parameter. In the actual ionosphere the plasma frequency varies with height. For theoretical convenience the model ionosphere is assumed to have a constant plasma frequency. This is partially justified because very often irregularities are observed to be confined to a slab and because even when irregularities are distributed those near the ionization peak are most effective in producing scintillation. The plasma frequency at the peak can vary from 2 to 15 MHz, a value of 10 MHz is used in computations. The parameter, propagation distance, is the distance from the top of the irregularity slab to the receiver as shown in Fig. 1. It has the minimum value of 100 km if irregularities are in the E region. Irregularities in the magnetosphere have been observed but they are not expected to affect transionospheric propagation signals because of their low density. Therefore, an approximate maximum value of 1000 km for the propagation distance is chosen. The rms electron density fluctuations had always been thought to be small, no more than 10 from the background, until the in situ measurements demonstrated that a surprisingly large percentage of 20 or even 50 is possible at the equator. This accounts for the rather large upper bound value of 0.5 for σ_N in the list. Based on radar data, the slab in which irregularities are confined can be as thin as 10 km and as thick as several hundred kilometers. Both scintillation measurements and in situ measurements indicate the one-dimensional power spectrum of density fluctuations has the form κ^{-m} where κ is the spatial wave number. The exponent m in the power-law spectrum is approximately 2. A power-law spectrum of the form κ^{-m} has several mathematical difficulties. For example, some spectral moments will fail to exist. These difficulties can be remedied by introducing the inner scale and the outer scale. The exact values of the inner scale and the outer scale are very uncertain at present. Based on plasma physics we would expect the inner scale to be bounded below by the Debye length below which the plasma is expected to lose all its collective behavior. Therefore, the absolute lower bound is the Debye length which in the ionosphere is approximately 10^{-3} m. Based on the radar backscatter data the irregularities at 1 m length seem to belong to the same process responsible to scintillation (Morse et al., 1977). However, the more powerful Arecibo radar does not seem to have reported the spread-F type irregularities of size 0.35 m. Consequently a more reasonable value for the inner scale is probably somewhere between 0.35 m and 1 m, a value very close to the ionic gyro-radius. There is very sparse information about the outer scale, a probable range is between 10 km and 100 km as indicated in the list.

3. PULSE DELAY AND PULSE WIDTH

For purposes of locating the position of a pulse and determining its pulse width, it is convenient to make use of the moment concept. Let $a(t, z)$ represent the complex amplitude of a signal and it is in general a random function of time t and position z (dependence on transverse coordinates is suppressed). Define the n th moment of the signal by

$$M^{(n)}(z) = \int_{-\infty}^{\infty} t^n a(t, z) a^*(t, z) dt \quad (4)$$

where the angular brackets are used to denote ensemble averaging. For convenience of physical interpretation the complex amplitude is assumed to be normalized so that $M(0)(z)=1$. Then, the mean time required by a pulse to propagate from $z=0$ to z is related to the first moment by

$$t_a(z) = M^{(1)}(z) - M^{(1)}(0) \quad (5)$$

The mean square pulse width centered around the mean arrival time is related to the first two moments by

$$\tau^2(z) = M^{(2)}(z) - t_a^2(z) \quad (6)$$

Higher order moments reveal skewness and concentration of the pulse and will not be dealt with in this paper.

Theoretical derivation of expressions for t_a and τ in this propagation problem can be done by solving the transport equation for the two-frequency one-position mutual coherence function. This has been done elsewhere (Yeh and Liu, 1977). Their results show that

$$t_a = t_1 + t_2 + t_3 \quad (7)$$

where

$$t_1 = z/c \sqrt{1 - f_p^2/f^2} \quad (8)$$

$$t_2 = 3f_p^2 \sqrt{z}/2f^2 c \quad (9)$$

$$t_3 = \frac{3}{2} f_p^2 L(2z-L) \ln(L/r_1) / 4f^2 c \quad (10)$$

The transit time t_1 is well-known since it is just the time required for a signal to propagate a distance z with the group velocity $c/\sqrt{1-f_p^2/f^2}$. In the high frequency approximation (i.e. $f \gg f_p$), t_1 is usually expanded and written in the form

$$t_1 = t_0 + \Delta t_1 \quad (11)$$

where $t_0 = z/c$ is the free space time delay and Δt_1 is the excess time delay due to presence of electrons. The excess time delay in the high frequency approximation is proportional to the integrated electron density or electron content and has been a quantity of interest in satellite-based navigational systems (Klobuchar, 1976). The time delay t_2 given by (9) is a correction term to t_1 when the signal has a finite bandwidth \sqrt{f} and is usually small for narrow band signals. The time delay t_3 is caused by random scattering. In order to demonstrate numerically the order of magnitude of various effects, the following model parameters are adopted.

$$\begin{aligned} \sqrt{f} &= 1 \text{ MHz} & f_p &= 10 \text{ MHz} \\ z &= 400 \text{ km} & \sigma_N &= 0.1 \\ L &= 200 \text{ km} & m &= 2 \\ r_1 &= 10^{-2} \text{ m} & \epsilon_1 &= 10^4 \text{ m} \end{aligned} \quad (12)$$

For these parameters, the free-space time delay t_0 is 1.33426 ns which is by far the largest value. The excess time delays due to electrons, finite bandwidth and random scattering are plotted as a function of frequency in Fig. 2. In a log-log plot all three curves are straight lines. The dominant contribution to the excess delay comes from the term proportional to electron content. But, for frequencies less than 100 MHz, the scattering can increase the time delay by 1 to 10 ns.

The mean square pulse width can also be derived from the transport equation for the mutual coherence function. The result is

$$\tau^2 = \tau_0^2 + \tau_1^2 + \tau_2^2 + \tau_3^2 + \tau_4^2 + \tau_5^2 \quad (13)$$

where

$$\tau_0^2 = \tau^2$$

$$\tau_1^2 = z^2 f_p^2 / f^2 c^2$$

$$\begin{aligned}
 \tau_1^2 &= f_{pN}^2 L^2 / 2f^2 c^2 & (14) \\
 \tau_2^2 &= f_{pN}^2 L(L^2 - 2Lz + 3z^2) / 12v^2 L_1 \tau_1^2 f^2 \\
 \tau_3^2 &= f_{pN}^2 L^2 (12z^2 - 16zL + 6L^2) (\ln L_1 / \tau_1)^2 / 48 L_1^2 f^2 c^2 \\
 \tau_4^2 &= f_{pN}^2 z L (2z - L) \sqrt{L} \ln(L_1 / \tau_1) / 2L_1 f^2 c^2
 \end{aligned}$$

Let the signal spectrum be Gaussian and be given by (2). The mean square pulse width of the impressed signal at $z=0$ is then

$$\tau^2(0) = 1/16v^2 \sqrt{L} \quad (15)$$

For a bandwidth of 1 MHz, τ^2 has the numerical value $6.3326 \times 10^{-15} \text{ s}^2$ or $\tau = 7.957 \times 10^{-8} \text{ s}$. It turns out that for the parameters given by (12) the dominating terms in (13) are τ_1^2 and τ_2^2 . That is, of the six terms in (13), τ_1^2 is most important for frequencies less than a certain value and τ_2^2 is most important for frequencies larger than the same value. Let the frequency at which $\tau_1^2 = \tau_2^2$ be f_0 , then

$$f_0^2 = 40 L_1^2 (L^2 - 2Lz + 3z^2) f_{pN}^2 \sqrt{L} / 3L_1 \tau_1^2 \quad (16)$$

When $f < f_0$, τ_1^2 has the largest value for which the original pulse width is very much lengthened, when $f > f_0$, τ_2^2 has the largest value, i.e. the original pulse width is substantially unchanged. For the parameters adopted in (12), f_0 is computed to be 1.46 GHz. Hence when $f < 1.46 \text{ GHz}$, the original pulse width of $7.9578 \times 10^{-8} \text{ s}$ can be very much lengthened. On the other hand, when $f > 1.46 \text{ GHz}$, the original pulse width is changed very little. It should be mentioned that τ_1 is very sensitive to the choice of an inner scale r_1 . The inner scale given in (12) is rather small. There is still question as to the validity of the forward scatter approximation in the parabolic equation method when the inner scale is so small. If, instead of 10^{-4} m , we pick $r_1 = 1 \text{ m}$ and leave other parameters in (12) unchanged, the dependence of pulse width on frequency is very much changed (see the second curve in Fig. 3). Even for such a large inner scale, the pulse width at 100 MHz is lengthened by more than one order of magnitude.

4. EFFECT OF NOISE

In the above discussion the communication channel is assumed to be noiseless. In practice the communication channel is not ideal and the signal must be competing against the noise. If the random signal and the noise are statistically independent, expressions for the mean arrival time and the mean square pulse width in the noisy environment can be derived and related to the corresponding quantities in the noiseless environment. Let the detection of the signal be gated for a duration T centered at some instant t , which is usually close to the actual arrival time of the signal. Within the gated interval, let the signal energy be S and noise energy be N . Then the mean arrival time in the noisy environment $(t_a)_N$ is related to the mean arrival time in the ideal channel t_a by (Yeh and Liu, 1977)

$$(t_a)_N = t_a + (t_s - t_a) N/S \quad (17)$$

As can be seen in (17) the error in the arrival time is proportional to the product of two terms: $t_s - t_a$ and N/S . Hence the error is minimized if the initial guess is very close to the true arrival time and/or the signal-to-noise ratio S/N is very large. The mean square pulse width in the noisy environment τ_N^2 can also be related to the mean square pulse width in the noiseless environment τ^2 by

$$\tau_N^2 = \tau^2 + [(t_s - t_a)^2 + \tau^2 / 12 - \tau^2] N/S \quad (18)$$

It is seen that the noise affects the pulse width in a more complicated way.

5. CONCLUSION

We have given analytic expressions for the mean arrival time and the mean square pulse width in (7) and (13) respectively for the propagation geometry shown in Fig. 1. Using typical ionospheric parameters, it is shown that the largest contribution to the mean arrival time is the free-space value z/c . The largest correction to the space value is probably still that proportional to the electron content. However, scattering may introduce a further delay of 1 to 10 ns for frequencies less than about 300 MHz. The pulse lengthening effect depends on the frequency f defined by (16). If $f < f_0$, the original pulse width is substantially unchanged. If $f > f_0$, the original pulse may be

very much lengthened. If it is found that f is rather sensitive to the choice of the inner scale. It should be cautioned that the forward scatter theory may become invalid if the inner scale is too small.

The effects of noise on the determination of the mean arrival time and the mean square pulse width are given by (17) and (18).

ACKNOWLEDGEMENT

This research was supported by the U.S. Army Research Office under Grant DAAG 29-76-G-0286.

REFERENCES

- Klobuchar, J. A., 1975, "Review of ionospheric time delay limitations to ranging systems". In the Geophysical Use of Satellite Beacon Observations, COSPAR Satellite Beacon Symposium edited by M. Mendillo, pp. 629-633.
- Morse, F. A., S. C. Edgar, H. C. Koons, C. J. Rice, W. J. Heikkila, J. H. Hoffman, S. A. Tinsley, J. D. Winningham, A. B. Christensen, R. F. Woodman, J. Pomalaza and N. R. Teixeira, 1977, "Equion, an equatorial ionospheric irregularity experiment", *J. Geophys. Res.*, **82**, 578-592.
- Yeh, K. C. and C. H. Liu, 1977, "An investigation of temporal moments of stochastic waves". To appear in *Radio Science*.

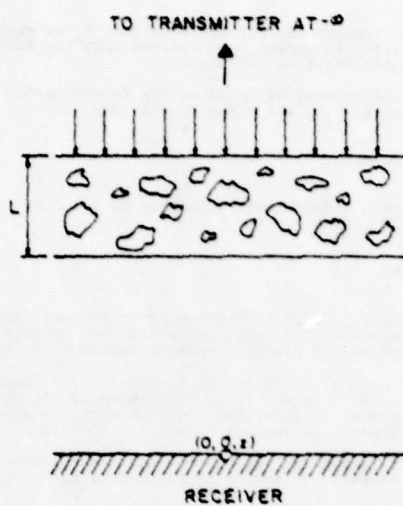


Fig. 1. The propagation geometry. The plane waves fall on top of the irregularity slab of thickness L . The randomized waves are further diffracted and received at the receiver which is a distance z from the top of the slab.

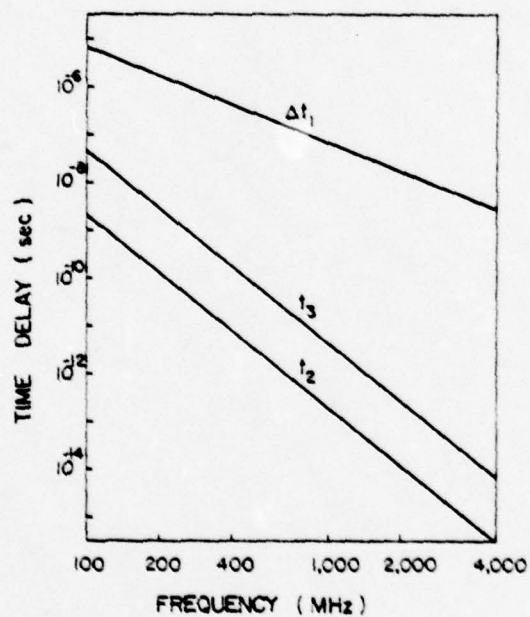


Fig. 2. Excess time delay as a function of frequency for parameters adopted in (12).

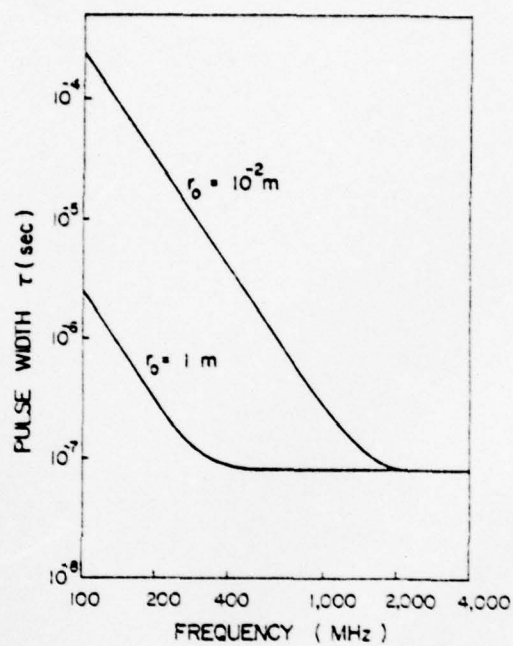


Fig. 3. Mean pulse width as a function of frequency for parameters adopted in (11) (labeled $\tau_0 = 10^{-2} \text{ m}$). When the inner scale is increased by two orders of magnitude, the behavior is shown by the curve labeled $\tau_0 = 1 \text{ m}$.

Appendix B

MEAN ARRIVAL TIME AND MEAN PULSE WIDTH OF SIGNALS PROPAGATING THROUGH AN INHOMOGENEOUS IONOSPHERE WITH RANDOM IRREGULARITIES

Y. K. Wong, K. C. Yeh and C. H. Liu

Ionosphere Radio Laboratory, Department of Electrical Engineering
University of Illinois at Urbana-Champaign
Urbana, Illinois 61801

ABSTRACT

It has been known for some time that as a dispersive medium the ionosphere will distort any radio signal propagating through it. In particular, the signal will propagate with a group velocity which is smaller than the free space velocity of light and the pulse shape will be degraded by being smeared and stretched. Recent studies of random medium propagation have demonstrated that scattering from random electron density irregularities can give rise to further degradation on signals of the kind just described. The purpose of this paper is to investigate the combined dispersive and scattering effects on radio signals in an inhomogeneous ionosphere.

The ionosphere is modeled as a slab of random irregularities imbedded in an inhomogeneous background. The background electron density is assumed to be vertically distributed with an arbitrary profile, although in actual numerical computations a Chapman profile is used. For almost all space communication applications the wave length is very small when compared with the scale height. In this case an electromagnetic pulse can be described by using the WKB solution. In many applications the precise shape of the pulse is not of great interest. Instead, a hierarchy of coarse scale descriptions will suffice. This suggests the use of temporal moments, for which the first moment is related to the mean arrival time, the second moment is related to the mean pulse width, the third moment is related to the skewness, etc. In solving for these moments the one-position two-frequency mutual coherence function appears naturally. The mutual coherence function in an inhomogeneous ionosphere is derived and solved approximately by the WKB method. The results are applied to propagation of transionospheric signals. Some numerical values will be given. They show that scattering from random irregularities can have non-negligible contribution to the arrival time and can have dominant contribution to pulse lengthening.

INTRODUCTION

As a radio signal propagates through the ionosphere, the signal is being distorted due to dispersion and scattering. The amount of distortion and its dependence on medium parameters have been studied by various authors [Liu and Yeh, 1975; Liu and Warnik, 1975; Liu et al., 1974; Ulaszek, 1974]. Their approach is adapted from the theory of wave propagation in a turbulent atmosphere (for a review see Tatarski, 1971). Central in this approach is the solution of the transport equation for the two-frequency mutual coherence function. At the same time Mark [1974] has suggested a new method of studying the characteristics of stochastic transients and transmission media by using power-moments spectra which characterize the temporal behavior of signals. Temporal moments of the stochastic wave can be derived and have also been studied by different authors [Yeh and Liu, 1977a; Yeh and Liu, 1977b; Yeh and Yang, 1977] under various conditions.

The objective of this paper is to investigate the combined effects of dispersion and random scattering on the mean arrival time and the mean pulse width of a signal propagating through an inhomogeneous ionosphere with random irregularities. These quantities have close relationship with the problems of time delay and pulse distortion. We first investigate the parabolic equation of quasi-optics [Liu et al., 1974] from which we obtain the two-frequency two-position mutual coherence functions generalized for a horizontally stratified inhomogeneous background medium. The forward scatter approximation is used to simplify the problem. The irregularity spectrum discussed here is assumed to follow a power-law as suggested by various experimental results. Equations for the mean arrival time and mean pulse width are then derived. For specific evaluation of the expressions, the background electron density is assumed to have a Chapman's profile. Using typical ionospheric parameters, some numerical results are obtained and shown in a later section.

TWO-FREQUENCY TWO-POSITION MUTUAL COHERENCE FUNCTION

The geometry of the problem of interest is shown in Fig. 1. A uniform plane wave is transmitted at $z=z_g$ and incident normally on top of a slab of random irregularities at $z=0$. Owing to the orientation of the coordinate axes z_g is actually negative. The slab of irregularities has a thickness of z_g . The wave is received, after emerging out of the slab at z_g , by a receiver located at $z=z_g$. The background electron density is not shown in the diagram but it is assumed to have a Chapman's profile with the peak at z_0 . Since the medium is the communication channel that is of interest, the effects of the transmitting and receiving antennas will not be considered.

The random electron density irregularities in the ionosphere can be mathematically characterized by taking the dielectric permittivity to be random in time and space. But to simplify the problem, the variation of the permittivity is assumed to be very slow comparing to the time that the signal will take to pass through the medium. Thus, the dielectric permittivity can be written as $\epsilon(\vec{r})$ which is a random function of position only. The permeability is taken to be uniform throughout the region of interest and equal to that in free space. The characteristic of the dielectric permittivity is described as

$$\epsilon(\vec{r}) = \epsilon_0 \langle \epsilon(\vec{r}) \rangle (1 + \mu(\vec{r})) \quad (1)$$

where

$$\langle \epsilon(\vec{r}) \rangle = 1 - \omega_p^2 / \omega^2 \quad (2)$$

$$\mu(\vec{r}) = - \frac{\omega_p^2 / \omega^2}{1 - \omega_p^2 / \omega^2} \cdot \frac{\Delta N(\vec{r})}{N(z)} \quad (3)$$

Here ω is the angular electron plasma frequency which is a function of z in our case. ϵ_0 is the vacuum permittivity and $N(z)$ denotes the background electron density which is a function of height with a typical scale height H . The percentage electron density fluctuation $\Delta N(\vec{r}) / N(z)$ is assumed to be a homogeneous random field with a typical scale size l_0 .

Starting with Maxwell's equations, assuming time dependence $e^{j\omega t}$, we can write the wave equation [Ulaszek, 1974; Yeh and Liu, 1972] for the electric field in the form

$$\nabla^2 \vec{E} + k^2 \langle \epsilon(\vec{r}) \rangle (1 + \mu(\vec{r})) \vec{E} = -\nabla [\vec{E} \cdot \nabla \ln(1 + \mu(\vec{r}))] \quad (4)$$

where $k = \omega/c$. If the irregularities are large compared to the signal wavelength, the right hand side of equation (4) can be ignored [Tatarskii, 1971]. This assumption implies that we neglect the depolarization effects of the wave. Therefore equation (4), after decoupling the cartesian components, reduces to the scalar wave equation

$$\nabla^2 E + k^2 \langle \epsilon(\vec{r}) \rangle (1 + \mu(\vec{r})) E = 0 \quad (5)$$

Let $u(\vec{r})$ denote the complex amplitude of the scalar field $E(\vec{r})$ by writing

$$E(\vec{r}) = u(\vec{r}) \exp[-jk \int_0^z \sqrt{\langle \epsilon(\zeta) \rangle} d\zeta] \quad (6)$$

Substituting (6) into (5) gives

$$\nabla^2 u - 2jk \sqrt{\langle \epsilon \rangle} \frac{\partial u}{\partial z} - jk \frac{\partial \sqrt{\langle \epsilon \rangle}}{\partial z} u + k^2 \langle \epsilon \rangle \mu \cdot u = 0 \quad (7)$$

If we assume the field is scattered into a small angular cone centered about z -axis, the forward scatter approximation can be applied [Tatarskii, 1971]. Actually, in deriving (7), the validity of the WKB solution is implicitly assumed. $\nabla^2 u$ in (7) can be replaced by the transverse Laplacian $\nabla_T^2 u$ since u is assumed to have a negligible variation in z as compared to one wavelength. Thus the complex amplitude of the time harmonic field component satisfies the so-called parabolic differential equation

$$\nabla_T^2 u - 2jk \sqrt{\langle \epsilon \rangle} \frac{\partial u}{\partial z} - jk \frac{\partial \sqrt{\langle \epsilon \rangle}}{\partial z} u + k^2 \langle \epsilon \rangle \mu u = 0 \quad (8)$$

$$\text{where } \nabla_T^2 = \frac{\partial^2}{\partial x^2} + \frac{\partial^2}{\partial y^2}.$$

In order to study the statistical properties of the signal, such as the temporal moments, rms intensity fluctuation, etc., one needs to first investigate the statistical characteristics of the complex amplitude u . In particular, the two-frequency two-position mutual coherence function Γ will be under investigation. It is defined as follows

$$\Gamma(z, |\vec{\rho}_1 - \vec{\rho}_2|, \omega_1, \omega_2) \equiv \langle u_1(z, \vec{\rho}_1, \omega_1) u_2^*(z, \vec{\rho}_2, \omega_2) \rangle \quad (9)$$

where $\langle \rangle$ denotes the ensemble average operator and an asterisk $*$ represents the complex conjugate operation. This function has a unit value for $z < 0$ since in this region the slab of random irregularities is absent. On the other hand, though the random irregularity is absent between z_g to the receiver, the function Γ does not equal to unity. This is due to the after effect as the signal passes through the slab of irregularities. This will be investigated later in the session.

The mutual coherence function Γ has been derived by some authors [Liu and Wernik, 1975; Ulaszek, 1974] but only for the homogeneous case. It is a bit more complicated when the background is inhomogeneous. From (9) we know that Γ depends only on the distance between the two points $\vec{\rho}_1 = (x_1, y_1)$ and $\vec{\rho}_2 = (x_2, y_2)$ instead of their individual position vectors owing to the assumption that the fluctuation of the electron density is a homogeneous random process

and the incident wave is uniform and plane. Let $u_1 = u(z, \rho_1, \omega_1)$ and $u_2 = u(z, \rho_2, \omega_2)$ be the signals at angular frequencies ω_1 and ω_2 and at positions (z, ρ_1) and (z, ρ_2) respectively. From (8) we write the parabolic equations for u_1 and u_2^* as

$$\frac{\partial u_1}{\partial z} + \frac{1}{2k_1 \sqrt{\epsilon_1}} \nabla_{T_1}^2 u_1 + \left(\frac{jk_1 \sqrt{\epsilon_1}}{2} \mu_1 + \frac{1}{4} \frac{\partial \ln \epsilon_1}{\partial z} \right) u_1 = 0 \quad (10)$$

$$\frac{\partial u_2^*}{\partial z} - \frac{1}{2k_2 \sqrt{\epsilon_2}} \nabla_{T_2}^2 u_2^* + \left(\frac{-jk_2 \sqrt{\epsilon_2}}{2} \mu_2 + \frac{1}{4} \frac{\partial \ln \epsilon_2}{\partial z} \right) u_2^* = 0 \quad (11)$$

If we multiply (10) by u_2^* and (11) by u_1 and add them together, it becomes

$$\frac{\partial \Gamma}{\partial z} + \Gamma Y = -\frac{1}{2} L_T Y \quad (12)$$

where

$$Y \equiv u_1 u_2^* \quad (12a)$$

$$L_T \equiv \frac{\nabla_{T_1}^2}{k_1 \sqrt{\epsilon_1}} - \frac{\nabla_{T_2}^2}{k_2 \sqrt{\epsilon_2}} \quad (12b)$$

$$Q \equiv \frac{1}{2} (k_1 \sqrt{\epsilon_1} \mu_1 - k_2 \sqrt{\epsilon_2} \mu_2) \quad (12c)$$

$$P \equiv Q + \frac{1}{4} \frac{\partial}{\partial z} (\ln \epsilon_1 - \ln \epsilon_2) \quad (12d)$$

The formal solution for (12), after taking the ensemble average, is given as

$$\begin{aligned} \langle \Gamma \rangle &= Y_0 \left[\frac{\langle \epsilon_1(0) \rangle \langle \epsilon_2(0) \rangle}{\langle \epsilon_1(z) \rangle \langle \epsilon_2(z) \rangle} \right]^{\frac{1}{4}} \\ &\cdot e^{\frac{1}{2} \int_0^z \int_0^z \langle Q(\zeta') Q(\zeta'') \rangle d\zeta' d\zeta''} \\ &- \frac{1}{2} \int_0^z \int_0^z \frac{\langle \epsilon_1(\zeta) \rangle \langle \epsilon_2(\zeta) \rangle}{\langle \epsilon_1(z) \rangle \langle \epsilon_2(z) \rangle} d\zeta \\ &\cdot e^{\frac{1}{2} \int_0^z \int_0^z \langle Q(\zeta') Q(\zeta'') \rangle d\zeta' d\zeta''} \\ &\cdot L_T \langle \Gamma \rangle d\zeta \quad (13) \end{aligned}$$

where $Y_0 = Y|_{z=0}$. Here we have assumed Q is Gaussian with zero mean. Further, we assume that the random medium is "delta-function" correlated along the direction of propagation so that Markov's assumption can be used [Tatarskii, 1971], i.e. using the approximation

$$B_N(\zeta' - \zeta'', 0) = A_N(0) \delta(\zeta' - \zeta'') \quad (14)$$

where $B_N(\vec{r})$ is the correlation function of $\Delta N/N$ which has a spectrum $\Phi_N(\vec{k})$ such that

$$A_N(\vec{\rho}) = \int_{-\infty}^{\infty} B_N(\vec{\rho}, z) dz = 2\pi \int_{-\infty}^{\infty} \Phi_N(\vec{k}_T, 0) e^{-j\vec{k}_T \cdot \vec{\rho}} d^2 k_T \quad (15)$$

$$\Phi_N(\vec{k}_T, 0) = \left(\frac{1}{2\pi} \right)^2 \iint A_N(\vec{\rho}) e^{j\vec{k}_T \cdot \vec{\rho}} d^2 \rho \quad (16)$$

and $\vec{k} = (\vec{k}_T, k_z)$. Thus, differentiating (13) with respect to z and letting $\Gamma = \langle \Gamma \rangle$ and assuming the wave is incident normally on the slab, we obtain

$$\begin{aligned} \frac{\partial \Gamma}{\partial z} + \frac{1}{2} [k_1^2 - k_p^2]^{-\frac{1}{2}} - [k_2^2 - k_p^2]^{-\frac{1}{2}} \nabla_{T_1}^2 \Gamma \\ + \left(\frac{1}{4} \frac{\partial}{\partial z} [\ln(1 - k_p^2 k_1^{-2}) (1 - k_p^2 k_2^{-2})] \right. \\ \left. + \frac{k_p^4}{8} \left[\frac{k_1^2 + k_2^2 - 2k_p^2}{(k_1^2 - k_p^2)(k_2^2 - k_p^2)} A_N(0) \right. \right. \\ \left. \left. - 2 [(k_1^2 - k_p^2)(k_2^2 - k_p^2)]^{-\frac{1}{2}} A_N(\rho) \right] \right) = 0 \quad (17) \end{aligned}$$

where $\rho = |\vec{\rho}_1 - \vec{\rho}_2|$ and $k_p = \omega_p(z)/c$. To solve for Γ in (17), let us put Γ in the following form

$$\begin{aligned} \Gamma \equiv \exp \left[- \int_0^z \frac{k_p^4}{8} \cdot \frac{(k_1^2 + k_2^2 - 2k_p^2)}{(k_1^2 - k_p^2)(k_2^2 - k_p^2)} \cdot A_N(0) d\zeta \right. \\ \left. + \frac{1}{4} \ln[(1 - k_p^2 k_1^{-2})(1 - k_p^2 k_2^{-2})] + \phi(\rho, z) \right] \quad (18) \end{aligned}$$

When we put Γ given in (18) back to (17), it will give a differential equation in terms of ϕ which looks like the following

$$\begin{aligned} \frac{\partial \phi}{\partial z} + \frac{1}{2} [k_1^2 - k_p^2]^{-\frac{1}{2}} - [k_2^2 - k_p^2]^{-\frac{1}{2}} [\nabla_{T_1}^2 \phi + (\nabla_{T_1} \phi)^2] \\ - \frac{k_p^4}{4} [(k_1^2 - k_p^2)(k_2^2 - k_p^2)]^{-\frac{1}{2}} \cdot A_N(\rho) \quad (19) \end{aligned}$$

For weak random irregularities, the non-linear term $(\nabla_{T_1} \phi)^2$ in (19) may be ignored. The resulting approximate solution is known as the Rytov's solution. With this assumption, (19) becomes

$$\frac{\partial \phi}{\partial z} + \frac{1}{2} [(k_1^2 - k_p^2)^{-\frac{1}{2}} - (k_2^2 - k_p^2)^{-\frac{1}{2}}] v_T^2 \phi = \frac{k_p^4}{4} [(k_1^2 - k_p^2)(k_2^2 - k_p^2)]^{-\frac{1}{2}} A_N(\rho) \quad (20)$$

To solve (20), we introduce a new two-dimensional Fourier transform

$$\psi(\vec{\kappa}_T, z) = \left(\frac{1}{2\pi}\right)^2 \iint_{-\infty}^{\infty} \phi(\vec{\rho}, z) e^{j\vec{\kappa}_T \cdot \vec{\rho}} d^2\rho \quad (21a)$$

$$\phi(\vec{\rho}, z) = \iint_{-\infty}^{\infty} \psi(\vec{\kappa}_T, z) e^{-j\vec{\kappa}_T \cdot \vec{\rho}} d^2\kappa_T \quad (21b)$$

Using (21b) and (15), (20) becomes

$$\frac{\partial \psi}{\partial z} - j \frac{\kappa_T^2}{2} [(k_1^2 - k_p^2)^{-\frac{1}{2}} - (k_2^2 - k_p^2)^{-\frac{1}{2}}] \psi = -\frac{k_p^4}{2} [(k_1^2 - k_p^2)(k_2^2 - k_p^2)]^{-\frac{1}{2}} \psi_N(\vec{\kappa}_T, 0) \quad (22)$$

Let us assume ψ has a form

$$\psi = W \exp\left\{j \frac{\kappa_T^2}{2} \int_0^z [(k_1^2 - k_p^2)^{-\frac{1}{2}} - (k_2^2 - k_p^2)^{-\frac{1}{2}}] d\zeta\right\} \quad (23)$$

From (22) and (23), W and ψ can be obtained and thus ϕ which is found to be

$$\phi = \frac{\pi}{2} \int_0^z k_p^4 [(k_1^2 - k_p^2)(k_2^2 - k_p^2)]^{-\frac{1}{2}} d\zeta \cdot \iint_{-\infty}^{\infty} \psi_N(\vec{\kappa}_T, 0) \exp(-j\vec{\kappa}_T \cdot \vec{\rho}) \cdot \exp\left\{j \frac{\kappa_T^2}{2} \int_0^z [(k_1^2 - k_p^2)^{-\frac{1}{2}} - (k_2^2 - k_p^2)^{-\frac{1}{2}}] d\zeta'\right\} d^2\kappa_T \quad (24)$$

Putting ϕ given in (24) back to (18) with the initial condition $\Gamma(z=0) = 1$, we obtain finally,

$$\Gamma(z, \rho, \omega_1, \omega_2) = \frac{\langle \epsilon_1(0) \epsilon_2(0) \rangle}{\langle \epsilon_1(z) \epsilon_2(z) \rangle} \frac{1}{4} \cdot \exp\left(-\frac{A_N(0)}{8} \int_0^z \frac{k_p^4 (k_1^2 - k_2^2 - 2k_p^2)}{(k_1^2 - k_p^2)(k_2^2 - k_p^2)} d\zeta\right) \cdot e^{\phi} \quad (25)$$

This is the two-frequency two-position mutual coherence function for a horizontally stratified background ionosphere under the combined WKB and Rytov approximations. This solution is valid for an observer inside the slab of random irregularities. If the observer is outside the slab as shown in Fig. 1, the solution (25) evaluated at the base of the slab ($z=z_B$) will serve as the initial condition for diffraction of waves below it. Using the same approach as shown and putting $A_N(\rho)=0$ in (20) for the absence of irregularities, Γ is obtained. It has the exact form as in (25) except the limits in ϕ are changed and is given as follows

$$\phi = \frac{\pi}{2} \int_0^{z_B} d\zeta [(k_1^2 - k_p^2)(k_2^2 - k_p^2)]^{-\frac{1}{2}} k_p^4 \cdot \iint_{-\infty}^{\infty} \psi_N(\vec{\kappa}_T, 0) \exp(-j\vec{\kappa}_T \cdot \vec{\rho}) \cdot \exp\left\{j \frac{\kappa_T^2}{2} \int_0^{z_R} [(k_1^2 - k_p^2)^{-\frac{1}{2}} - (k_2^2 - k_p^2)^{-\frac{1}{2}}] d\zeta'\right\} d^2\kappa_T \quad (26)$$

where $z_R > z_B$. The first two factors given in (25) are also changed. Instead of the variable z , it is replaced by z_R . The first factor is approximately equal to unity under high frequency approximation and it is assumed in our discussion.

It is useful to expand the mutual coherence function in a series

$$\Gamma = \Gamma_0 + \Gamma_1 \eta + \Gamma_2 \eta^2 + \dots \quad (27)$$

where $\eta = (k_1 - k_2)/k_1$ and all the Γ_i ($i=0,1,2,\dots$) are functions of k_1 only. The first three terms are obtained using the result in (25) and (26) and are given as follows

$$\Gamma_0 = 1 \quad (28a)$$

$$\Gamma_1 = j \frac{v_T^2 A_N(0)}{8k_1^3} \int_0^{z_B} k_p^4 \cdot (z_R - \zeta) d\zeta \quad (28b)$$

$$\Gamma_2 = \frac{k_1^2}{2} \left(\frac{-j v_T^2 A_N(0)}{8k_1} \right) \int_0^{z_B} k_p^4 \cdot (z_R - \zeta) d\zeta^2 + \frac{k_1^2}{2} \left(\frac{-A_N(0)}{4k_1^4} \right) \int_0^{z_B} k_p^4 d\zeta + \frac{v_T^2 v_T^2 A_N(0)}{16k_1^6} \int_0^{z_B} k_p^4 \cdot (z_R - \zeta)^2 d\zeta + \frac{j v_T^2 A_N(0)}{2k_1^5} \int_0^{z_B} k_p^4 \cdot (z_R - \zeta) d\zeta \quad (28c)$$

The first term in (28c) will be neglected for its value is very small comparing to other terms in the expression under high frequency approximation. ρ is put equal to zero because the receiver is assumed to be a point.

IRREGULARITY SPECTRUM

It is shown in the previous section that the propagation of an EM-wave in a random medium is closely related to the correlation, or the spectrum, of the random field $\Delta N/N$. In the ionosphere, through many measurements, they all seem to suggest the irregularity spectrum has the spatial wave number dependence κ^{-p} , commonly referred to as a power-law spectrum. But there are a few difficulties for a 3-dimensional power spectrum of the form κ^{-p} . Firstly, for $p > 2$, its associated correlation will not exist. Secondly, for any finite value of p some spectral moments will always fail to exist. Fortunately, Shkarosky [1968] introduced an inner scale r_0 along with the outer scale l_0 , introduced by Tatarskii [1971] to remove the difficulties by writing the spectrum as

$$\Phi_N(\kappa) = \frac{[\kappa_0 r_0]^{(p-3)/2} \cdot r_0^3}{(2\pi)^{3/2} K_{(p-3)/2}(\kappa_0 r_0)} \cdot \frac{K_{p/2}(r_0 \sqrt{\kappa^2 + \kappa_0^2}) \sigma_N^2}{(r_0 \sqrt{\kappa^2 + \kappa_0^2})^{p/2}} \quad (29)$$

where $\kappa_0 = 1/l_0$ and K is a Hankel function of imaginary argument. σ_N^2 is the variance of the fluctuation function $\Delta N/N$. It has an advantage in using (29) for all the related correlation functions can be evaluated analytically.

The 2-dimensional correlation $A_N(\rho)$ defined by (15) for an isotropic random field can be expressed in the form [Yeh and Liu, 1977a]

$$A_N(\rho) = A_0 + A_2 \rho^2 + A_4 \rho^4 + \dots \quad (30)$$

Thus, using (15) and (29), the coefficients in (30) are obtained and are given as follows

$$A_0 = \sqrt{2\pi} \kappa_0 / \kappa_0 \cdot \sigma_N^2 K_{(p-2)}(\kappa_0 r_0) / K_{(p-3)/2}(\kappa_0 r_0) \quad (31a)$$

$$A_2 = -\sqrt{\pi} \kappa_0 / 2 r_0 \cdot \sigma_N^2 K_{(p-4)/2}(\kappa_0 r_0) / K_{(p-3)/2}(\kappa_0 r_0) \quad (31b)$$

$$A_4 = \sqrt{\pi} \kappa_0^3 / 2^5 r_0^3 \cdot \sigma_N^2 K_{(p-6)/2}(\kappa_0 r_0) / K_{(p-3)/2}(\kappa_0 r_0) \quad (31c)$$

MEAN ARRIVAL TIME OF SIGNALS

Let us assume the signal be a real pulse $P(z, t)$ which is a superposition of plane waves, i.e.

$$P(z, t) = \int_{-\infty}^{\infty} f(\omega) u(z, \omega) \exp\{j\omega(t - \int_z^{\infty} \sqrt{\epsilon} dz/c) + c.c.\} d\omega \quad (32)$$

where $f(\omega)$ is the amplitude spectrum and u is the complex amplitude with boundary condition $u(z_0, \omega) = 1$ and satisfies approximately the parabolic differential equation (11). The pulse enters the slab normally at $z=0$ and propagates through the random medium. It is received at a point $z=z_R$ after emerging out of the slab at $z=z_B$. For a real pulse, $f(\omega)$ and $u(z, \omega)$ must be even in ω for an isotropic medium which is assumed here. The pulse is assumed to have a narrow bandwidth, i.e. if $\omega = \omega_c + \Omega$ where ω_c is the carrier angular frequency, then $\Omega \ll \omega_c$. Hence, the pulse can then be expressed as

$$P(z, t) = A(z, t) \exp\{j(\omega_c t - k_c \int_z^{\infty} \sqrt{\epsilon} dz) + c.c.\} \quad (33)$$

where c.c. denotes the complex conjugate of the first term and the subscript c represents the corresponding parameters at the carrier frequency. The complex envelope $A(z, t)$ is given as

$$A(z, t) = \int_{-\infty}^{\infty} d\Omega g(\Omega) V(z, \Omega) \exp\{j(\Omega t - (k \int_z^{\infty} \sqrt{\epsilon} dz - k_c \int_z^{\infty} \sqrt{\epsilon_c} dz))\} \quad (34)$$

where $g(\Omega) = f(\omega_c + \Omega)$ and $V(z, \Omega) = u(z, \omega_c + \Omega)$. Since we have assumed that the bandwidth of the pulse is small, thus the function $g(\Omega)$ is sharply peaked at $\Omega=0$. Therefore the limits of the integral in (34) can be extended from $-\infty$ to ∞ as shown.

Now, let us define the n^{th} temporal moment by the equation

$$M^{(n)}(z) \equiv \int_{-\infty}^{\infty} \langle A^*(z, t) t^n A(z, t) \rangle dt \quad (35)$$

where $n=0, 1, 2, \dots$. This definition has been used in computations of quantum mechanical packets [Baird, 1972], in studies of wave dispersion [Anderson and Askne, 1974] and in calculating the spatial fluctuations of a light beam [Kon et al., 1974]. The ensemble average operator is present in (35) because A is random. When the expression (34) for A is substituted in (35) one can tell that the mutual coherence function will appear naturally.

We note from (35) that the zeroth temporal moment $M^{(0)}(z)$ is just the energy in the pulse.

Under the forward scatter approximation it can be shown that $M^{(0)}(z)$ equals to constant, i.e. the total energy in the pulse is conserved. In this case it is convenient to let $M^{(0)}(z)=1$. For the time reference, it is convenient to set $M^{(1)}(z_S)=0$ which means that a pulse is emitted at the sending end z_S when $t=0$. In general, $M^{(1)}(z_S)$ is not equal to zero but only if the impressed signal has a real symmetric envelope, i.e. $A(z_S, t) = A(z_S, -t) = A^*(z_S, t)$. This implies that $g(\Omega)$ must be real and even in Ω . For simplification, such a symmetric envelope is assumed. For general pulses, $M^{(1)}(z_S)$ must be subtracted out in order to establish the time origin.

Having all these assumptions, the mean arrival time is given by

$$t_a(z_R, z_S) = M^{(1)}(z_R) = \int_{-\infty}^{\infty} \langle A^*(z_R, t) t A(z_R, t) \rangle dt \quad (36)$$

Putting $A(z, t)$ given by (34) into (36) and using the results from last section, we obtain

$$t_a(z_R, z_S) = \frac{(z_R - z_S)}{c} + \Delta t + t_1 + t_2 \quad (37)$$

where

$$\Delta t = \frac{1}{2ck_c^2} \int_{z_S}^{z_R} k_p^2 \cdot (1 + \frac{3}{4} \cdot \frac{k_p^2}{k_c^2}) dz \quad (37a)$$

$$t_1 = \frac{3}{4ck_c^2} \cdot \frac{\bar{\Omega}^2}{\omega_c^2} \cdot \int_{z_S}^{z_R} k_p^2 \cdot (2 + 5 \frac{k_p^2}{k_c^2}) dz \quad (37b)$$

$$t_2 = \frac{-A_2}{2ck_c^4} \int_0^{z_B} k_p^4 \cdot (z_R - \zeta) d\zeta \quad (37c)$$

$\bar{\Omega}^2$ is called the mean square bandwidth of the signal and is defined as

$$\bar{\Omega}^2 \equiv 2\pi \int_{-\infty}^{\infty} g(\Omega) g^*(\Omega) \Omega^2 d\Omega \quad (38)$$

If the receiver is inside the random medium, (37) is modified to have different limits. The contributions to the mean arrival time in (37) are contained in four terms. The first term represents the time required for the signal to propagate a distance $z_R - z_S$ in free space. The second term Δt is a correction factor to the first term due to the dispersive characteristics of the medium. The third term t_1 is a higher order correction to the first two terms and is caused by the finite bandwidth in the signal. This t_1 is proportional to $\bar{\Omega}^2$ and the dispersive characteristics of the medium and can be called a term of higher order dispersion. For a non-dispersive medium, t_1 vanishes. The fourth term t_2 accounts for the random scattering and diffraction in the random

irregularity slab. The numerical value of A_2 in (37c) is negative and all the integrals in (37a, b, c) have positive values. Thus all these terms tend to increase the mean time of arrival of the signal.

MEAN SQUARE PULSE WIDTH

The mean square pulse width is defined as

$$\tau^2 \equiv \frac{M^{(2)}(z_R)}{M^{(0)}(z_R)} - \left[\frac{M^{(1)}(z_R)}{M^{(0)}(z_R)} \right]^2 \quad (39)$$

where $M^{(2)}(z) = \int_{-\infty}^{\infty} \langle A^*(z, t) t^2 A(z, t) \rangle dt$ and both $M^{(1)}(z_R)$ and $M^{(0)}(z_R)$ have obtained previously. The final expression for τ^2 is given by

$$\tau^2 = \tau_0^2 + \tau_1^2 + \tau_2^2 + \tau_3^2 \quad (40)$$

where

$$\tau_0^2 = M^{(2)}(z_S) \quad (40a)$$

$$\tau_1^2 = \frac{A_0}{4c^2 k_c^4} (1 + 10 \frac{\bar{\Omega}^2}{\omega_c^2}) \int_0^{z_B} k_p^4 d\zeta \quad (40b)$$

$$\tau_2^2 = \frac{4A_4}{c^2 k_c^6} (1 + 21 \frac{\bar{\Omega}^2}{\omega_c^2}) \int_0^{z_B} k_p^4 (z_R - \zeta)^2 d\zeta \quad (40c)$$

$$\tau_3^2 = \frac{1}{c^2 k_c^4} \cdot \frac{\bar{\Omega}^2}{\omega_c^2} \left[\int_{z_S}^{z_R} k_p^2 d\zeta \right]^2 \quad (40d)$$

In (40), τ_0^2 is actually the mean square pulse width of the signal at the sending end, i.e. the original pulse width of signal. τ_3^2 is a correction term which is contributed by the dispersive characteristics of the medium only. τ_1^2 and τ_2^2 are the terms that come about because of scattering from the random irregularities. There is no A_2 -term in (40) because it is negligible compared to all other terms under high frequency approximation. If we assume the signal has a Gaussian frequency spectrum where

$$g(\Omega) = (2\sigma)^{-1/2} \exp(-\Omega^2/2\sigma^2) \quad (41)$$

then $\tau_0^2 = (4\bar{\Omega}^2)^{-1}$. Out of these four terms in (40), with typical ionospheric parameters, τ_0^2 and τ_2^2 are the dominant terms. At low frequency, τ_2^2 is the largest. As the frequency increases, these two terms will have comparable values until at a much higher frequency, τ_0^2 dominates. Some numerical computations are shown in the next section.

NUMERICAL RESULTS

In this section, we are going to compute some numerical values of the mean arrival time and the mean pulse width for some typical ionospheric conditions. The background electron density is assumed to have a Chapman's profile. With the geometry shown in Fig. 1 the z-axis is pointing downward instead of the usual upward direction, the square of the plasma wave number for a Chapman layer is expressed as

$$k_p^2(z) = \frac{N_0 q^2}{c^2 m_e} \cdot \exp\left\{\frac{1}{2}\left(1 + \frac{(z-z_0)}{H} - \exp\left(\frac{z-z_0}{H}\right)\right)\right\} \quad (42)$$

where N_0 is the maximum electron density; q --the charge of an electron; m --the mass of an electron; c --the velocity of light; H --the scaled height and z_0 --the location of the peak of the electron density. The integrals in (37) and (40) can be obtained by making use of numerical analysis and a digital computer. They can also be worked out analytically.

Let us consider some typical ionospheric parameters where $N_0=10^{12} \text{ m}^{-3}$, $H=80 \text{ km}$, $p=4$, $\kappa_0=10^{-4} \text{ m}^{-1}$, $r_0=10^{-1} \text{ m}$ and $\sigma_N=0.2$. The peak of the inhomogeneous electron density is assumed to be at $z_0=0$. The distance between the satellite and receiver is usually 35,000 km and the top of the irregularity slab is about 500 km from ground having a thickness of about 100 km. Assuming the signal has a carrier frequency of 250 MHz and having $\sqrt{N^2}=2\pi \times 10 \text{ MHz}$, the mean arrival time is evaluated according to (37) which gives

$$t_a(z_R, z_S) = 0.117 + 7.095 \times 10^{-7} + 3.411 \times 10^{-9} + 4.278 \times 10^{-9} \text{ s.} \quad (43)$$

The time taken for the signal to travel that distance in free space is 0.117s. Out of the rest three correction terms, $\Delta t=7.095 \times 10^{-7} \text{ s}$ which is proportional to the total electron content is the dominant term. For the given values that are used in here, $t_2=4.278 \times 10^{-9} \text{ s}$ which is due to random scattering and diffraction in the random irregularities slab has a higher value than that correction factor $t_1=3.411 \times 10^{-9} \text{ s}$. For different set of parameter values, t_1 can be greater than t_2 where they are given in (37b) and (37c) respectively. These three correction terms are plotted in log-log scale in Fig. 2 with carrier frequency ranging from 10^2 to 10^4 MHz . They formed three straight lines and their values decrease as the carrier frequency increases. This is true because as the frequency increases, the factor $(1-\mu_p^2/\omega^2)^{1/2}$ is closer to unity. Thus, the signal seems to propagate in a medium more nearly approaching free space. But for frequencies between 100 and 200 MHz, the scattering can increase the time delay by 10 to 100 ns.

Using the same set of parameter values, the mean square pulse width is obtained as

follows

$$\tau^2 = 6.333 \times 10^{-17} + 2.744 \times 10^{-16} + 2.518 \times 10^{-11} + 1.287 \times 10^{-14} \text{ s}^2. \quad (44)$$

For frequency below 1000 MHz, τ_2^2 given by (40c) dominates the mean pulse width of the signal. When frequency is above 4000 MHz, $\tau_0^2=6.333 \times 10^{-17} \text{ s}^2$ dominates over all the others, i.e. the pulse is not being distorted much. It is found that the frequency range in which the pulse is not distorted is very sensitive to the mean square bandwidth $\bar{\omega}^2$. If instead of $\bar{\omega}^2=2\pi \times 10 \text{ MHz}$, we use $\bar{\omega}^2=2\pi \times 1 \text{ MHz}$, τ_0^2 will become $6.333 \times 10^{-15} \text{ s}^2$ and the undistorted signal frequency range will be 1500 MHz and above. Furthermore, τ_2^2 given in (40c) is very sensitive to the choice of the inner scale r_0 . In Fig. 3, the mean pulse width is plotted in log-log scale with three different values of r_0 and remaining other parameters same as those used in (44). For $r_0=0.1 \text{ m}$, it is still a question as to the validity of the forward scatter approximation in the parabolic equation method when the inner scale is so small. But even when $r_0=10 \text{ m}$, at 100 MHz, the pulse width is lengthened by more than two orders of magnitude.

CONCLUSION

In this paper, the expressions for the mean arrival time (37) and the mean square pulse width about the mean (40) for an EM pulse passing through a random irregularities slab with an inhomogeneous background electron density are derived. The model that is used is more realistic in characterizing the ionosphere. For example, the random irregularity spectrum has a power-law profile instead of a Gaussian profile used by Yeh and Yang [1977] and the background electron density is allowed to be inhomogeneous instead of homogeneous. For some typical ionospheric parameters, the greatest contribution to the correction in time delay is Δt which is proportional to the total electron content in the medium and is given in (37a). Nevertheless, the random scattering factor brings an addition of 10 to 100 ns to the time delay. Actually, the importance of the thickness of the irregularities slab is also being investigated. It only affects the values t_2 given in (37c) and it is shown in Fig. 4, using the same parameters as in (43). When $z_S > 150 \text{ km}$, t_2 does remain the same. It is reasonable because we have assumed a Chapman profile for the electron density. For some other sets of ionospheric parameters, the correction factor t_1 and t_2 can be larger and this shows that the results due to random scattering and higher order dispersion have important implications for accurate satellite based navigational and communication systems.

The pulse lengthening effect depends on the carrier frequency being used. With a

higher carrier frequency, the signal is less distorted. It is also sensitive to the inner scale value that is being assumed. Here, it should be cautioned that if the inner scale is too small, the forward scatter approximation may not be valid. Further, the mean square bandwidth of the pulse also has a great effect on the range of frequency where the signal is less distorted.

ACKNOWLEDGEMENT

This work was supported partly by the National Science Foundation under Grant ATM 75-21755 and partly by the U.S. Army Research Office under the Grant DAAG 29-76-G-0286.

REFERENCES

- Anderson, D. G. and J. I. H. Askne, "Wave packets in strongly dispersive media," *Proc. IEEE*, Vol. 62, USA, 1974, pp. 1518-1523.
- Baird, L. G., "Moments of a wave packet," *Am. J. Phys.*, Vol. 40, USA, 1972, pp. 327-329.
- Kou, A. I., V. L. Mironov and V. V. Kosov, "Fluctuations of the centers of gravity of light beams in a turbulent atmosphere," *Radiofizika*, Vol. 17, USSR, 1974, pp. 1501-1511.
- Liu, C. H. and A. W. Wernik, "A Characterization of transionospheric fading communication channel," *IEEE Trans. Commun.*, USA, July 1975, pp. 773-776.
- Liu, C. H. and K. C. Yeh, "Frequency and spatial correlation functions in a fading communication channel through the ionosphere," *Radio Sci.*, Vol. 10, 1975, pp. 1055-1061.
- Liu, C. H., A. W. Wernik and K. C. Yeh, "Propagation of pulse trains through a random medium," *IEEE Trans. Ant. Prop.*, USA, July 1974, pp. 624-627.
- Mark, W. D., "Characterization of stochastic transients and transmission media: The method of power-moments spectra," *J. of Sound and Vibration*, Vol. 22, No. 3, USA, 1972, pp. 249-295.
- Shkarofsky, I. P., "Generalized turbulence space-communication and wave-number spectrum-function pairs," *Can. J. Phys.*, Vol. 46, Canada, 1968, pp. 2133-2153.
- Tatarskii, V. I., "The effects of the turbulent atmosphere on wave propagation," U.S. Department of Commerce, National Technical Information Service, Springfield, Va., USA, 1971.
- Ulaszek, S. J., Jr., "A theoretical study of the transionospheric fading communication channel," IRL Tech. Rep. #54, University of Illinois, Urbana-Champaign, Ill., USA, 1974.
- Yeh, K. C. and C. H. Liu, "Theory of ionospheric waves," New York, USA, Academic Press, 1972.
- Yeh, K. C. and C. H. Liu, "An investigation of temporal moments of stochastic wave," *Radio Sci.*, Vol. 12, USA, 1977a, pp. 671-680.
- Yeh, K. C. and C. H. Liu, "Pulse delay and pulse distortion by random scattering in the ionosphere," presented at the AGARD EPP Symposium on Aspects of Electromagnetic Scattering in Radio Communications, Boston, USA, 3-7 Oct., 1977b.
- Yeh, K. C. and C. C. Yang, "Mean arrival time and mean pulsewidth of signals propagating through a dispersive and random medium," *IEEE Trans. Ant. Propagat.*, Vol. AP-25, No. 5, USA, 1977, pp. 710-713.

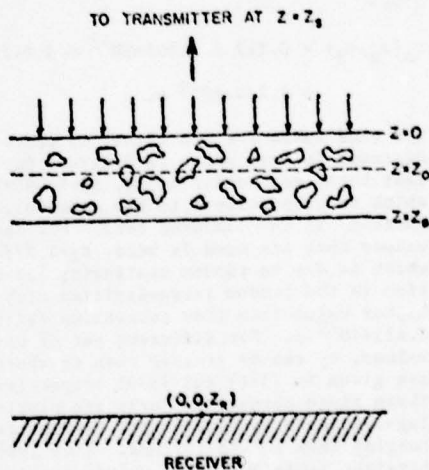


Fig. 1 The geometry of the problem. The plane wave signal is transmitted at z_g , is incident normally on top a slab containing random irregularities at $z=0$, emerges from the slab at $z=z_g$, and is received at z_r . The background ionosphere is assumed to be inhomogeneous with a peak density at $z=z_0$.

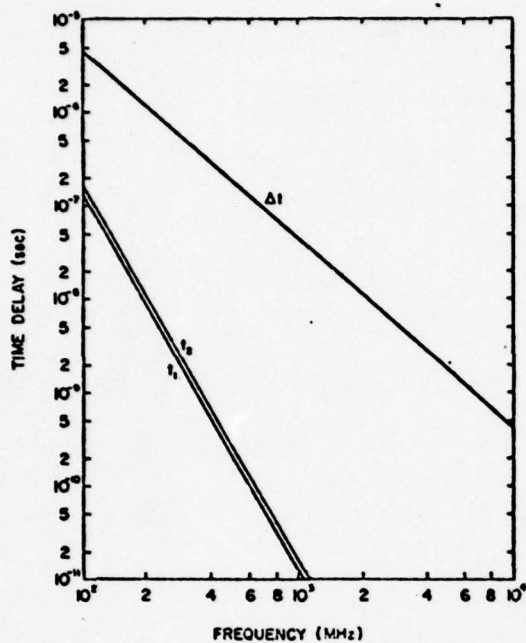


Fig. 2. Excess time delay as a function of frequency for parameters used in (43).

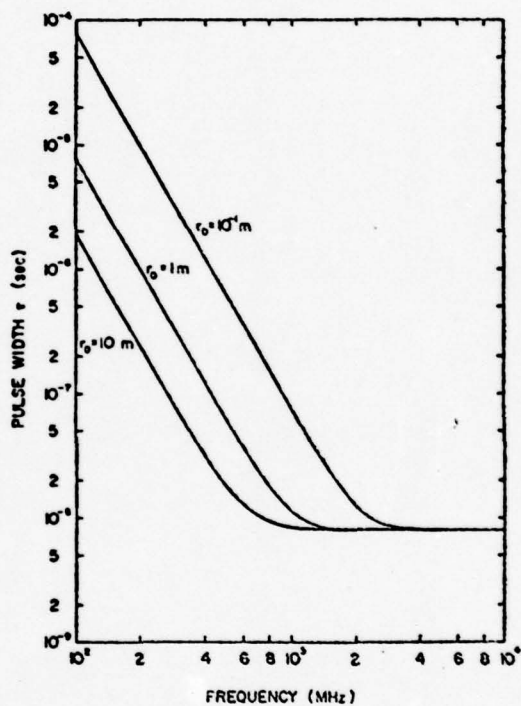
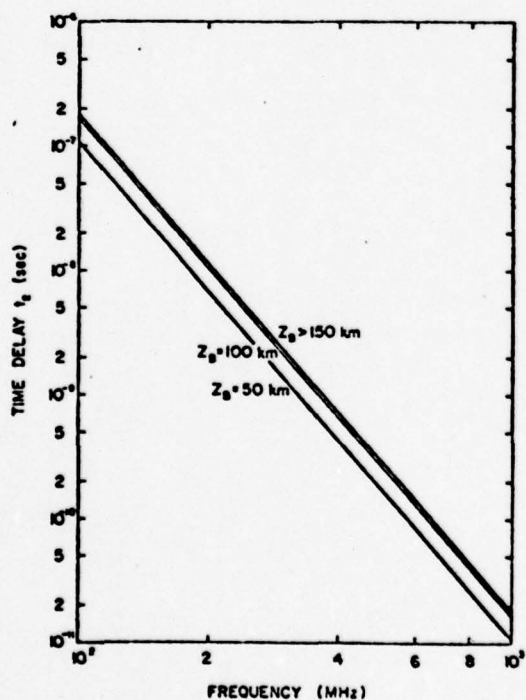


Fig. 3. Mean pulse width as a function of frequency for parameters used in (44). Three values of r_0 are used and plotted here.

Fig. 4. The time delay t_2 as a function of frequency for parameters used in (43). Three different thicknesses of slab z_0 are used and plotted here.

IONOSPHERIC BUBBLES OBSERVED BY THE FARADAY ROTATION METHOD AT NATAL, BRAZIL

K. C. Yeh¹, H. Soicher², C. H. Liu¹, E. Bonelli³¹Department of Electrical Engineering, University of Illinois, Urbana, IL 61801²Center for Communication Systems, U.S. Army Communication Research and Development Command, Ft. Monmouth, N.J. 07703³Department of Theoretical and Experimental Physics, Federal University of North Rio Grande, Natal, RN, Brazil

Abstract. By a sample record we show that the radio beacon experiments which utilize the Faraday rotation technique and the scintillation observations can be used to observe equatorial ionization bubbles. In a two-hour period 5 isolated bubbles have been identified. The depleted total electron content for one such bubble is 2.2×10^{16} electrons/m² and the east-west dimension is about 72 km. This translates to a total depletion of 1.6×10^{21} electron per meter in the north-south direction.

The purpose of this paper is to report observations of ionospheric bubbles by means of the Faraday rotation method using signals transmitted by the geostationary satellite SMS 1 at 136.379 MHz and received at Natal, Brazil (geographic coordinates 35.23°W, 5.85°S, dip -9.6°). Such bubbles have been observed at the equatorial ionosphere by a variety of experimental techniques, the most dramatic of which are radar backscatter maps [Woodman and LaHoz, 1976] and the satellite in situ measurements [McClure et al., 1977]. These results have been recently summarized [Basu and Kelley, 1979]. Theoretically the steepened underside of the ionosphere is subject to Raleigh-Taylor instability [Liu and Yeh, 1966a and b] which, when triggered, will develop nonlinearly into bubbles. The associated polarization electric field can drive these bubbles upward to form plumes [Ott, 1978; Ossakow et al., 1979]. Using the Faraday rotation technique such bubbles were inferred in observations of Koster [1976] although he did not use that terminology. More recently using the same technique as used in this paper, Klobuchar et al., [1978] have reported observations of some very large electron depletions, some even over 20% of the background, while Rino et al. [1978] using the orbiting satellite have observed many cases that show complex electron content structures but only few cases in which their data would suggest a simple depletion of electron content. Since September 1978 a polarimeter was installed, together with equipment for scintillation observations, at Natal, Brazil on the campus of Federal University of North Rio Grande. We wish to show one sample record obtained using that equipment.

Fig. 1 shows a record obtained on October 15, 1978. The time marked on the record is given in

LMT which is UT - 3 hrs. The total record length has a duration slightly less than two hours. In this 2-hour duration at least 5 isolated bubbles can be identified. Experience has shown that a bubble can be identified by a decrease in the total electron content as given by the Faraday rotation effect (shown in the lower two channels of Fig. 1) and the accompanied sudden increase in the fading rate and in most but not all cases also the increased scintillation index (shown in top channel of Fig. 1). On occasions during severe scintillations, the signal may fade into the noise level. At these times, the polarization of the received wave is of course undefined and the polarimeter will drift to any arbitrary indication. However, as soon as the signal rises above the noise, the polarization channels will return to correct indications, giving rise to sharp spikes as can be seen with fairly high frequency on the bottom channel of Fig. 1 before 0200 LMT. The examples shown in Fig. 1 occurred past the midnight and these are easier to identify because the record is usually not masked by so many spikes. Between bubbles the fading rate and usually the scintillation index are both reduced. During the period after the local sunset and midnight the scintillation can be so severe as to make positive identification difficult. The bubble that occurred at 0251 LMT depicted in Fig. 1 shows a depletion of 2.2×10^{16} electrons/m² or about 2% of the diurnal change. The duration of 8 minutes can be translated to mean an east-west dimension of 72 km since spaced station observations deduce an east-west drift of 150 m/s. These numbers indicate that the total depletion of electrons per meter in the north-south direction is about 1.6×10^{21} electrons/m. Airglow observations show large extension of the depleted region in the north-south direction to sometimes above 1200 km [Whitney et al., 1978; Weber et al., 1978]. Consequently, the implied total depletion in these bubbles can be very large indeed. It is interesting to note that large depletions have been reported as far away from the magnetic equator as São José dos Campos [Kaushika and Mendonca, 1974] at which the dip is -23.7°. However, the nature of depletions reported by them seems to be quite different from those reported here.

During the one-month period from September 18, 1978 through October 19, 1978, ninety-four such bubbles have been observed. A study of their



Fig. 1. Sample data showing occurrence of at least five isolated bubbles in a time slightly less than two hours. A linearly polarized signal at 136.379 MHz transmitted by the geostationary satellite SMS 1 parked at 90°W is received at Natal, Brazil (35.23°W, 5.85°S, Dip -9.6°). The top channel is amplitude and it is approximately linear in dB with a full scale deflection corresponding to 18dB. The lower two channels give the plane of polarization of the received wave in a ramp format with one channel displaced by 90° from the other. A full scale deflection corresponds to 180° rotation of the plane of polarization or an electron content change of 1.89×10^{17} electrons/m². The upscale change indicates a decrease in the total electron content. The time runs from left to right and hourly marks in LMT are shown. The date is October 15, 1978.

statistics and the associated scintillation observations is being undertaken and will be the subject of a forthcoming paper.

Acknowledgement. At the University of Illinois, this research was supported by the Army Research Office under grant DAAG 29-78-G-0101. We wish to thank Francis J. Gorman, Jr. for his assistance in testing and setting up the equipment in the laboratory before shipping to Brazil. The assistance of P. Kaufmann in making this experiment possible at Natal is acknowledged with pleasure.

References

- Basu, S. and M. C. Kelley, A view of recent observations of equatorial scintillation and their relationship to current theories of F-region irregularity generation. To appear in *Radio Sci.*, 1979.
- Kaushika, N. D. and F. de Mendonca, Nighttime fluctuations (scintillations) in Faraday rotation angle of VHF signals from geostationary satellites. *Planet. Space Sci.*, **22**, 1331, 1974.
- Klobuchar, J. Aarons, E. Weber, L. Lucena and M. Mendillo, Total electron content changes associated with equatorial irregularity plumes. Presented at National Radio Science Meeting, paper G4-2, 6-9 Nov. 1978, Boulder, Colorado.
- Koster, J. R., Study of the equatorial ionosphere. Report AFGL-TR-77-0165, University of Ghana, Legon, Ghana, 1976.
- Liu, C. H. and K. C. Yeh, Low-frequency waves and gradient instabilities in the ionosphere, *Phys. Fluids*, **9**, 1407, 1966a.
- Liu, C. H. and K. C. Yeh, Gradient instabilities as possible causes of irregularities in the ionosphere, *Radio Sci.*, **1**, 1283, 1966b.
- McClure, J. P., W. B. Hanson and J. H. Hoffman, Plasma bubbles and irregularities in the equatorial ionosphere, *J. Geophys. Res.*, **82**, 2650, 1977.
- Ossakow, S. L., S. T. Zalesak and B. E. McDonald, Nonlinear equatorial spread F: Dependence on altitude of the F peak and bottomside background electron density gradient scale length, *J. Geophys. Res.*, **84**, 17, 1979.
- Ossakow, S. L., A review of recent results on spread F theory. NRL Memorandum Report 3909, January 1979.
- Ott, E., Theory of Rayleigh-Taylor bubbles in the equatorial ionosphere, *J. Geophys. Res.*, **83**, 2066-2070, 1978.
- Rino, C. L., R. C. Livingston and J. Owen, The structure of equatorial gigahertz scintillation. Presented at National Radio Science Meeting, paper G4-4, 6-9 Nov. 1978, Boulder, Colorado.
- Weber, E. J., J. Buchau, R. H. Eather, and S. B. Mende, North/south aligned equatorial airglow depletions, *J. Geophys. Res.*, **83**, 712-716, 1978.
- Wernik, A. W. and C. H. Liu, Ionospheric irregularities causing scintillation of GHz frequency radio signals, *J. Atmos. Terr. Phys.*, **36**, 871-879, 1974.
- Whitney, H. E., J. Aarons and C. Malik, A proposed index of measuring ionospheric scintillations, *Planet. Space Sci.*, **17**, 1069, 1969.

Whitney, H. E., J. Aarons, J. Bachau, E. J. Weber, and J. P. McClure, The evolution of scattering equatorial F-region irregularities and resultant effects on transionospheric radio waves. AGARD Conference Proceedings No. 244, Aspects of Electromagnetic Wave Scattering in Radio Communications edited by A. N. Ince, paper 8, 1978.

Woodman, R. F. and C. LaHoz, Radar observations of F-region equatorial irregularities, J. Geophys. Res., 81, 5447, 1976.

(Received March 9, 1979;
accepted April 3, 1979.)

Appendix D

Ionospheric Effects on Radio Communication and Ranging Pulses

by

K. C. Yeh and C. H. Liu

Ionospheric Effects on Radio Communication and Ranging Pulses

K. C. Yeh and C. H. Liu
Department of Electrical Engineering
University of Illinois at Urbana-Champaign
Urbana, Illinois 61801

Abstract

Transionospheric radio pulses used for communication and ranging purposes are modified by propagation effects arising from dispersion and scattering. To describe these effects quantitatively, it is convenient to use the concept of temporal moments. The zeroth temporal moment is proportional to energy flow in the wave and is constant in a dissipationless ionosphere under the forward scatter approximation. The first temporal moment is related to the mean arrival time which can be arranged as a series consisting of terms proportional to f_c^{-2n} , $n=0,1,2, \dots$, where f_c is the carrier frequency. Here the $n=0$ term in this series representation of the first temporal moment is just the free-space transit time which can be related simply to the geometric distance, a quantity required with great precision in ranging applications. The $n=1$ term, which is proportional to the electron content, has been investigated by various investigators in connection with navigational satellite applications. The $n=2$ term in the expansion of the first temporal moment given in this paper comes about through dispersion, finite bandwidth effect and scattering from random irregularities; the numerical values of each of these terms are computed in this paper for a Chapman layer. The second temporal moment is related to the mean square pulsewidth. It is shown that an amplitude modulated pulse at a carrier fre-

quency of 100 MHz may be stretched up to several hundred fold in width, by dispersion and scattering, but such an effect diminishes rapidly in importance as the carrier frequency is raised. These results provide useful information to designers of satellite-based communication and ranging systems.

1. Introduction

In applications of all weather navigation [1], communication [2], and search and rescue [3] using satellite-based radio systems, it is very important to know what effects the intervening propagation medium has on radio signals. The intended signal may be modified in many different ways by dispersion, scattering and multipaths effects while propagating from the satellite to the ground or vice versa. The intent of this paper is to investigate some of these effects produced by the ionosphere. To characterize the signals we will use the temporal moments which have been developed recently in a sequence of papers [4], [5], [6], [7]. Effects produced by temporal dispersion and scattering from ionospheric irregularities are both taken into account. Importance of various effects will be estimated using realistic parameters. Actually, the resulting formulas are all algebraic and the interested reader can compute these simply for himself.

Let the background ionosphere be horizontally stratified, varying only along the vertically downward axis z . Superposed on the background are random irregularities in electron density $\Delta N(\vec{r})$. The dielectric permittivity is then

$$\epsilon(\vec{r}) = \epsilon_0 \langle \epsilon_r(z) \rangle (1 + \mu(\vec{r})) \quad (1)$$

where ϵ_0 is the free space permittivity, and $\langle \epsilon_r(\omega, z) \rangle$ is the relative permittivity of the background medium obtained by taking the ensemble average of ϵ_r and is given by

$$\langle \epsilon_r(\omega, z) \rangle = 1 - \omega_p^2(z) / \omega^2 \quad (2)$$

Here, ω_p is the angular plasma frequency of the background and is a function of z , and ω is the angular frequency of the wave. The fluctuating part of the dielectric permittivity is proportional to $\mu(\vec{r})$ which is given by

$$\mu(\vec{r}) = - \frac{\omega_p^2/\omega^2}{1 - \omega_p^2/\omega^2} \frac{\Delta N(\vec{r})}{N(z)} \quad (3)$$

where N is the background electron density and ΔN is its random fluctuating part. By assumption ΔN has a vanishing mean. In the analysis of wave propagation, it will be assumed that $\Delta N/N$ is zero everywhere except in a slab of finite thickness within which $\Delta N/N$ is a homogeneous random field.

Consider the propagation of a real pulse $p(z,t)$ from the satellite at $z=0$ vertically downward to z . Let the pulse be narrow banded with a carrier angular frequency ω_c . Such a pulse can be expressed as

$$p(z,t) = a(z,t) \exp j[\omega_c t - \int_0^z k_c(\zeta) d\zeta] + \text{c.c.} \quad (4)$$

where $a(z,t)$ is the random complex envelope, $k_c(z) = \omega_c \langle \epsilon_r(\omega, z) \rangle / c$, and c.c. denotes the complex conjugate of the first term.

Define the n th temporal moment by

$$M^{(n)}(z) \equiv \int_{-\infty}^{\infty} t^n \langle a(z,t) a^*(z,t) \rangle dt \quad (5)$$

Here an asterisk is used to denote the complex conjugate operation. When defined in this way, the zeroth moment $M^{(0)}$ is proportional to the energy flow. Under the forward scatter

approximation, which we assume, this energy flow must be constant in a dissipationless ionosphere, which we also assume. Hence

$$M^{(0)}(z) = M^{(0)}(0) = \text{constant} \quad (6)$$

The first moment provides information on the occurrence of the pulse. As a matter of fact, the mean arrival time of the pulse can be defined as

$$t_a(z) = [M^{(1)}(z) - M^{(1)}(0)] / M^{(0)} \quad (7)$$

This is the travel time required by the pulse to propagate from the satellite at $z=0$ to the point of interest at z . As the pulse travels through the medium, it will be distorted and stretched. In particular the mean square pulse width is related to the second moment by

$$\tau^2(z) = M^{(2)}(z) / M^{(0)}(z) - t_a^2(z) \quad (8)$$

More detailed information on the pulse requires a knowledge of the higher temporal moments. For example, the skewness or asymmetry of the pulse is related to the third moment, and the concentration of the pulse is related to the fourth moment. The computation of these higher temporal moments is not difficult but algebraically tedious. With these moments, a least square orthogonal polynomial expansion procedure can be developed to calculate the mean square pulse shape [7]. For many applications, such details are not necessary and information on the mean arrival time and the pulse width will suffice.

2. Mean Arrival Time

Let us place the origin of a coordinate system at the satellite. The signal transmitted by the satellite propagates vertically downward along z through the inhomogeneous ionosphere. The signal encounters a slab of electron density irregularities from z_A to z_B where scattering takes place. The dispersed signal undergoes a further diffraction process in the space $z > z_B$ before it is received at z_R . The mean arrival time of the pulse at the receiver is defined by (7), and its expression derived elsewhere [8] can be rearranged to give

$$t_a(z_R) = z_R/c + \alpha/f_c^2 + \beta/f_c^4 + \dots \quad (9)$$

The first term on the right of (9) is just the free-space travel time and, for any set of realistic parameters, it has by far the largest numerical value. Additional terms occur because of dispersion and scattering. The first correction term is inversely proportional to the square of frequency and is well-known. It is also proportional to the integrated electron density or electron content, i.e.,

$$\alpha = \frac{1}{2c} \int_0^{z_R} f_p^2 d\zeta = \frac{40.3}{c} I \quad (10)$$

The last expression of (10) is obtained when one uses the International System of Units with I representing the electron content in electrons/m². The term α/f_c^2 of (9) is often called the excess time delay (above the free-space value) and is a quantity of interest in satellite-based radio navigation

systems; its variability has been investigated in several references [9], [10]. For example, at a frequency of 1.6 GHz, the excess time delay for I equal to 10^{18} electrons/m² is 52.5 ns. This value of excess time delay corresponds to a distance of 15.74 m which would result in an error if not properly taken into account in ranging calculations. Actually, the excess time delay, of course, contains higher-order correction terms as well, as shown in (9). The second-order correction term has been derived in [8] and can be written as

$$\delta = \frac{1}{c} \left[\frac{3}{8} \int_0^{z_R} f_p^4 d\zeta + \frac{3\overline{v^2}}{2} \int_0^{z_R} f_p^2 d\zeta + \frac{-A_2}{2} \int_{z_A}^{z_B} f_p^2 (z_R - \zeta) d\zeta \right] \quad (11)$$

where $(\overline{v^2})^{1/2}$ is the bandwidth of the signal and A_2 is related to the power spectrum of $\Delta N/N$. The full expression for A_2 can be found in [5]. For a power spectrum with the wave number dependence κ^{-4} , an outer scale ℓ_0 , an inner scale $r_0 \ll \ell_0$, and $\langle (\Delta N/N)^2 \rangle = \sigma_N^2$, A_2 reduces to

$$A_2 = -(\sigma_N^2/\ell_0) \ln(\ell_0/r_0) \quad (12)$$

In (11) the first term has its origin in dispersion, actually the part of dispersion that has the $1/f_c^4$ dependence. The second term in (11) arises from the fact that the transmitted signal has a finite bandwidth, and the third term comes about from scattering from random irregularities. To estimate numerically the magnitudes of these various terms, one has to set up an ionospheric model. For this purpose let the ionosphere be represented by a Chapman layer with

$$\begin{array}{ll} \text{maximum concentration} & N_0 = 10^{12} \text{ electrons/m}^3 \\ \text{scale height} & H = 100 \text{ km} \\ \text{peak height} & h_0 = 300 \text{ km} \end{array} \quad (13)$$

We also need some parameters related to ionospheric irregularities, which are taken to have the following values.

$$\begin{aligned}
 \text{outer scale} & \quad \ell_0 = 50 \text{ km} \\
 \text{inner scale} & \quad r_0 = 10 \text{ m} \\
 \text{rms fluctuations} & \quad \sigma_N = 1 \\
 \text{bandwidth} & \quad (\overline{v^2})^{1/2} = 10 \text{ MHz}
 \end{aligned} \tag{14}$$

A rather large σ_N value of 100% is used in (14), which is believed to exist under intense equatorial scintillation conditions [11]. The irregularities are assumed to be present throughout this Chapman profile. Since $\Delta N/N$ is assumed to be a homogeneous random process, only irregularities near the ionization peak are most important in producing scintillations. This corresponds roughly to a thickness of about 200 km. For these values, the scattering term (i.e. the third term) of (11) has a value two orders of magnitude larger than the dispersion term (the first term) and three orders of magnitude larger than the bandwidth term (the second term). When α given by (10) and β given by (11) are substituted into (9) and the excess time delay is converted into excess distance by multiplying by c , the results so obtained are shown in Fig. 1. At a frequency of 100 MHz, the α term gives an excess distance of 1666 meters and the β term gives an excess distance of 543.5 meters. As the frequency increases, the α term decreases in a manner like $1/f_c^2$, while β term decreases like $1/f_c^4$ as depicted in Fig. 1.

In the planned NAVSTAR Global Positioning System [1], provisions will be made, whereby time delays at two coherent carrier frequencies f_c and mf_c will be measured. Let the corresponding mean arrival times be $t_a(f_c)$ and $t_a(mf_c)$. Then, from (9), the distance z_R is found to be

$$z_R = c \left[\frac{m^2 t_a(mf_c) - t_a(f_c)}{m^2 - 1} + \frac{\beta}{m^2 f_c^4} + \dots \right] \quad (15)$$

For a user with only two-frequency capability, the data can be processed according to the first term of (15), resulting in an estimate of z_R . What has been ignored in such a process are terms given by β and higher-order terms in (15). Depending on m , f_c and the expected accuracy, the truncation in (15) may or may not be important. For example, at GHz frequencies, by ignoring β and higher-order terms the indicated two-frequency measurements will introduce an error not more than 0.1 m, a very small value. However, the same process at 100 MHz will yield an error of several hundred meters which may be too large for certain applications. In the latter case if the accuracy is important, a three-frequency system can be devised whereby time delays are measured at three coherently related frequencies. Proper processing of the three-frequency data can account for both the α term and β term of (9). The error thus committed in estimating z_R is then proportional to terms beyond the β term in the expansion given by (9).

3. Mean Pulsewidth

The mean pulsewidth is related to the second moment through (8). When the indicated computations are carried out, many terms are obtained [5], [8]. For ionospheric applications, some of these terms are unimportant and can be discarded. If only the three more important terms are kept, the mean square pulsewidth at the receiver is

$$\tau^2(z_R) = \tau_0^2 + \tau_1^2 + \tau_2^2 \quad (16)$$

where

$$\begin{aligned} \tau_0^2 &= \tau^2(0) \\ \tau_1^2 &= \frac{\overline{v^2}}{4\pi^2 f_c^6} \cdot \int_0^{z_R} f_p^2 d\zeta \\ \tau_2^2 &= \frac{A_4}{\pi^2 f_c^6} \cdot \int_{z_A}^{z_B} f_p^4 (z_R - \zeta)^2 d\zeta \end{aligned}$$

Note that τ_0 is the original pulsewidth when transmitted by the satellite, τ_1^2 represents broadening contributed by dispersion and τ_2^2 represents broadening contributed by scattering. If the transmitted pulse has a Gaussian spectrum, which we assume in the following computations, the pulsewidth can be related to the bandwidth by

$$\tau_0^2 = 1/(16\pi^2 \overline{v^2}) \quad (17)$$

For a power-law power spectrum of the form κ^{-4} , A_4 is given by

$$A_4 = \sigma_N^2 / (4\ell_0 r_0^2) \quad (18)$$

To give numerical estimates, we again model the ionosphere by a Chapman layer with parameters given by (13) and other parameters given by (14). The irregularities are again allowed to extend throughout the Chapman layer. Under these conditions, τ_1^2 is very small in comparison with τ_2^2 and can be ignored. The effect of pulse broadening through scattering is depicted in Fig. 2. For the parameters chosen, a pulse at a carrier frequency of 100 MHz is stretched to 142 times the original pulsewidth when received. However, as the radio carrier frequency increases the pulsewidth decreases rapidly like $1/f_c^3$ until it is approximately equal to the original pulsewidth τ_0 . With a further increase in carrier frequency the pulsewidth becomes nearly unaffected by propagation effects. The frequency at which $\tau_0^2 = \tau_2^2$ is defined as f_e . Accordingly,

$$f_e^6 = 16\overline{v^2}A_4 \int_{z_A}^{z_B} f_p^4 (z_R - \zeta)^2 d\zeta \quad (19)$$

For the Chapman ionospheric model adopted in this paper, (19) can be written as

$$f_e^6 = 1.012 \times 10^{21} \overline{v^2} \sigma_N^2 N_0^2 / (\ell_0 r_0^2) \quad (20)$$

where all quantities are expressed in the International System of Units. For cases in which τ_1^2 is small in comparison with τ_2^2 , the original pulse is stretched to $\sqrt{2}$ times its original width at $f_c = f_e$. When $f_c \gg f_e$, the original pulsewidth is unchanged after propagating through the medium. But when $f_c \ll f_e$, the original pulsewidth is lengthened tremendously.

Therefore, in estimating the propagation effects on pulse-width, it is important to know the value of carrier frequency f_c relative to f_e .

4. Effect of Oblique Propagation

In all of the above computations, we have assumed that the waves are incident normally on the horizontally stratified ionosphere. If the waves are incident obliquely as in the case in most application situations, these formulas must be modified. The required modification is simple when the zenith angle i is not larger than about 45° . In this case, z_R in the first term of (9) must be replaced by d_R , the geometric distance between the satellite and the user. The integrals for α and β in (9) and the integrals for τ_1^2 and τ_2^2 in (16) must be carried out along an oblique path. This can be done by replacing $d\zeta$ by $\sec i \, d\zeta$, where, by Snell's law,

$$\sec i = \sec i_0 [1 + (f_p^2 / 2f_c^2) \tan^2 i_0 + \dots] \quad (21)$$

Here i_0 is the zenith angle of the ray at the ionospheric base. With such replacements, the net modification on the expressions for α and β in (9) and on the expressions for τ_1^2 and τ_2^2 in (16) can be stated simply as follows. For α , the expression given by (10) must be multiplied by $\sec i_0$; or alternately the expression (10) is unchanged with the understanding that I now denotes the oblique electron content. For β , the expression (11) must be multiplied by $\sec i_0$ and a new term given by

$$\frac{1}{4c} \sec i_0 \tan^2 i_0 \int_0^{z_R} f_p^4 \, d\zeta \quad (22)$$

must be added. This new term comes about because of ray bending. For the parameters chosen and with $i_0 < 45^\circ$, this new term is small compared with the scattering term. In this case the modification has the net effect of increasing all excess distances by a factor $\sec i_0$ which amounts to, for example, a 41% increase for $i_0 = 45^\circ$ when compared with the vertical case. Similar considerations for the mean square pulsewidth can be done. Compared with the vertical propagation case, the relative pulsewidth for the oblique ray is increased by a factor $\sec^{1/2} i_0$, which amounts to a 20% increase when $i_0 = 45^\circ$. These results give the amount of degradation that can be expected when the satellite moves away from the overhead position. The amount of degradation can be fairly severe if the satellite is moved far away from the vertical and appears near the horizon.

In all the formulas given above, the electron density irregularities are assumed to be isotropic. When the irregularities are anisotropic, additional modifications are expected; but such modifications appear only on scattering terms. In general, if the irregularities are elongated the scattering effects are expected to be strongest when the propagation path is parallel to the elongation. However, quantitative estimates can be made only after extending the theory.

5. Conclusion

We have shown in this paper the various effects a radio pulse may encounter while propagating through the ionosphere. Of particular interest are the mean arrival times and root mean square pulse width. The mean arrival time of a pulse is determined by the sum of many terms. The leading term is the free space transit time which is independent of the carrier frequency. The second term has its origin in dispersion and is proportional to the electron content and inversely proportional to the square of the carrier frequency. This second term is well-known and has been studied because of its application in the planned satellite-based navigational systems [9], [10]. The third term is inversely proportional to the fourth power of the carrier frequency and is itself composed of three terms, each representing the effect produced by dispersion, the finite bandwidth and the scattering from irregularities, respectively. In a satellite-based navigational system using two frequencies, the excess distance caused by the second term, i.e., the term proportional to the electron content can be compensated through proper data processing, but no amount of data processing can compensate simultaneously the excess distance contained in the third term. In such a case the third term represents the error in ranging measurements. This error has a very strong dependence on the carrier frequency, being inversely proportional to the fourth power of the carrier frequency. Numerical estimates show that the error can be

fairly large (approximately several hundred meters) at 100 MHz but very small (less than 0.1 meter) at 1 GHz or higher.

The expression for the mean square pulsewidth consists of three terms: the original mean square pulsewidth term, the term contributed by the finite bandwidth and the term contributed by scattering from random irregularities. For ionospheric applications and when the irregularity fluctuations are intense, the finite bandwidth term can be ignored in comparison with the scattering term. Both the finite bandwidth term and the scattering term have $1/f_c^6$ dependence and hence decrease very rapidly with increasing f_c . If the original pulsewidth is tremendously lengthened at low frequencies through dispersion and scattering, such effects will diminish rapidly with increasing carrier frequency. In this connection it is useful to define a frequency f_e as that frequency at which the mean square pulsewidth due to scattering is equal to the original mean square pulsewidth. When defined this way, the original root-mean-square pulsewidth is lengthened to $\sqrt{2}$ times its original root-mean-square pulsewidth when $f_c = f_e$. For the numerical values adopted f_e is found to be 522 MHz.

In making these estimates, the radio signal is assumed to be incident on the ionosphere normally. For most applications the radio ray will arrive at the receiver obliquely. When the zenith angle of the ray is 45° , the excess distance is increased by 41% and the relative pulsewidth is increased by 20%. For a zenith angle larger than 45° , the increase will be larger, but a more refined theory is needed to estimate the numerical value quantitatively.

Acknowledgement

This research was supported by the U.S. Army Research Office under Grant DAAG 29-76-G-0286 and Grant DAAG 29-78-G-0101.

References

- [1] E. M. Lassiter and B. Parkinson, "NAVSTAR/GPS: Operational Status", Proceedings of the International Navigation Congress, 173-180, Boston, Aug. 3-6, 1976.
- [2] J. J. Spilker, Jr., Digital Communications by Satellite, Prentice-Hall, N.J., 1977.
- [3] F. H. Raab, G. W. Board, S. D. Arling, J. D. Dobbs, S. C. Smadell and J. R. Waechter, "An application of the Global Positioning System to search and rescue and remote tracking", Navigation, 24, 216-228, 1977.
- [4] K. C. Yeh and C. C. Yang, "Mean arrival time and mean pulsewidth of signals propagating through a dispersive and random medium", IEEE Trans. Antennas Propagat., AP-25, 710-713, 1977.
- [5] K. C. Yeh and C. H. Liu, "An investigation of temporal moments of stochastic waves", Radio Sci., 12, 671-680, 1977.
- [6] C. H. Liu and K. C. Yeh, "Propagation of pulsed beam waves through turbulence, cloud, rain or fog", J. Opt. Soc. Am., 67, 1261-1266, 1977.
- [7] C. H. Liu and K. C. Yeh, "Pulse propagation in random media", IEEE Trans. Antennas Propagat., AP-26, 561-566, 1978.
- [8] Y. K. Wong, K. C. Yeh and C. H. Liu, "Mean arrival time and mean pulse width of signals propagating through an inhomogeneous ionosphere with random irregularities", Proceedings of 1978 Symposium on the Effect of the Ionosphere on Space and Terrestrial Systems, paper 6-2, January 24-26, 1978.
- [9] Haim Soicher, "Ionospheric and plasmaspheric effects in satellite navigation systems", IEEE Trans. Antennas Propagat., AP-25, 705-708, 1977.
- [10] J. A. Klobuchar, M. J. Buonsanto, M. J. Mendillo and J. M. Johanson, "The contribution of the plasmasphere to total time delay", Proceedings of 1978 Symposium on the Effect of the Ionosphere on Space and Terrestrial Systems, paper 6-4, January 24-26, 1978.
- [11] S. Basu and M. C. Kelley, "Review of equatorial scintillation phenomena in light of recent developments in the theory and measurement of equatorial irregularities", J. Atmos. Terr. Phys., 39, 1229-1242, 1977.

Fig. 1 Excess distance as a function of frequency. The ionospheric model parameters are given in (13) and (14). The excess distance corresponding to the α term of (9) is proportional to $1/f_c^2$ and that corresponding to the β term of (9) is proportional to $1/f_c^4$, as marked on the graph.

Fig. 2 Relative lengthening of pulsewidth as a function of carrier frequency. The ionospheric model parameters are given in (13) and (14).



(13) $f_c = 1.5$ MHz

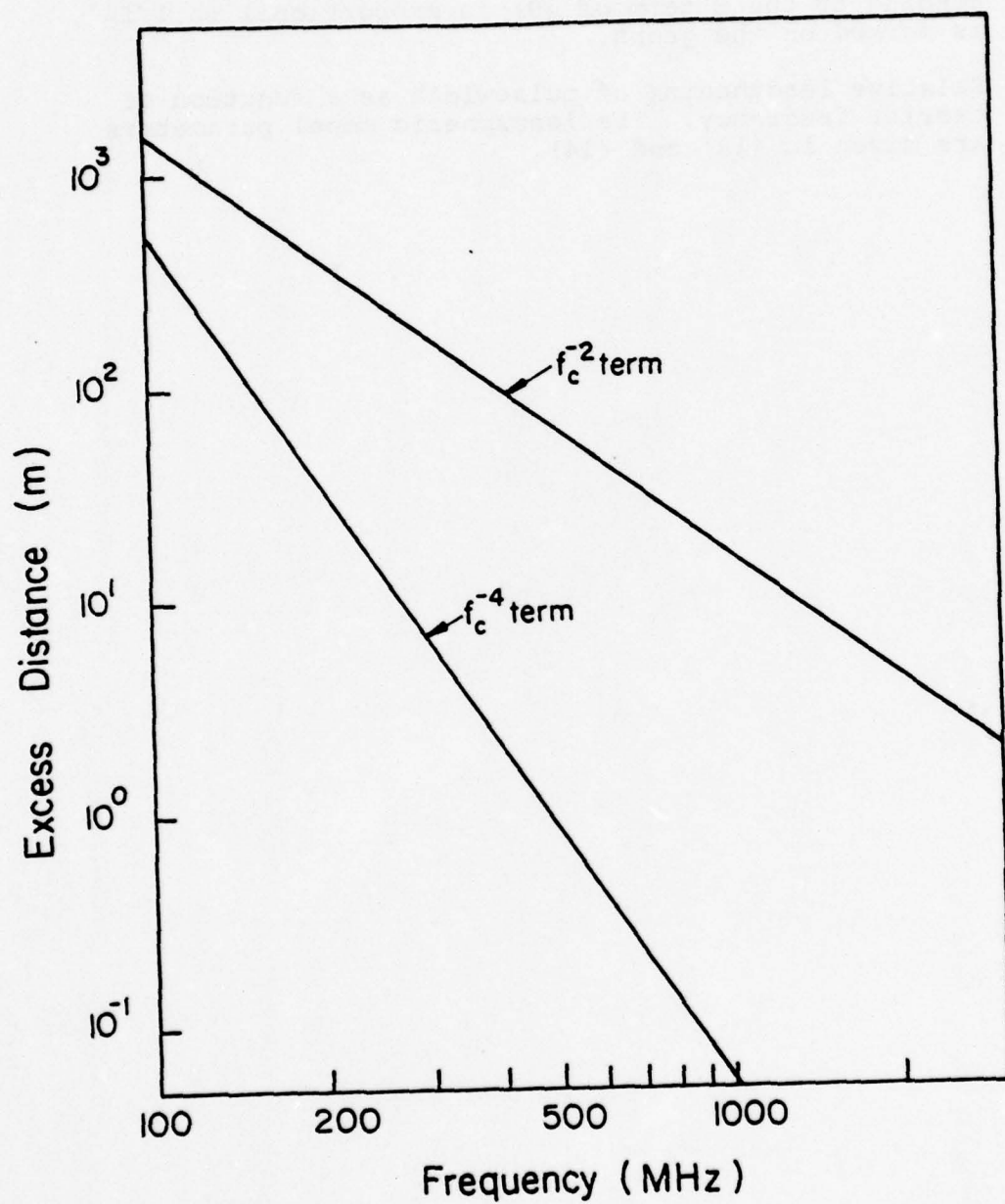


Fig. 1

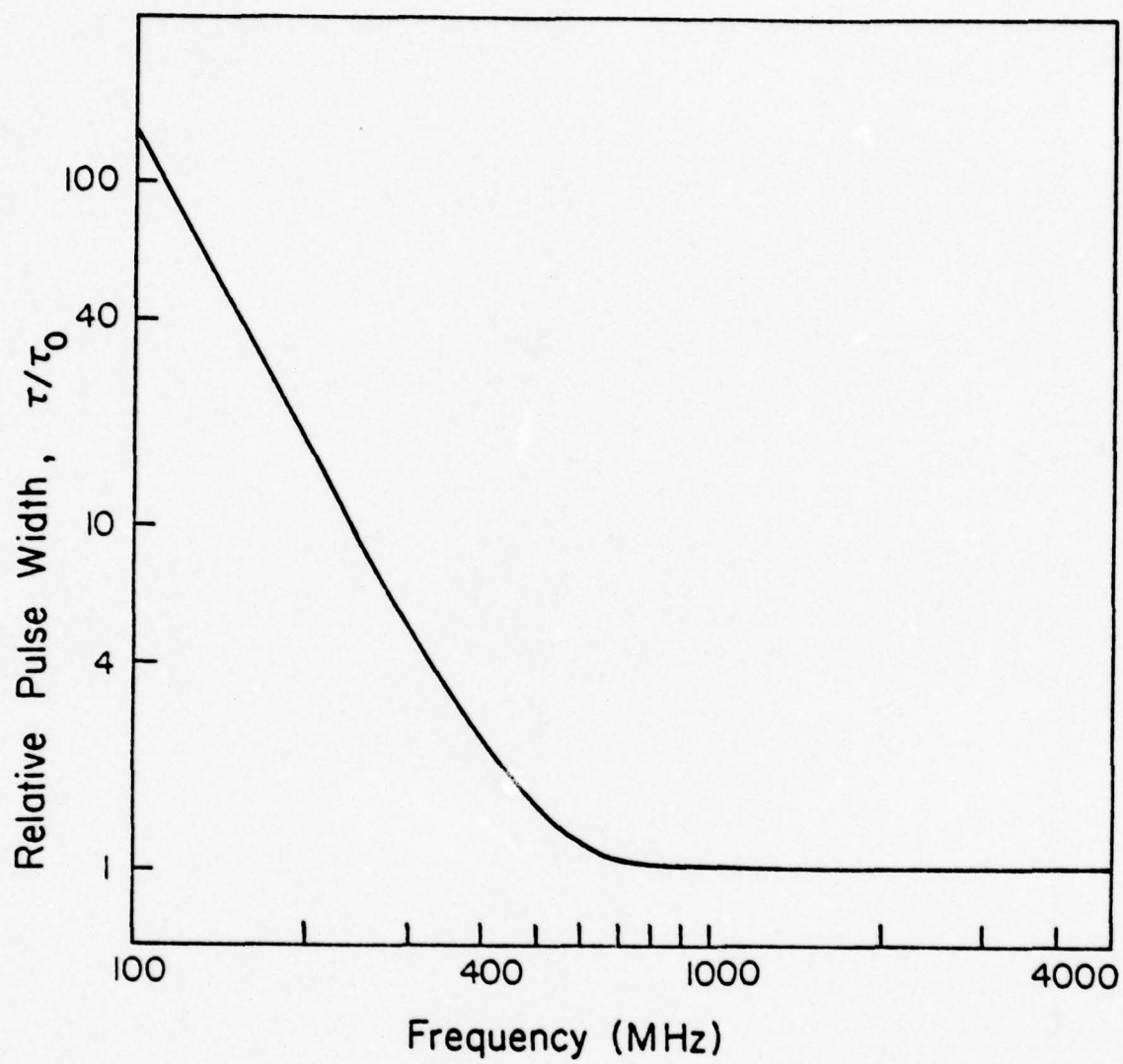


Fig. 2

Appendix E

Scintillation Observations at Natal

by

K. C. Yeh, J. P. Mullen, J. R. Medeiros, R. F. da Silva and
R. T. Medeiros

SCINTILLATION OBSERVATIONS AT NATAL

K. C. Yeh
Department of Electrical Engineering
University of Illinois, Urbana, IL. 61801, U.S.A.

J. P. Mullen
Air Force Geophysics Laboratory
Hanscom Air Force Base, MA. 01731, U.S.A. .

J. R. Medeiros, R. F. da Silva and R. T. Medeiros
Departamento de Física Teórica e Experimental
UFRN - CCE

Abstract

An equatorial ionospheric scintillation program was performed during the period 27 February - 13 March 1978 in Peru, Brazil, Ghana and Ascension Island. The purpose of the experiment was to study the generation, persistence and decay of the large scale irregularity structure which is responsible for diffraction of radio waves transmitted through the ionosphere.

This report stresses results obtained at the Ionospheric Radio Observatory, which is staffed by the Departamento de Física Teórica e Experimental, Centro de Ciências Exatas, Universidade Federal do Rio Grande do Norte.

The Observatory recorded signals of MARISAT I (1976-17A) and LES-9 (1976-23B), the former at 257.55 MHz and the latter at 249.6 MHz. During the nighttime hours scintillation on both signals commonly exceeded 20 decibels peak to peak, and some scintillation occurred on 10 of the 15 nights of the experiment. Scintillation measurements performed with spaced receivers on a 278 meter baseline indicate eastward irregularity

velocities of approximately 30 - 150 meters per second during the nighttime hours. The fading rates observed ranged from 1 per second to 6 per minute.

R E S U M O

Um programa equatorial sobre cintilações ionosféricas foi realizado durante o período de 27 de fevereiro - 13 de março no Peru, Brasil, Gana e Ilha da Ascensão. O propósito da experiência era estudar a produção persistência, e decaimento de irregularidades de grande escala que são responsáveis pela difração de ondas de rádio transmitidas através da ionosfera.

Esse artigo dá ênfase a resultados obtidos no Radio-Observatório Ionosférico do Departamento de Física Teórica e Experimental, Centro de Ciências Exatas da Universidade Federal do Rio Grande do Norte.

O Observatório gravou sinais dos satélites MARISAT I (1976-17A) e LES-9(1976-23B) nas frequências de 257,55 MHz e 249,6MHz, respectivamente. Durante a noite a cintilação em ambos sinais excedeu, frequentemente, o valor de 20 decibéis pico-a-pico e ocorreram cintilações em 10 noites das 15 noites de observação. Medidas de cintilações efetuadas usando-se antenas espaçadas de 278 metros indicaram componentes de velocidade das irregularidades no sentido Oeste-Leste de aproximadamente 30-150 metros por segundo durante a noite. As taxas de flutuação de amplitude observadas vão de 1 por segundo até 6 por minuto.

Introduction: A joint equatorial scintillation program was carried out from 27 February to 13 March 1978. The program included scientists of the Universidade Federal do Rio Grande do Norte, Natal, Brasil (UFRN), the Geophysical Institute of Peru (IGP), the University of Texas at Dallas (UTD), the University of Illinois (UI), Emmanuel College, Boston, Massachusetts, the Air Force Geophysics Laboratory (AFGL), and the Space and Missiles Test Center (SAMTEC). The sites operated were at Natal, (Brazil), Ancon, Jicamarca and Huancayo (Peru) and Ascension Island Station. In addition, the AFGL Airborne Ionospheric Observatory flew selected flight patterns over Peru and Ascension Island. Because of the wealth of data during the period, this report confines itself to the observations and preliminary results gleaned from the UFRN station at Natal.

Background: From July 1974 to January 1977 the Observatory at UFRN was observing signals transmitted by the LES-6 (1968-81D) satellite at 254 MHz. From January 1977 to the present, MARISAT I (1976-17A) has been observed at 257.55 MHz. The antenna system consists of a 30 foot parabolic antenna which was first installed on a fixed mount and later on a manually steerable mount. The receiving system consists of a Vanguard converter and an R-390A/URR receiver. Recording was on a strip chart having a response of about .01 seconds. Because of the reasonably similar sub-ionospheric intersections (5.35°S , 35.4°W for LES-6 and 5.35°S , 33.6°W for MARISAT II) it was found feasible to combine the data and to generate the contours shown in Figure 1. For purpose of plotting Figure 1, the scintillation index SI is defined by the formula

$$SI = (P_{\max} - P_{\min}) / (P_{\max} + P_{\min}) \quad (1)$$

where P_{\max} is the maximum power observed on the chart record and P_{\min} is the minimum power. It is sometimes convenient to express SI on a percentage basis. A discussion of the scintillation index SI defined by (1) and its relation to other definitions of scintillation index such as peak-to-peak fluctuation in db and S_4 index has been made by Whitney, Aarons and Malik (1969). The plot of Figure 1 shows a high probability of occurrence of substantial scintillation near the southern summer solstice and a minimum probability at the southern winter solstice. No detectable scintillation at these frequencies was found during the daylight hours. The diurnal maximum was found at 2100-2300 LMT, which is essentially that found at Huancayo and reviewed by Aarons (1977).

Current Observations: During the 15 nights of the experiment, scintillation occurred on ten of them. We have chosen one of these for detailed examination. Figure 2 which compares the scintillation for the nights of 9-10 March 1978 observed on the signals of MARISAT I and LES-9 (1976-23B) is in agreement with the long term results shown in Figure 1. The sub-ionospheric points for a 400 km intersection were:

MARISAT I: 5.16° S Lat, 33.71° W long.

LES-9: 3.68° S Lat, 38.2° W long.

This spacing furnishes an opportunity to examine the relative timing of the onsets of strong scintillation. The actual onset times were, to the best accuracy determinable from the chart records,

MARISAT I 2155 UT

LES-9 2159 UT

Because the distance between the 400 km ionospheric intersections is too great (531 km) to be traversed by the normal irregularity drift in the measured time, it must be supposed that the onsets represented the generation of two separate irregularity clouds. In this example, the easterly location first encountered scintillation.. In earlier work (Bandyapadhyay and Aarons, 1970) scintillation was commonly seen earlier in the west, but a considerable number of observations was found in which scintillation was first seen on an easterly path as it was seen here. Scintillation occurring earlier in the east would naturally be expected because of the earlier arrival of nightfall in that direction. However, the angle of elevation effects can often enhance the effects of weaker scattering layers and present the appearance of having scintillation in either direction. For high angle observations, however, first occurrence in the east is most likely (Koster, private communication, 1978). The scintillation seen in Figure 2 was quite intense, exceeding 30 db on MARISAT and 16 db on LES-9. The differences in the scintillation levels from these two satellites can be attributed in large part to the differences in receiving equipment, the MARISAT receiver utilized a 30-foot parabolic antenna having a nominal gain of 25-db whereas the LES-9 equipment used a single yagi with a gain of 12 db. This continued on both channels for about 4 1/2 hours. There was little evidence seen of the onsets and decays indicative of multiple discrete irregularity clouds, either in Figure 2 or in the raw data. The conclusion which must be drawn is that there exists large scale structures seen simultaneously at both sub-ionospheric locations, but having strong gradients which produce the patterns seen in Figure 2.

Other observers (Aarons, Whitney and MacKenzie 1978) have, in this program, noted that the irregularity patch expanded westward shortly after sunset at the layer (i.e., about 1930 LMT). They have noted that the westward movement halted, with a subsequent eastward drift on the order of 50-300 meters per second. In a later section our drift measurements will be described.

A short distance away, a second receiving system was established by the University of Illinois to perform multifrequency observations of MARISAT. During the program this system recorded the 257.55 MHz signal of MARISAT and by interconnection enabled drift measurements to be made. A helical antenna with a gain of 16 db is used as compared with 25 db gain provided by the 30-foot parabolic antenna.

In Fig. 3 is reproduced a short section of the sample record showing MARISAT amplitude scintillations at 257.55 MHz from the two locations. The receiving antenna of the top channel is 278 meters to the west of the bottom channel. For such a small spacing the signals are generally almost perfectly correlated with a time delay which can be used to compute the irregularity drift speed along the baseline. This has been done for the data recorded in the evening of March 9, 1978.

Fig. 4 shows the behavior of scintillation during the evening of March 9, 1978. Evidence of scintillation first appeared at 2154 UT (see top panel of Fig. 2). This scintillation rose quickly in intensity and was fully developed in about 2 minutes at which time the peak-to-peak fluctuations were 15 db, which corresponded to a S_4 scintillation index of 0.63. About 10 minutes later the scintillation reached its

maximum at 20 db (corresponding to $S_4=0.80$). It stayed at this high value for about 40 minutes, after which a gradual decay phase set in. This decay continued for more than five hours until the scintillation completely disappeared at 0440 UT March 10, 1978. During the same time the fading rate had a behavior shown in the middle panel of Fig. 4. Because of the slow recording speed before 0020, which made scaling the fading rate impossible, the fading rate data were available only after 0020 UT. In this preliminary report, the fading rate is defined as the average number of maximum per second in a record of one minute duration centered about the time of interest. It is seen in Fig. 4 that the fading rate decreased continuously from nearly 1 sec^{-1} shortly after midnight to 0.1 sec^{-1} in three hours. During the same time the time delay of the fading patterns observed at spaced stations increased steadily from less than 2 seconds to more than 6 seconds as depicted by the curve on the bottom panel of Fig. 4.

The apparent anticorrelation between the fading rate and the time delay as evidenced in Fig. 4 is interesting and needs further investigation. Since the baseline distance and orientation are known, it is possible to compute the component of the drift velocity along the baseline. The results are shown in Fig. 5. The eastward drift was approximately 150 m/s shortly after the midnight and it decreased steadily to a value of approximately 30 m/s at 0400 UT. The average trend of the fading rate obtained by replotting the data shown in Fig. 4 is also depicted in Fig. 5. Both the velocity curve (marked V) and the fading rate curve (marked F) showed a decreasing trend. This is expected; since under the weak scatter limit and the frozen-in hypothesis, the scintillation theory predicts the fading rate to be directly proportional

to the irregularity drift speed. However, when the scintillation gets stronger, the multiple scattering effects are expected to become increasingly important. Theoretical computations have shown that effects caused by multiple scattering will actually decrease the correlation intervals (Yeh, Liu and Youakim, 1975). In other words, for a given drift speed, the fading rate will increase with the increasing scintillation. As the observed scintillation was decreasing through the period of interest, it may explain why the average rate of decrease of the fading rate was quite different from that of the velocity in the beginning, even though they were very similar near the end of the scintillation period as shown in Fig. 5. If such an explanation is correct it may also imply that the irregularity spectrum did not change much in the period of interest.

Conclusion: We have described in this paper our preliminary scintillation observations made at Natal. It is shown that at 250 MHz, the peak-to-peak fluctuations can often reach a value as high as 30 db which corresponds to an S_4 scintillation index of nearly unity. With such a high value of S_4 index, the multiple scatter effects are certainly important and the fading signal must be well into the saturation regime. Long term observations show that the scintillation activities at an equatorial station such as Natal are highly seasonal and occur mainly at local night. Spaced receiver experiments indicate, at least in one instance, an eastward drift of nighttime irregularities with a velocity 150 m/s shortly after 0000 and decreasing to 30 m/s in about four hours. Such drift measurements have implied consequence in the study of equatorial electric field. These measurements are being continued and more detailed results will be published in the future.

Acknowledgement

The work reported in this paper was partially supported by the U.S. Army Research Office under grants DAAG 29-76-G-0286 and DAAG 29-78-G-0101 and partially supported by the U.S. Air Force under grant AFOSR 78-3613. One of us (RTM) would like to thank CNPq, for a fellowship awarded to him during the course of this work. The reported work would not have been possible if strong support from J. J. M. Moreira was not received.

Bibliography

Aarons, J., Scintillation studies of the ionosphere in AGARDograph No.166 on Total Electron Content and Scintillation Studies of the Ionosphere, edited by J. Aarons, 1973.

Aarons, J., H. Whitney and E. Martin MacKenzie, The Formation, Duration and Decay of Equatorial Irregularity Patches; The Ground Scintillation Observations. To be presented at URSI, Boulder, Colorado, 5-10, Nov. 78.

Bandyopadhyay, P. and J. Aarons, The Equatorial F-Layer Irregularity Extent as Seen from Huancayo, Peru, Radio Science, 5, 931-938, 1970.

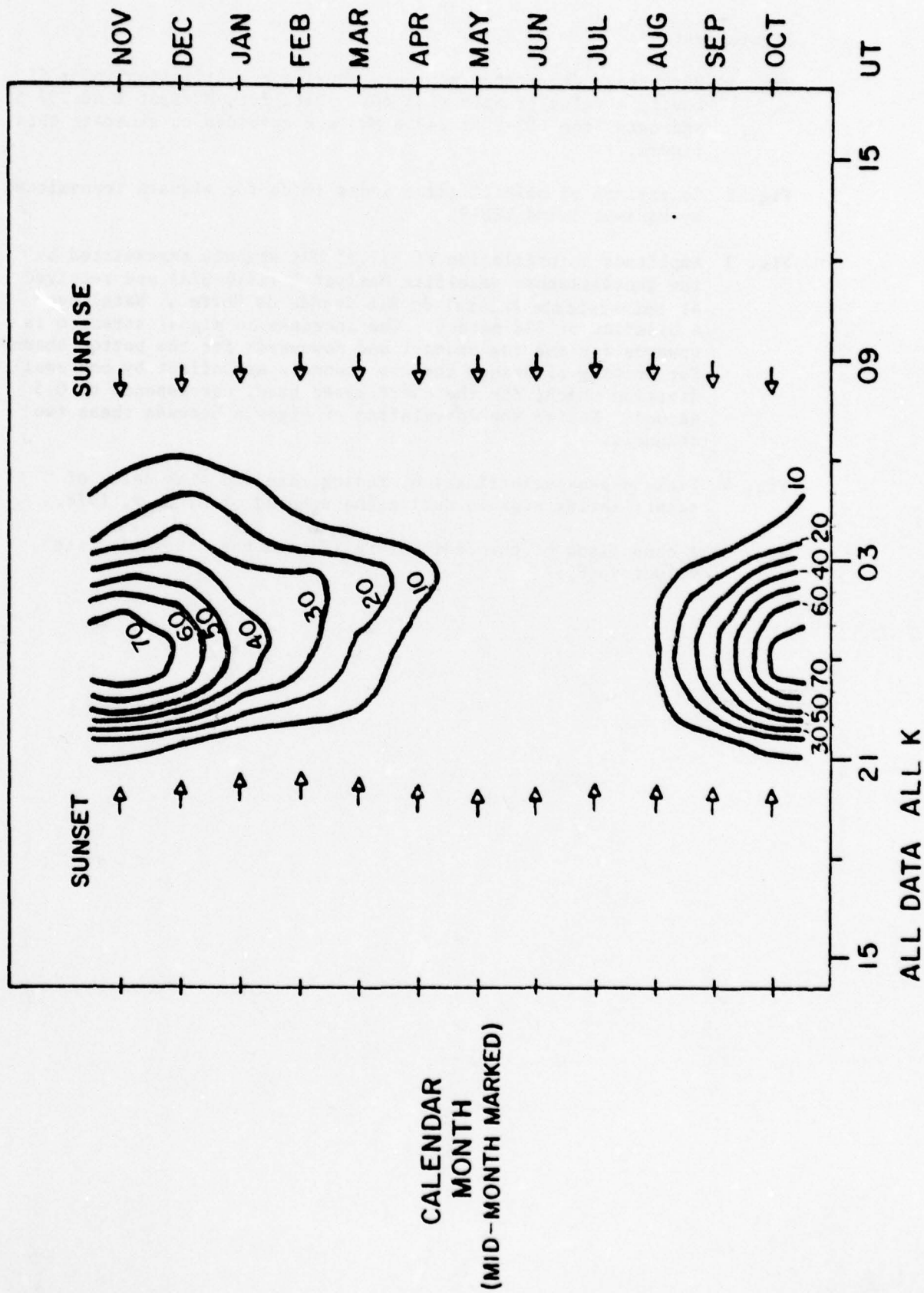
Whitney, H. E., J. Aarons and C. Malik, A proposed index of measuring ionospheric scintillations, Planet. Space Sci., 17, 1069-1073, 1969.

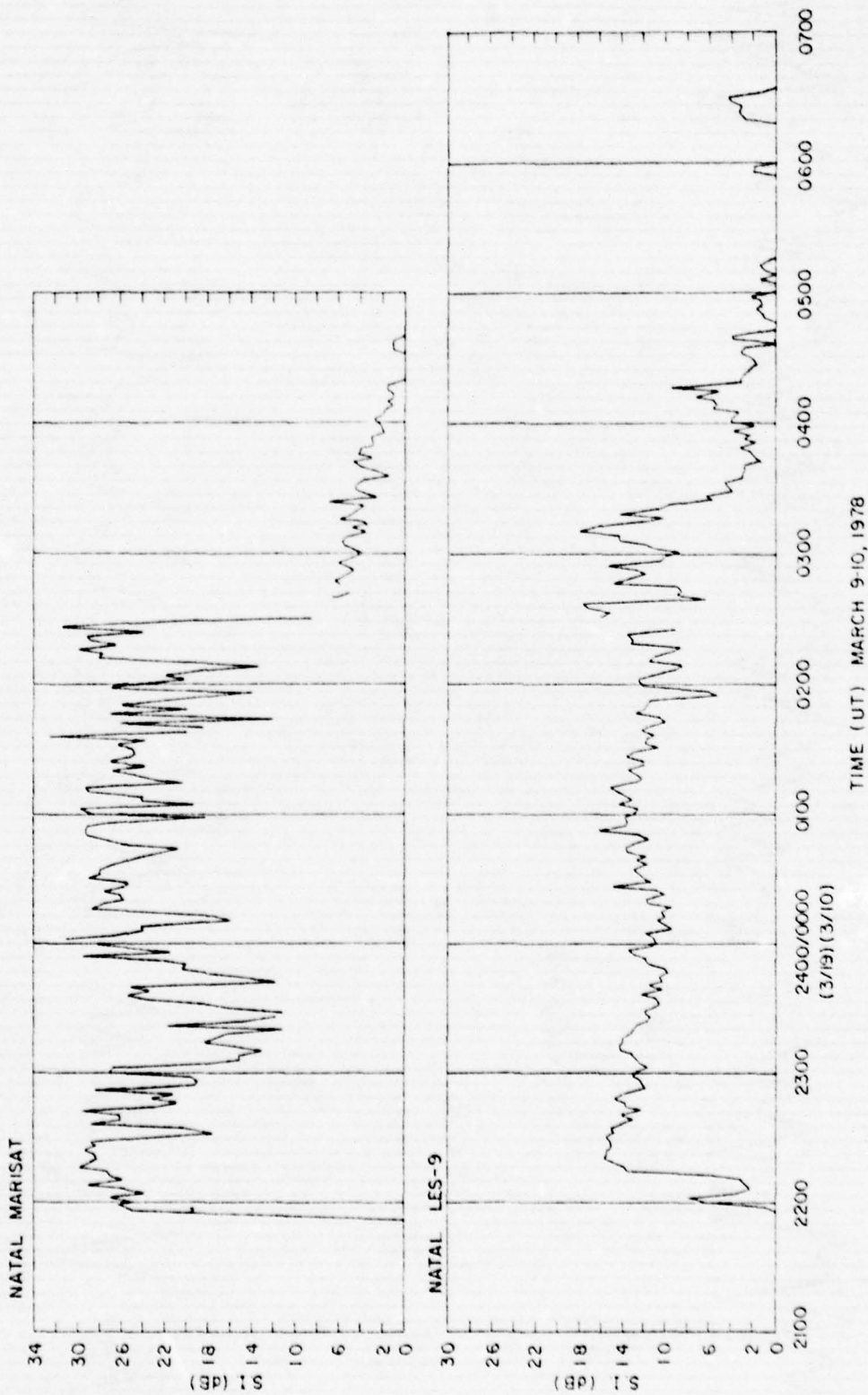
Yeh, K. C., C. H. Liu and M. Y. Youakim, A theoretical study of the ionospheric scintillation behavior caused by multiple scattering, Radio Science, 10, 97-106, 1975.

Figure captions

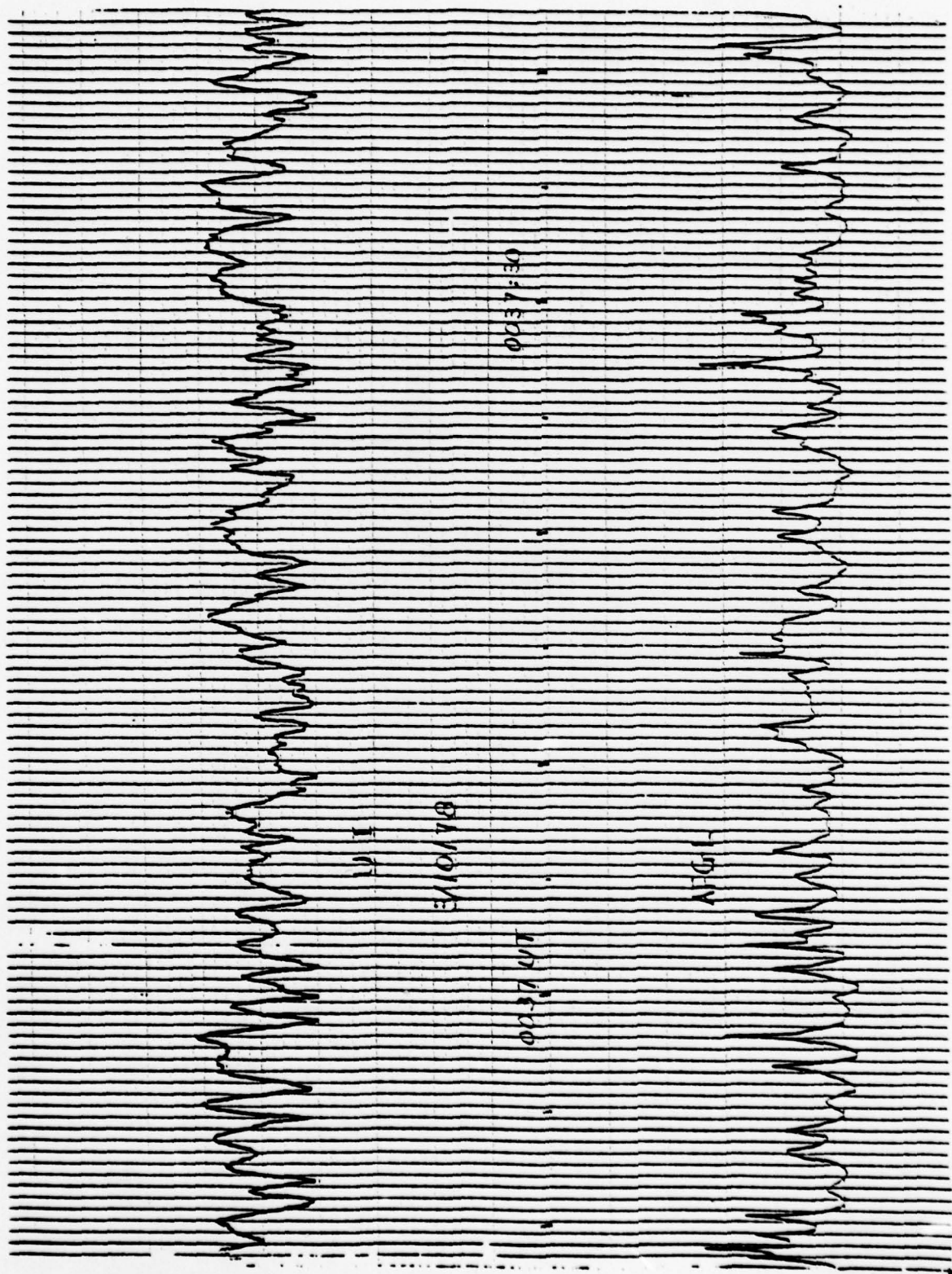
- Fig. 1 Percentage occurrence contours showing scintillation index SI having a value greater than 60%. Data from Marisat 1 at 257.55 MHz and data from LES-9 at 249.6 MHz are combined to generate this figure.
- Fig. 2 Comparison of scintillation index in db for signals transmitted by Marisat 1 and LES-9.
- Fig. 3 Amplitude scintillation of 257.55 MHz signals transmitted by the geostationary satellite Marisat 1 (1976-17A) and received at Universidade Federal do Rio Grande do Norte, Natal over a baseline of 278 meters. The increase in signal strength is upwards for the top channel and downwards for the bottom channel. For writing clearance the two channels are offset by one small division which, for the chart speed used, corresponds to 0.5 second. Notice the correlation of signals between these two channels.
- Fig. 4 Peak-to-peak scintillation, fading rate and time delay of scintillating signals during the evening of March 9, 1978.
- Fig. 5 A comparison of the fading rate (F) and the eastward drift velocity (V).

PERCENTAGE OCCURRENCE GREATER THAN 60 NATAL L6 AND MS

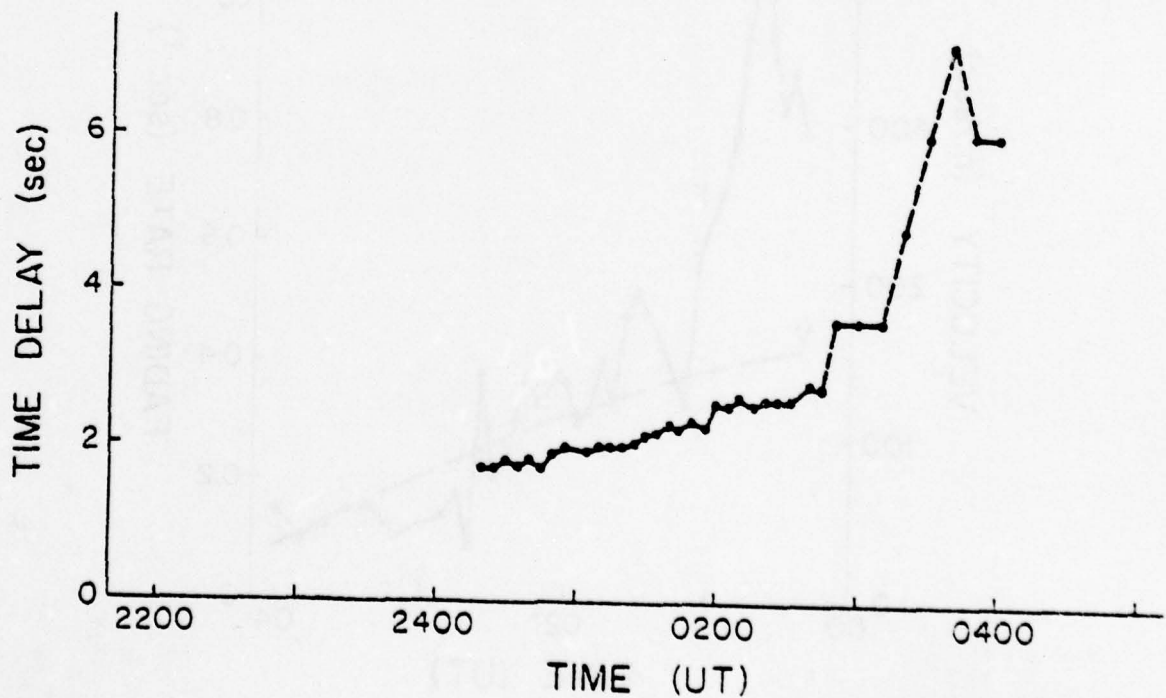
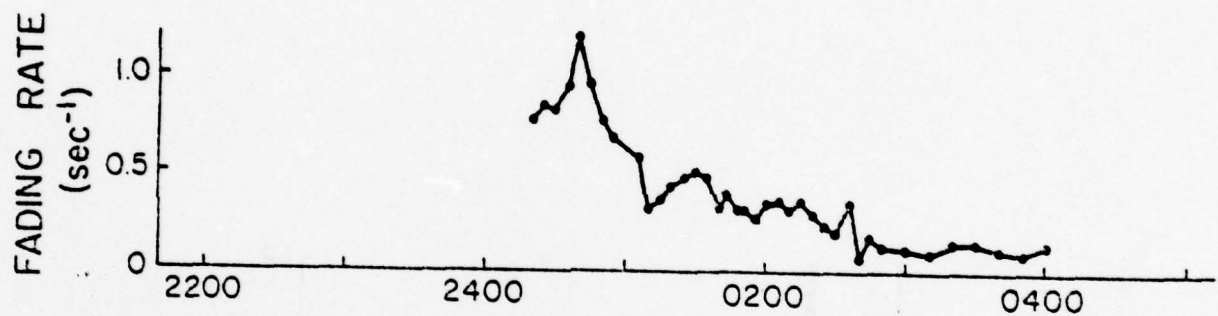
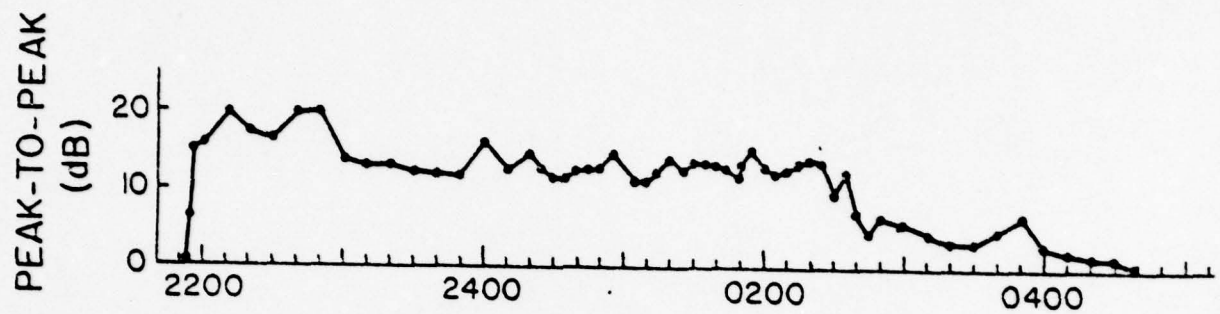


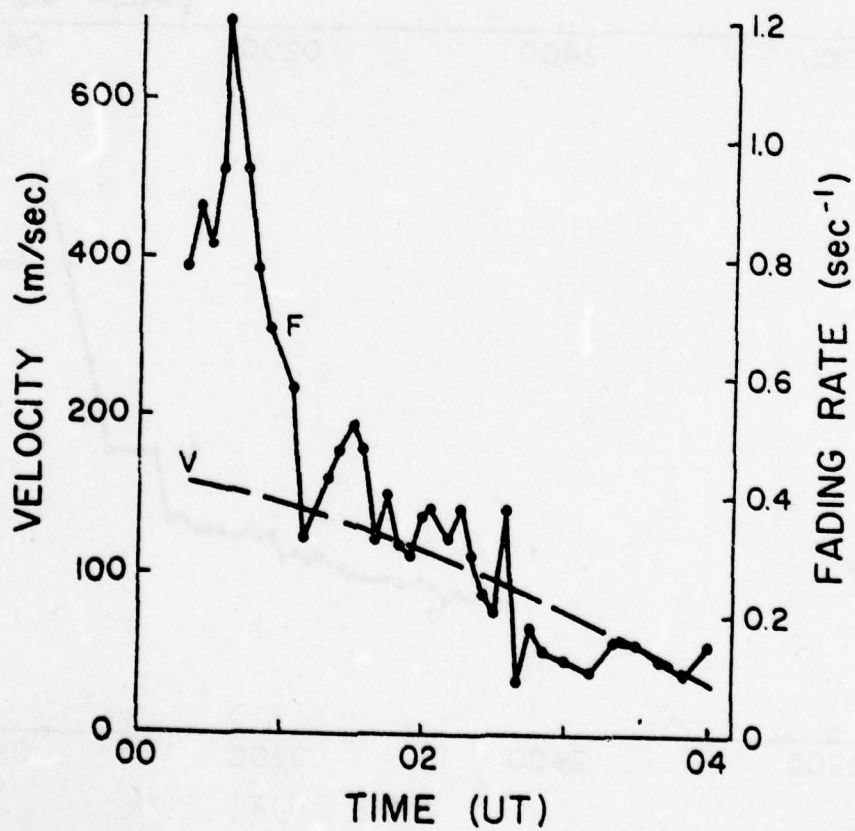


70
20
2



3/9/78 - 3/10/78





Appendix F

Observations of Equatorial Ionospheric Bubbles
by the Radio Propagation Method

by

K. C. Yeh, H. Soicher and C. H. Liu

OBSERVATIONS OF EQUATORIAL IONOSPHERIC BUBBLES
BY THE RADIO PROPAGATION METHOD

K. C. Yeh*, H. Soicher⁺ and C. H. Liu*

*Department of Electrical Engineering,
University of Illinois, Urbana, IL 61801

⁺Center for Communication Systems US Army Communication
Research & Development Command Fort Monmouth, NJ 07703

Abstract

Recent data collected near the magnetic equator depict one kind of ionospheric perturbations in the nighttime hours variously as bubbles or plumes. Theoretical studies show that the under-side of the ionosphere is subjected to Rayleigh - Taylor instabilities which, when triggered, will cause a region of depleted ionization to rise as bubbles. When such regions are traversed by a probing radio wave, the associated Faraday effect is expected to show depletions of the electron content. This paper describes some experimental results obtained at Natal, Brazil (35.23°W, 5.85°S, dip-9.6°) by monitoring radio signals transmitted by the geostationary satellites MARISAT 1 and SMS 1. Using ionization depletions as indications of bubbles, statistical studies of occurrence, size and magnitude of perturbations are carried out. The most probable depletions for the propagation path under study have values in the range 1 to 4×10^{16} electrons per meter², but depletions as large as 1.2×10^{17} electrons per meter² have also been observed. The average durations for each observed bubble may vary from less than 2 minutes to over 30 minutes with an average of 8 minutes. The experimental data further show that the scintillation rate may increase suddenly when these bubbles either form along or drift across the propagation path.

Introduction

Recent flurry of activities at the magnetic equator has helped to reach some understanding about the nature of one kind of ionospheric perturbations occurring at night.

Such ionospheric perturbations are described variously as ionization depletions, bubbles, plumes, some type of irregularity patches or equatorial spread F irregularities. On the experimental side, the radar backscatter maps [Woodman and LaHoz, 1976] show dramatically the plume-like structures when viewed vertically upward as a function of time at a fixed location. When measured in situ, large depletions of ionization are observed as the satellite passes nearly horizontally [McClure et al., 1977] or as the rocket traverses nearly vertically [Kelley et al., 1976] through these bubbles. The boundary of the bubble can be very steep and has been described as ionization walls. Inside the ionization walls are highly complex and spiky ionization structures which give rise to a power law type irregularity power spectrum [Dyson et al., 1974; Morse et al., 1977; Woodman and Basu, 1978]. Based on propagation measurements, the occurrence of these bubbles have been shown to be correlated with the onset of scintillation on satellite radio signals [Aarons, 1977; Basu and Basu, 1976]. They have also been found to be responsible for backscattering in transequatorial propagation [Röttger, 1976]. On the theoretical side, the attention has been mainly focused on some type of plasma instabilities. Early investigations have shown that

the bottom side ionosphere is subject to Rayleigh - Taylor instabilities with a growth rate [Liu and Yeh, 1966a and b]

$$\gamma = \frac{gN'}{v_{in}N} - \beta \quad (1)$$

where g is the gravity, N is the electron concentration, N' is its height gradient, v_{in} is the ion-neutral collisional frequency and β is the effective attachment coefficient of electrons. Recent numerical simulations show that a plasma mode which is linearly unstable as predicted by (1) or its generalization or any other fluid type gradient instability must evolve nonlinearly so that as the depletion increases the nonlinear polarization $\vec{E} \times \vec{B}$ forces in the equatorial geometry can drive the depleted region upward through the ionization peak to the topside ionosphere [Ossakow et al., 1979]. Such a process is apparently very sensitive to background conditions as the computed bubble rising velocity has been found to vary from 2.5 m/s to 160 m/s.

Analytic treatment of the same problem [Ott, 1978] has shown that the initial bubble rising velocity depends on the amount of depletion and is given by

$$v = \frac{N_0 - N_b}{N_0 + N_b} \frac{g}{v_{in}} \quad (2)$$

where N_0 is the background electron concentration and N_b is the electron concentration inside the bubble. Aspects of both observational results and theoretical investigations have been recently reviewed [Basu and Kelley, 1979; Ossakow, 1979].

In this paper we would like to report our observations of these equatorial bubbles by means of radio propagation experiments and their effects on transionospherically propagated signals.

Experimental Results

A radio receiving station has been set up on the Campus of the Federal University of North Rio Grande, Natal, Brazil (35.23°W , 5.85°S , Dip -9.6°). At various times the station has been used to monitor different satellites, but in this paper we will report only some preliminary results based on the geostationary satellites SMS 1 and MARISAT 1. The satellite SMS 1, parked at 90°W , transmits a linearly polarized signal at 136.379 MHz and its signal has been used to measure the Faraday polarization rotation and hence the total electron content integrated along the path from the satellite to the ground terminal. The satellite MARISAT 1, parked at 15.4°W , transmits a circularly polarized wave at 257.55 MHz and its amplitude is received at two stations with an east-west spacing of 278 meters. This distance is very small and the scintillation patterns at two stations are nearly perfectly correlated. By the method of similar fades, the time displacement can be used to compute the drift velocity. Additionally, the amplitude of an L band signal at 1541.5 MHz transmitted by MARISAT 1 is also received at one station for scintillation studies.

Fig. 1 is a picture of the sample record of signals transmitted by SMS 1. The time goes from left to right with hourly values marked in LMT which corresponds to UT - 3 hr. The top channel shows the amplitude, the middle two channels show the plane of polarization in a ramp format with one displaced by 90° from the other, and the bottom channel gives effectively the middle portions of the polarization curve given by the two middle channels except the sense of the plane of polarization rotation is reversed. The top amplitude channel is approximately linear in dB and the full

scale change corresponds to about 18 dB. The sense of rotation in the two middle polarization channels is such that an upscale corresponds to a decrease in electron content. The full scale for the middle two channels corresponds to a polarization rotation of 180° or a change of 1.89×10^{17} electrons/m² in the total content. Two depletions can be easily seen in Fig. 1 and both are accompanied by the increased fading rate and the increased scintillation index. During the one month period from September 18, 1978 through October 19, 1978 ninety-four such isolated depletions have been identified. We shall call these isolated depletions bubbles since by inference they are most likely the very bubbles or plumes seen by radars and satellites. In the following are given the statistics of these 94 cases.

Fig. 2 is a histogram showing the occurrence time determined from the SMS 1 data such as Fig. 1. It is clear that these bubbles occur exclusively at night, between 19:00 hour and 04:00 hour, with a major peak in 20:00-22:00 hr. and perhaps a minor peak in 02:00-03:00 hr. This occurrence time is also compared in Fig. 2 with the average percentage of occurrence of scintillation at 257.55 MHz transmitted by the satellite MARISAT 1 with a scintillation index larger than 0.6 (supplied by private communication from J. P. Mullen Air Force Geophysics Laboratory). Here the Scintillation index used is that defined by Whitney et al. [1969]. The scintillation curve (shown dotted in Fig. 2) is shifted slightly in time so that it will have the same local time base as the histogram since

the sub-ionospheric points of the two propagation paths are separated by about 4° in longitude. An inspection of Fig. 2 shows that bubbles and high scintillation index occur nearly coincidentally in the early evening part of the scintillation activities but not in the latter part. This apparent discrepancy may be explained in part by the observation that early evening bubbles are longer lasting, occur more frequently and sometimes in successions, and generally are associated with almost continuous strong scintillations while bubbles observed past midnight occur less frequently and when they occur they are associated with strong scintillation activities interlaced with periods of weak scintillation activities such as shown in Fig. 1. Some of these points are revealed in Fig. 3.

During the two-week period shown in Fig. 3 the geostationary satellite SMS 1 was transmitting continuously and scintillation of the signal at 136 MHz were observed everyday. The onset of scintillation during this period was observed to fall within a narrow time window of 18:30 to 19:00 LT. This is clearly shown in Fig. 3 where a thin straight line is used to indicate presence of scintillation. The onset of scintillation is generally very sudden and the fluctuations usually become very intense in just a few minutes. This behavior should be contrasted with that occurring near the termination of scintillation where both the scintillation index and scintillation rate decrease gradually before complete cessation. Superposed on scintillation events

(indicated by thin lines in Fig. 3) are occurrences of ionospheric bubbles indicated by thick lines. The bubbles occurring before the local midnight are obviously more numerous than those occurring after the local midnight. Actually, the scintillation before midnight is usually so intense that it often makes scaling difficult. It is possible that some of the bubbles were actually present before midnight but not scaled as such because of obscuration from scintillation. It is interesting to note that for the night of October 12, 1978, no bubble was observed even though the scintillation was present for four hours, a duration somewhat shorter than normal.

A histogram depicting the duration of ionization depletions is given in Fig. 4. Most of these depletions last less than 10 minutes, but there are also a number of cases lasting longer than half an hour. These depletions have a distribution shown in Fig. 5. Most cases have a decrease in equivalent vertical electron content of less than 4×10^{16} electrons/m², but depletions as large as 1.1×10^{17} electrons/m² have also been observed. This is about 16% of the total diurnal change which has an average value of 7.0×10^{17} electrons/m². In an attempt to search for correlation between events with large depletions and events with long enduring bubbles a scatter plot is made in Fig. 6. The results seem to suggest that long enduring bubbles have a tendency to be associated with large depletions, but the converse may not be necessarily true.

The sample results of scintillation observations at 257.55 and 1541.5 MHz of signals transmitted by MARISAT 1 are shown in Fig. 7. The top three panels refer respectively to peak-to-peak amplitude fluctuations in dB, the rate of fluctuation in number of maximum per second determined from a record of one minute duration and eastward drift velocity in m/s, all analyzed from 257.55 MHz. The bottom panel refers to peak-to-peak amplitude fluctuations in dB at 1541.5 MHz. During the period of one hour forty minutes shown in Fig. 7, the scintillation at 257.55 MHz was very severe, hovering around 20dB (equivalent to S_4 scintillation index of 0.8) except perhaps around 00:15 during which the peak-to-peak fluctuations were dropped to about 5 dB (equivalent to S_4 scintillation index of 0.26). On the other hand, the fluctuation rate showed broad increases of which at least three can be identified in Fig. 7. The first one occurred from 00:30 to 01:00, the second one occurred from 01:00 to 01:20 and the third one started at about 01:20 and, because of missing data, did not finish. It is interesting to compare these broad increases in fluctuation rate at 257.55 MHz with the three broad increases in peak-to-peak scintillation index at 1541.5 MHz. A possible explanation on this close comparison will be given in the next section.

Discussions and Conclusion

The kind of equatorial ionization depletions observed by Faraday rotation technique discussed in this paper has been first reported by Koster [1976]. By monitoring VHF radio waves transmitted by the SIRIO geostationary satellite and received at Ascension Island, Klobuchar et al. [1978] have observed large bubbles which occasionally show a depletion over 20% of the total value. The arrival of bubbles is usually associated with the onset of strong amplitude scintillations in a manner similar to examples shown in Fig. 1. However, in our data we do not observe a large increase in the slope of the background electron content before the arrival of bubbles as reported by them. On the other hand, using multiple-frequency signals transmitted by the orbiting Wideband satellite, Rino et al. [1978] have observed only a few cases of simple electron content depletions, the kind reported in this paper; but scintillations at gigahertz frequencies are always associated with extremely large variations in electron content.

Based on one month of our data the appearance of a bubble was always accompanied by the increased fading rate, while the peak-to-peak fluctuations might or might not increase. According to the theory of wave propagation in random media, the fading rate depends on several factors. In the weak scatter limit the scattering of radio waves is controlled by the Fresnel filtering effect [Wernik and Liu, 1974], i.e. the scattered power comes mainly from irregularities of Fresnel size $l_F = \sqrt{z\lambda}$ where z is the distance between the region of irregularities and the receiver and λ is the radio wave-

length. If one further introduces the Taylor's frozen-in hypothesis (which seems to be supported by the observed high correlation between spaced stations), the fading rate in the weak scatter case is found to be proportional to v/ℓ_F where v is drift velocity of irregularities. The drift velocity determined by the spaced station observations has only slow variations such as shown in the third panel of Fig. 7 and cannot be used to explain the sudden increase in fading rate during the presence of a bubble. Since the observed scintillation is fairly severe, the above weak scatter theory is really not valid. According to the multiple scatter theory [Yeh et al., 1975], the correlation distance of the received amplitude may actually decrease with increased scintillation index due to randomization effects. Experimentally, the control of scintillation rate by the Fresnel filtering effect in the weak scatter case and by the randomization effect in the strong scatter case has already been demonstrated by multifrequency studies of scintillations [Umeki et al., 1977]. It is necessary to use the multiple scatter theory to explain the gross resemblance of increases in the fading rate at 257.55 MHz and increases in the peak-to-peak fluctuation at 1541.5 MHz shown in Fig. 7. This is because at 257.55 MHz the scintillation index is already saturating, any increase in irregularity strength perhaps due to arrival of a bubble must be accompanied by the increased fading rate signifying decorrelation by multiple scattering, while at 1541.5 MHz the weak scatter theory can still be employed and it predicts that an increased irregularity strength is accompanied by the increased scintillation index. This interpretation is further supported by the fact that the

fading rate should be proportional to \sqrt{f} in the weak scatter limit. In Fig. 7 when the scintillation index at 257.55 MHz was minimum at about 00:15 UT the fading rate was 0.18 peaks/sec. The fading rate at 1541.5 MHz was 0.38 peaks/sec, giving a ratio $(0.38/0.18)=2.1$. The square root of the frequency ratio is $(1541.5/257.55)^{1/2}=2.45$ which compares favorably with the fading rate ratio of 2.1. This implies that decorrelation by multiple scattering was responsible for observed high fading rate in Fig. 7. However, as mentioned earlier there were a few cases for which only the fading rate was increased, but not the scintillation index, during the appearance of a bubble. For these cases the present scintillation theory using the random media approach does not seem to be capable of offering an explanation. A new look at the scintillation mechanism may be desirable. Interference of grazing rays reflected from bubble ionization walls as proposed by Crain et al. [1979] may well be responsible for such cases.

The numerically computed bubbles [Ossakow et al., 1979] show a nearly constant depletion of about 1.0×10^{11} electrons/ m^3 density for a region extending in 110 km in height. This amounts to an electron content depletion of 1.1×10^{16} electrons/ m^2 which is near the lower boundary of the most probable depletions given in Fig. 5. Based on our observations, depletions as large as 10 times larger than those computed by Ossakow et al. [1979] are possible.

The observed bubbles as shown in Fig. 4 have an average duration of 8 minutes. For a drift velocity of 150 m/sec, this corresponds to an average size of about 70 km. Inside each bubble the electron depletion has an average value of 3×10^{16} electrons/m² as shown in Fig. 5. This gives the average depletion inside each bubble a value of about 2×10^{21} electrons per meter in the north-south direction. Airglow observations indicate a north-south extension of at least 1200 km [Whitney et al., 1978; Weber et al., 1978], which value we will take. The total depletion for each bubble has then an average value of 3×10^{27} electrons, certainly an enormous value even though it is about 5 orders of magnitude smaller than the totality of all electrons around the whole globe in the ionosphere.

Acknowledgement

This research was sponsored by the Army Research Office under grant DAAG 29-78-G-0101. We wish to thank J. P. Mullen of the Air Force Geophysics Laboratory for sharing some of his data with us before publication. The polarimeter was installed by personnel from Itapetinga Radio Observatory under the direction of Pierre Kaufmann and the field station maintenance was supervised by E. Bonelli of the Federal University of North Rio Grande. The assistance of Francis J. Gorman, Jr. and K. S. Yang in electronic equipment is acknowledged with pleasure.

References

- Aarons, J., Equatorial scintillations: A review, IEEE Trans. Ant. Prop. AP-25, 729, 1977.
- Basu, S. and S. Basu, Correlated measurements of scintillations and in-site F region irregularities from OGO-6, Geophys. Res. Lett., 3, 681, 1976.
- Basu, S. and M. C. Kelley, A review of recent observations of equatorial scintillations and their relationship to current theories of F-region irregularity generation. To appear in Radio Science, 1979.
- Crain, C. M., H. G. Booker, and J. A. Ferguson, Use of refractive scattering to explain SHF scintillations, Radio Sci., 14, 125-134, 1979.
- Dyson, P. L., J. P. McClure and W. B. Hanscom, In-situ measurements of the spectral characteristics of F-region ionospheric irregularities, J. Geophys. Res., 79, 1495, 1974.
- Kelley, M. C., G. Haerendel, H. Kappler, A. Valenzuela, B. B. Balsley, D. A. Carter, W. L. Ecklund, C. W. Carlson, B. Havsler and R. Torbert, Evidence for Rayleigh-Taylor type instability and upwelling of depleted density regions during equatorial Spread F, Geophys. Res. Letts., 3, 448, 1976.
- Klobuchar, J. Aarons, E. Weber, L. Lucena and M. Mendillo, Total electron content changes associated with equatorial irregularity plumes. Presented at National Radio Science Meeting, paper G4-2, 6-9 Nov. 1978, Boulder, Colorado.
- Koster, J. R., Study of the equatorial ionosphere. Report AFGL-TR-77-0165, University of Ghana, Legon, Ghana, 1976.
- Liu, C. H. and K. C. Yeh, Low-frequency waves and gradient instabilities in the ionosphere, Phys. Fluids, 9, 1407, 1966a.
- Liu, C. H. and K. C. Yeh, Gradient instabilities as possible causes of irregularities in the ionosphere, Radio Sci., 1, 1283, 1966b.
- McClure, J. P., W. B. Hanson and J. H. Hoffman, Plasma bubbles and irregularities in the equatorial ionosphere, J. Geophys. Res., 82, 2650, 1977.
- Morse, F. A., B. C. Edgar, H. C. Koons, C. J. Rice, W. J. Heikkila, J. H. Hoffman, B. A. Tinsley, J. D. Winningham, A. B. Christensen, R. F. Woodman, J. Pomalaza and N. R. Teixeira, EQUION, an equatorial ionospheric irregularity experiment, J. Geophys. Res., 82, 578, 1977.

- Ossakow, S. L., S. T. Zalesak and B. E. McDonald, Nonlinear equatorial spread F: Dependence on altitude of the F peak bottomside background electron density gradient scale length, *J. Geophys. Res.*, 84, 17, 1979.
- Ossakow, S. L., A review of recent results on spread F theory. NRL Memorandum Report 3909, January 1979.
- Ott, E., Theory of Rayleigh-Taylor bubbles in the equatorial ionosphere, *J. Geophys. Res.*, 83, 2066-2070, 1978.
- Rino, C. L., R. C. Livingston and J. Owen, The structure of equatorial gigahertz scintillation. Presented at National Radio Science Meeting, paper G4-4, 6-9 Nov. 1978, Boulder, Colorado.
- Röttger, J., The macroscale structure of equatorial irregularities, *J. Atmos. Terr. Phys.*, 38, 97-102, 1976.
- Umeki, R., C. H. Liu and K. C. Yeh, Multifrequency studies of ionospheric scintillations, *Radio Sci.*, 12, 311-317, 1977.
- Weber, E. J., J. Buchau, R. H. Eather, and S. B. Mende, North/south aligned equatorial airglow depletions, *J. Geophys. Res.*, 83, 712-716, 1978.
- Wernik, A. W. and C. H. Liu, Ionospheric irregularities causing scintillation of GHz frequency radio signals, *J. Atmos. Terr. Phys.*, 36, 871-879, 1974.
- Whitney, H. E., J. Aarons and C. Malik, A proposed index of measuring ionospheric scintillations, *Planet. Space Sci.*, 17, 1069, 1969.
- Whitney, H. E., J. Aarons, J. Buchau, E. J. Weber, and J. P. McClure, The evolution of scattering equatorial F-region irregularities and resultant effects on trans-ionospheric radio waves. AGARD Conference Proceedings No. 244, Aspects of Electromagnetic Wave Scattering in Radio Communications edited by A. N. Ince, paper 8, 1978.
- Woodman, R. F. and S. Basu, Comparison between in-situ spectral measurements of F-region irregularities and backscatter observations at 3 m wavelength, *Geophys. Letts.*, 5, 869, 1978.
- Woodman, R. F. and C. LaHoz, Radar observations of F-region equatorial irregularities, *J. Geophys. Res.*, 81, 5447, 1976.
- Yeh, K. C., C. H. Liu, and M. Y. Youakim, A theoretical study of the ionospheric scintillation behavior caused by multiple scattering, *Radio Sci.*, 10, 97-106, 1975.

- Fig. 1 Sample data of 136.379 MHz signals transmitted by the geostationary satellite GOES 1 and received at Natal, Brazil on October 16, 1978. The top channel shows the amplitude. The scale is approximately linear in dB with a full scale deflection corresponding to an amplitude change of 18 db. The middle two channels show the plane of polarization in a ramp format with one channel displaced by 90° relative to the other. The full scale deflection corresponds to a rotation of the plane of polarization by 180° . In both middle channels, an upscale indicates a decrease in electron content. The bottom channel gives essentially the middle portions of two middle channel with the sense of polarization reversed.
- Fig. 2 Histogram showing the occurrence time of ionization bubbles determined from data such as shown in Fig. 1 for the period 9/18/78 through 10/19/78. The dotted curve referring to the right scale depicts the average occurrence percentage of scintillation index exceeding 0.6 at 257.55 MHz transmitted by the geostationary satellite MARISAT 1 and received at Natal for the same period but in a different year.
- Fig. 3 Diagram showing occurrence of scintillation (indicated by thin lines) and of bubbles (indicated by thick lines) for a two-week period in October 1978.
- Fig. 4 Histogram showing bubble durations deduced from data such as shown in Fig. 1 for the same period shown in Fig. 2.
- Fig. 5 Histogram showing depletions of the total electron content inside the bubbles for the same period shown in Fig. 2.
- Fig. 6 Scatter plot showing electron content depletion vs. bubble duration.
- Fig. 7 Scintillation observations on October 18, 1978 at Natal of signals transmitted by the geostationary satellite MARISAT 1 at 257.55 MHz and 1541.5 MHz.

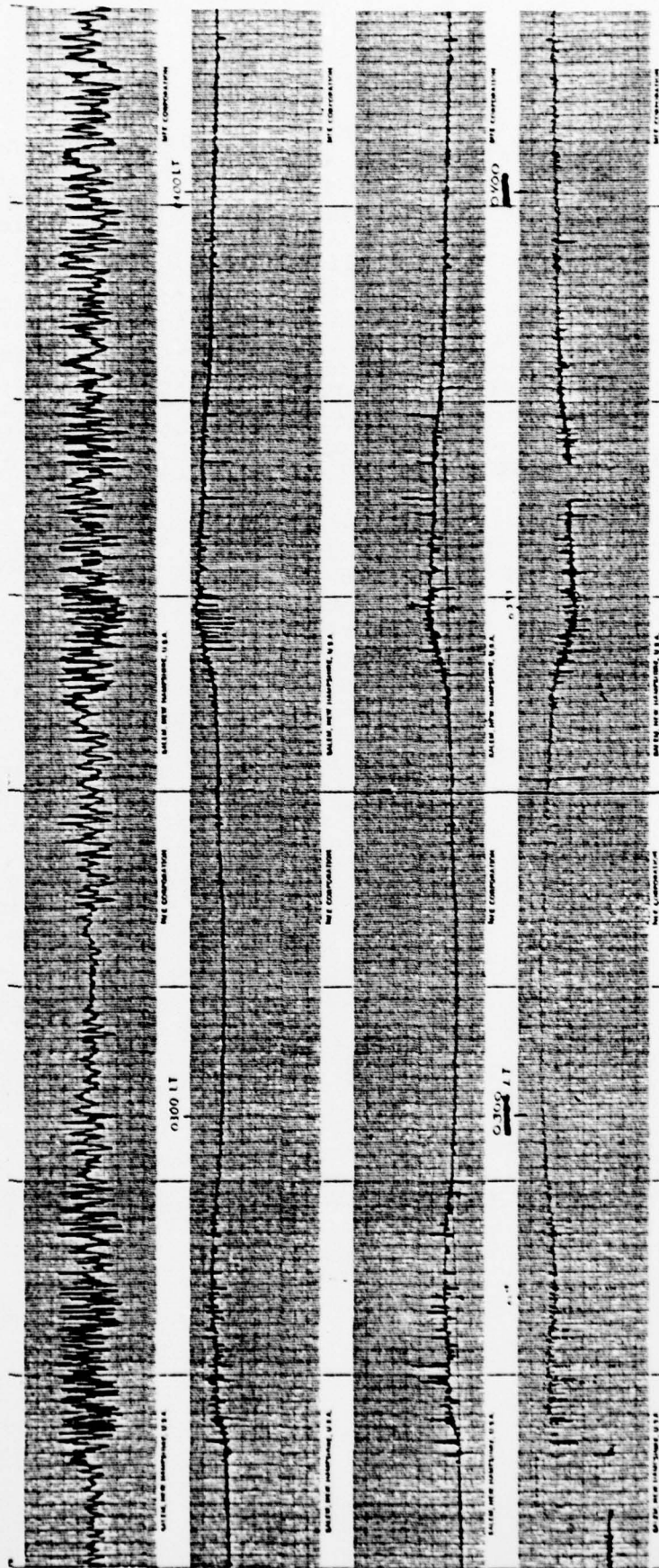


Fig. 1

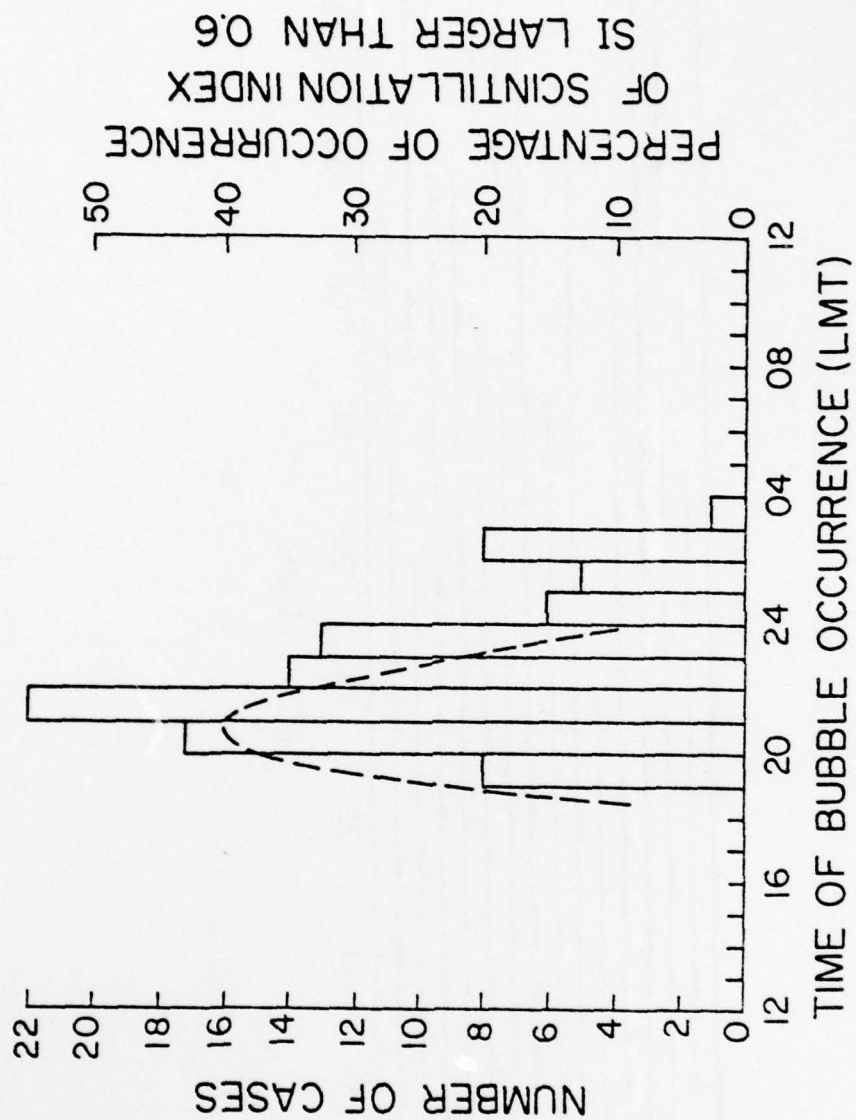


Fig. 2

AD-A076 622

ILLINOIS UNIV AT URBANA-CHAMPAIGN DEPT OF ELECTRICAL --ETC F/G 20/14
STUDIES OF EQUATORIAL SCINTILLATION PROBLEMS.(U)

SEP 79 K C YEH , C H LIU

DAAG29-76-6-0286

UNCLASSIFIED

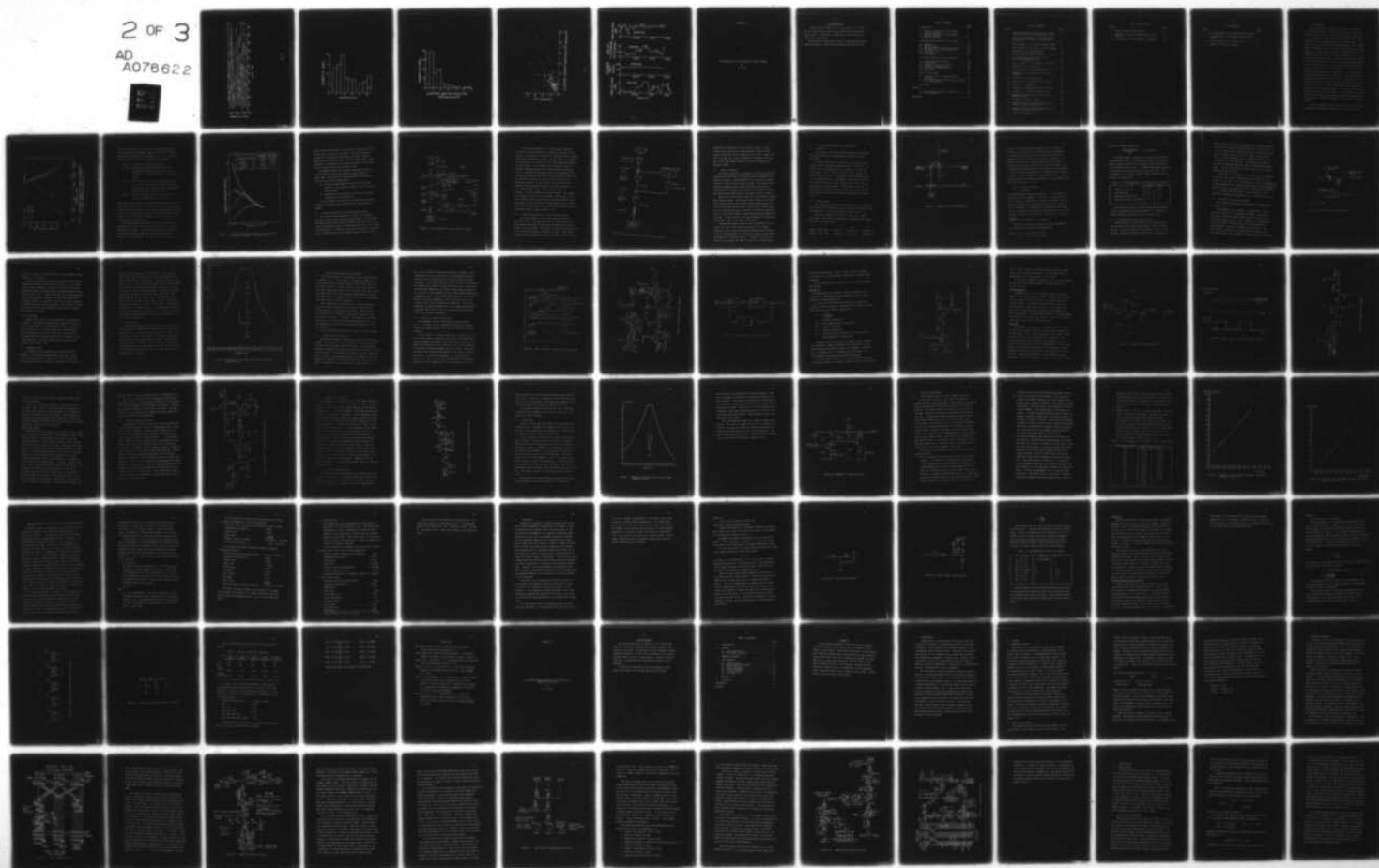
UILU-ENG-79-2559

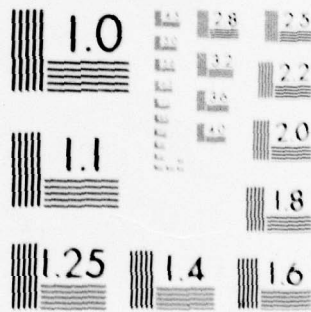
ARO-14260.8-ELX

NL

2 OF 3

AD
A076622





MICROCOPY RESOLUTION TEST CHART
NATIONAL BUREAU OF STANDARDS-1963-A

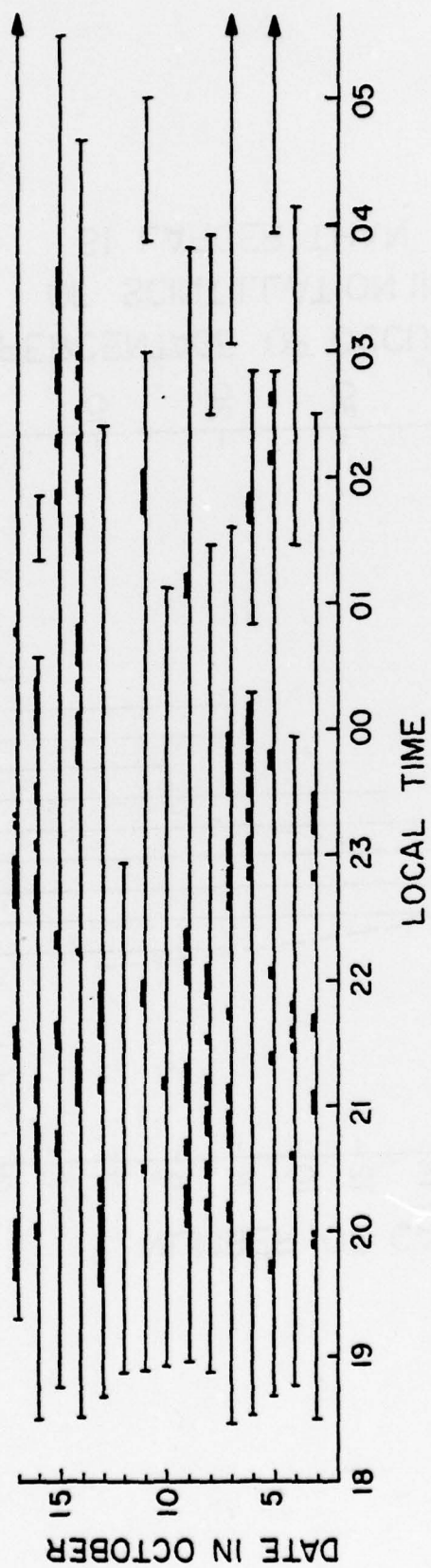
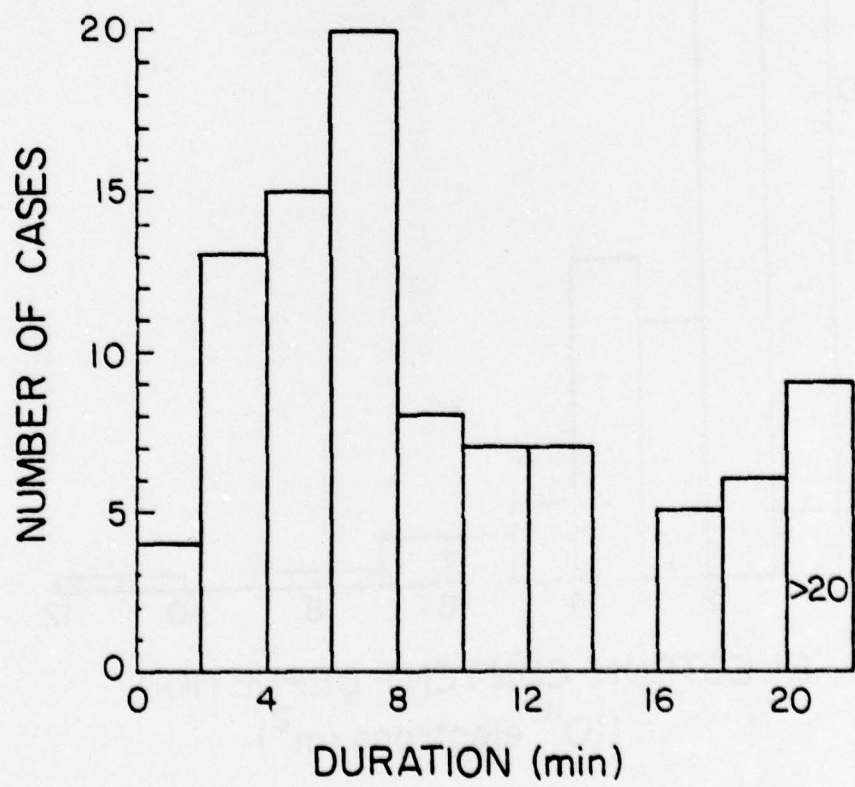
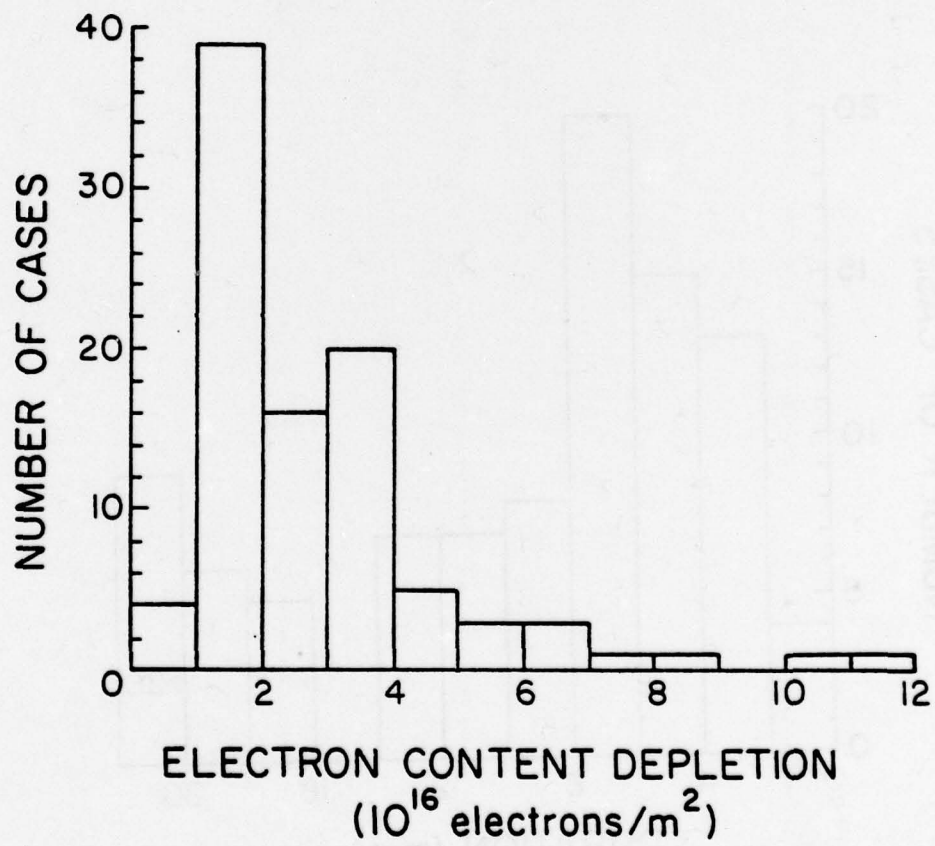


Fig. 3





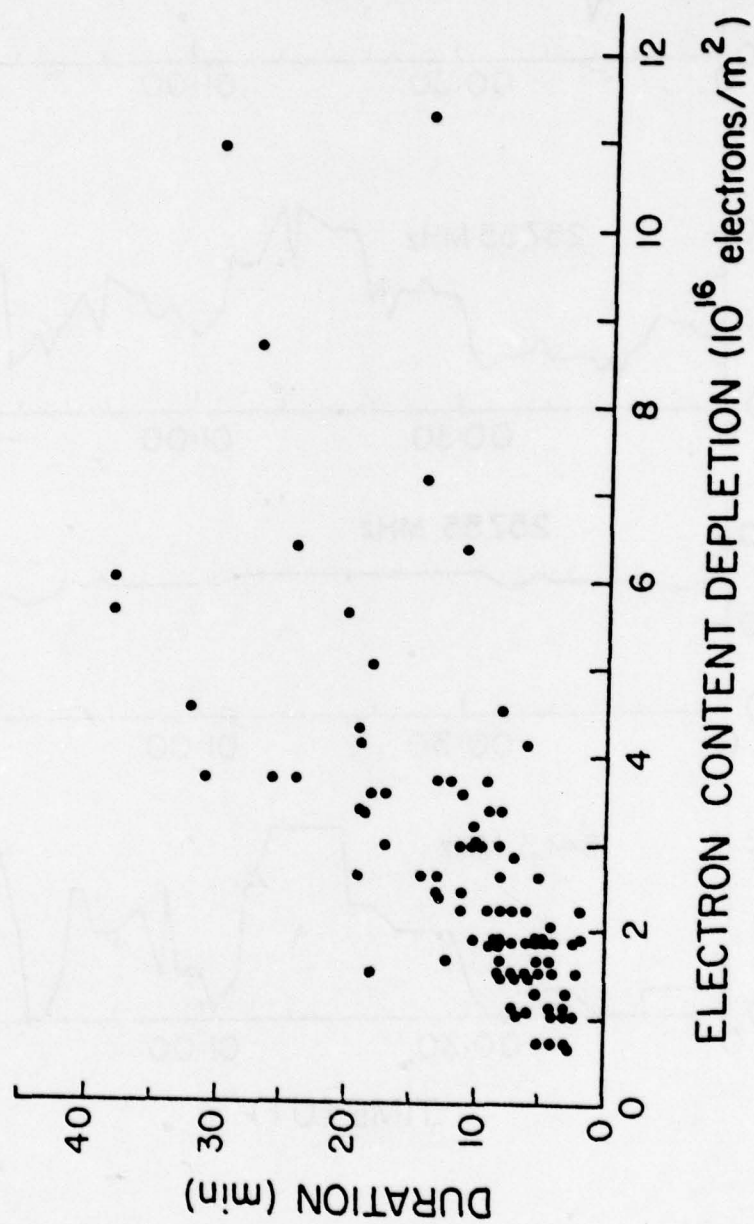
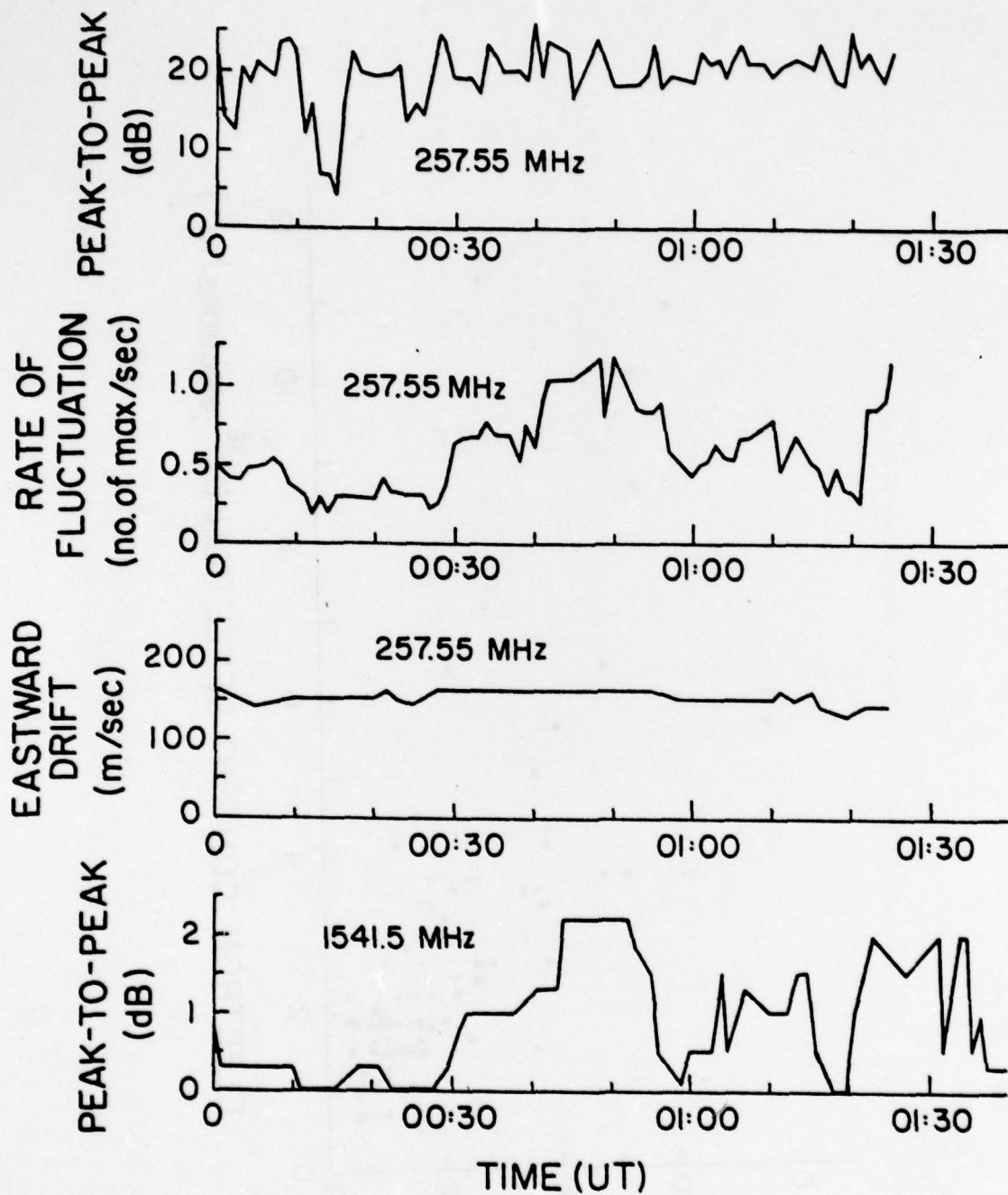


Fig. 6



Appendix G

IMPLEMENTATION OF AN L-BAND AND C-BAND RECEIVER

by

Y. P. Wei

ACKNOWLEDGEMENT

I would like to thank Dr. K. C. Yeh and Mr. K. S. Yang for the great help and advice they gave me while working on this project. I also want to thank Mrs. Linda Houston for typing this manuscript.

This work was supported by the U.S. Army Research Office under the grant No. DAAG 29-76-G-0286 and DAAG 29-78-G-0101.

TABLE OF CONTENTS

	Page
1. Introduction	1
1.1 General description of the C-band receiver system	5
1.2 General description of the L-band receiver system	7
1.3 Model B receiver.	9
2. A Detailed Description of the Frontend	10
2.1 Antenna	10
2.2 Demultiplexer	10
2.3 The frontend of the C-band receiver	13
2.4 3850 MHz phase locked oscillator.	14
2.5 RF Preamp	16
2.6 Bandpass filter	16
2.7 Mixer M2040	17
3. A Detailed Description for the Backend	19
3.1 10 MHz Crystal Oscillator	19
3.2 50 MHz PLL.	20
3.3 Frequency doubler and driver.	31
3.4 Frequency divider by six.	33
3.5 116 2/3 MHz bandpass filter	33
3.6 Amplifiers.	35
4. Receiver Performance	39
4.1 Linearity test of C-band & Model B receivers	39
4.2 Gain and signal-to-noise ratio in C-band and L-band systems.	44
5. Conclusion	49
Appendix.	51
(1) Test points and check of phase lock.	51
(2) 31 db attenuator	57
References.	62

LIST OF FIGURES

Figure		Page
1	Correlation distance as a function of frequency [after Yeh, Liu and Youakim, 1975]. . .	2
2	Normalized correlation intervals as functions of signal frequency [after Umeki et al., 1977]	4
3	Block diagram of the C-band receiver system. .	6
4	Block diagram of the L-band receiver system. .	8
5	Schematic of the demultiplexer	11
6	3850 MHz phase-locked oscillator	15
7	The amplitude response curve of the 3945.5 MHz bandpass filter	18
8	Block diagram of 10 MHz crystal oscillator . .	21
9	Schematic of the 50 MHz PLL.	22
10	Block diagram of a phase-locked loop	23
11	Schematic of the oscillator circuit in 50 MHz PLL	25
12	Schematic of 50 MHz amplifier.	26
13	Analog signal is converted to TTL level. . . .	27
14	Schematic of comparator.	29
15	Schematic of frequency doubler and driver. . .	32
16	Schematic of frequency divider by six.	34
17	Amplitude response curve of 116 $\frac{2}{3}$ MHz bandpass filter.	36
18	Schematic of model B driver.	38
19	Linearity test for C-band (backend) and model B receiver (plug-in #1).	42
20	Linearity test for C-band (backend) and model B receiver (plug-in #2).	43
21	Power level detector	52

LIST OF FIGURES CONT.

Figure		Page
22	Setup of power level detector.	53
23	Schematic of the 31 db attenuator in 1 db steps.	58
24	Configuration of the resistive π -network . . .	59

LIST OF TABLES

Table		Page
1	The measurements on the demultiplexer network.	13
2	Linearity test of the backend of the C-band receiver	41
3	The measurements on the test points.	54
4	Design of 31 db step attenuator.	60

1. Introduction

When a radio wave propagates through the ionosphere, the sometimes present irregularities can scatter radio wave energy and will cause fluctuations in the wave parameters such as amplitude, phase, direction of arrival, etc. This is known as the ionospheric scintillation phenomenon. The study of the scintillation of transionospheric radio signals plays an important role in satellite communications and geophysics. In these applications, it is important to know the dependence of scintillation on radio frequencies. Yet, early experiments were made mostly in the HF & VHF ranges, usually with a single frequency. Some with simultaneous measurements at two frequencies and very few of these measurements were made at several widely spaced frequencies. Because of the expected strong dependence on frequency, it is anticipated that multiple scattering may take place in the ionosphere at a frequency of 500 MHz or even higher. Theoretically, the multiple scattering effects have been investigated numerically [Yeh and Liu, 1975]. It was found that for the parameters chosen and for frequencies higher than 1 GHz, the correlation distance decreased with frequency. For frequencies less than about 500 MHz, multiple scattering played an important role in making the correlation distance to increase with frequency. (Fig. 1)

In 1976, simultaneous scintillation data from the ATS-6 Radio Beacon Experiments for signals at 40, 140, 360 MHz

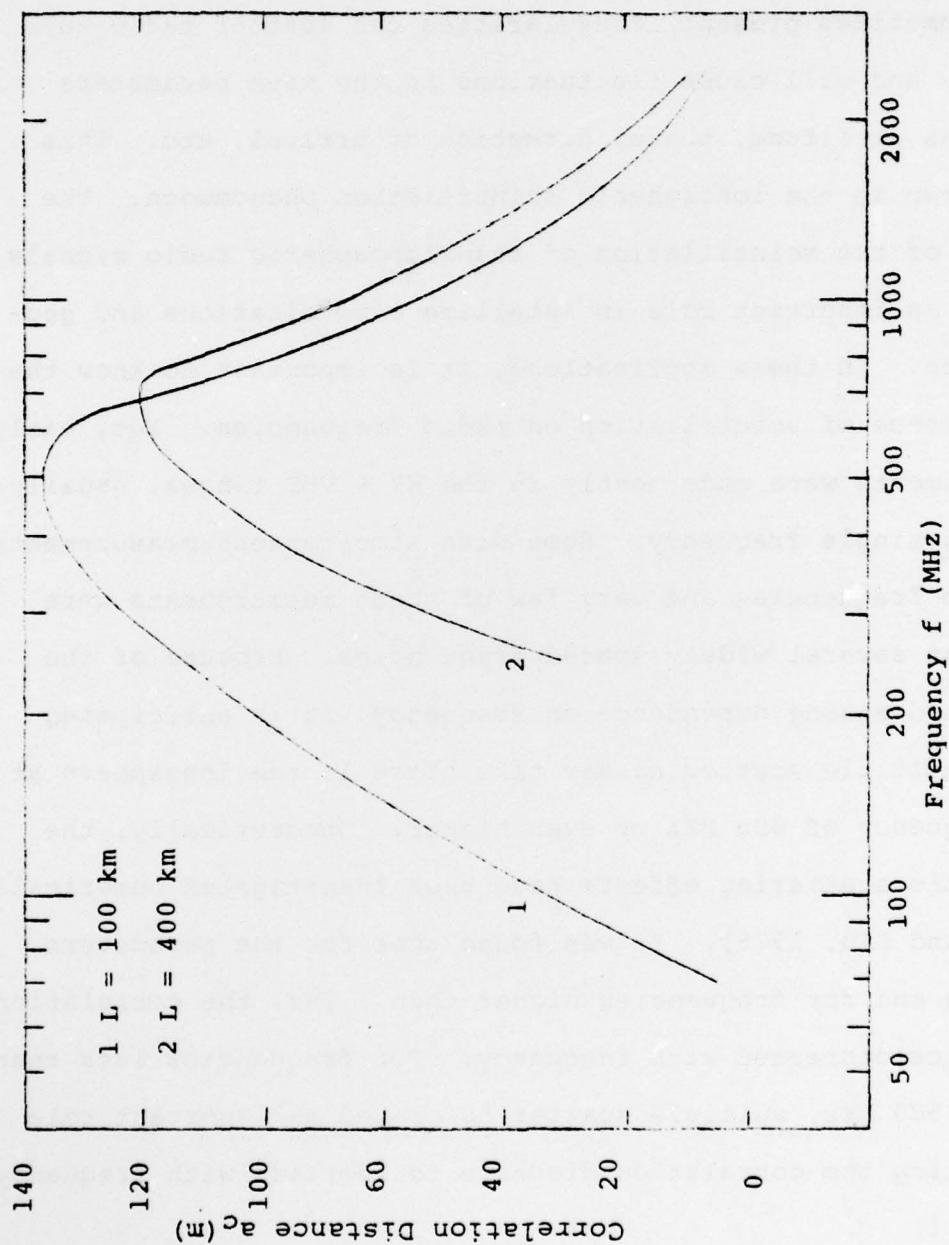


Figure 1. Correlation distance as a function of frequency.
 $r_0 = 300$ m. $(\Delta N/N_0)^2)^{1/2} = 5\%$, $z_0 = 250$ km,
 $f = 10$ MHz, power-law spectrum (2).

offered an opportunity to study the frequency dependence of the scintillation phenomenon [Umeki et al., 1977]. Their results are reproduced here and shown in Fig. 2. From this figure, the four curves can be analyzed as follows:

- Curve 1: Fresnel zone relation dominates.
- Curve 2: With stronger scintillations, multiple scattering becomes more effective. In low frequency, correlation interval τ decays more slowly.
- Curve 3: The scintillation at the low frequency range is so strong that multiple-scattering effect dominates in the region, but for high frequency, single scattering is still valid.
- Curve 4: Multiple scattering effect dominates in all frequency ranges shown in the figure.

The observational results compared favorably with theoretical predictions given in Fig. 1. If we want to get the simultaneous scintillation data in GHz range to study the multiple scattering effect, then measurements at L-band and C-band frequencies will be useful to see how the observational data are compared with the theoretical predictions.

The understanding and prediction of the scintillation phenomenon are vital to the design and operation of satellite communication systems. On the other hand, the scintillation data contain valuable information about the physics and dynamics of the ionosphere. The project is concerned with

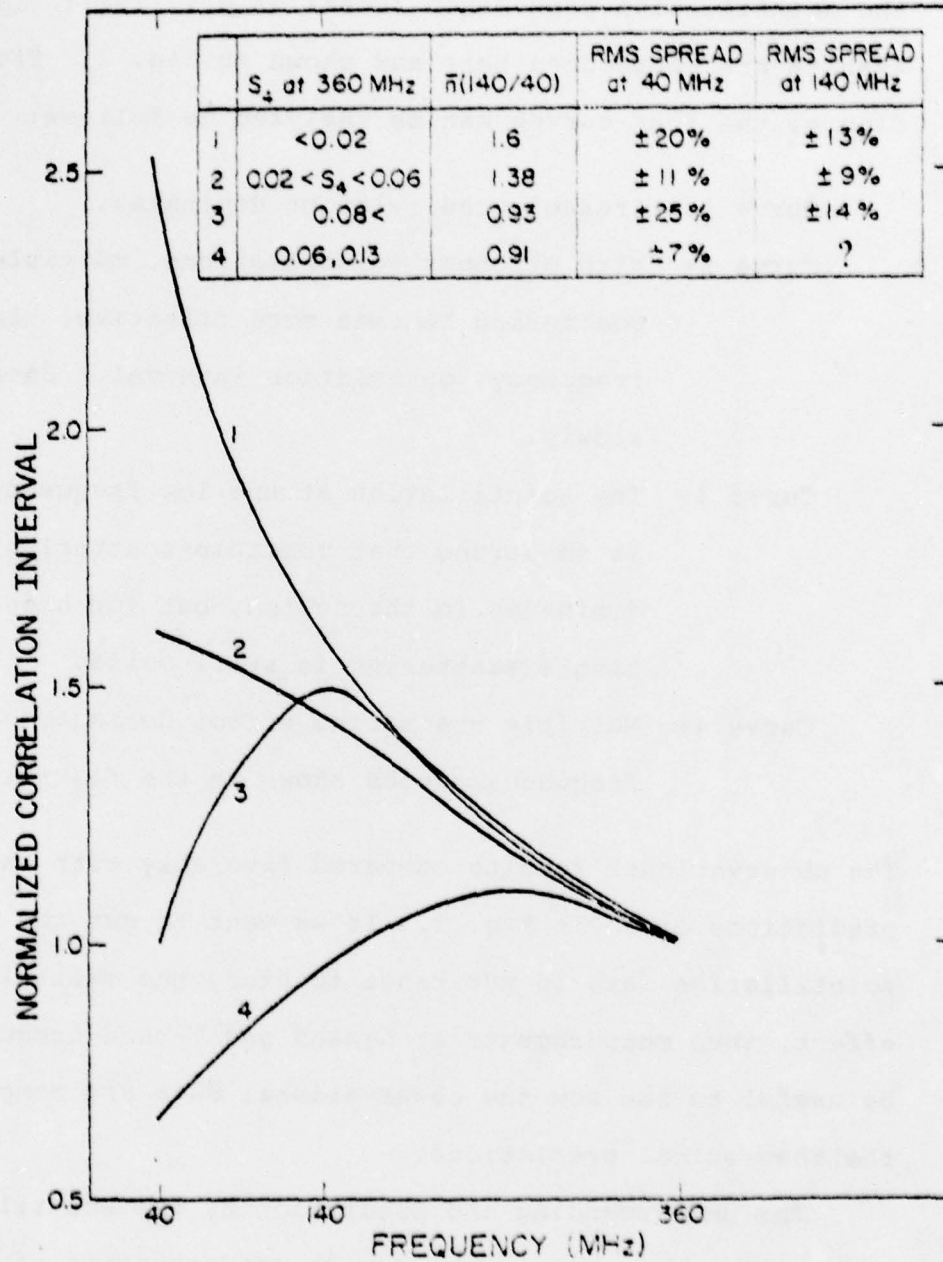


Figure 2. Normalized correlation intervals as functions of signal frequency [R. Umeki, et al.]

making these measurements at an equatorial station where the scintillation is known to be strong. For this purpose, a cooperative program with a Brazilian university (Federal University of North Rio Grande) has been established. Both equipment and personnel will be sent to Brazil to help establish the field station and to collect data.

The MARISAT satellite transmits continuously both the L band signals at 1541.5 MHz and the C-band signals at 3945.5 MHz. The L-band and C-band systems are designed to carry out two types of experiments:

- (1) Designed toward obtaining specific information needed to study specific aspects of the scintillation problem.
- (2) Designed for the purpose of collecting long-term statistics of the phenomenon.

In the following two sections, we shall describe simply the block diagrams of the C-band and the L-band receiver systems.

1.1 General description of C-band receiver system

The antenna system composed of antenna and parabolic reflector receives the C-band and L-band signal simultaneously. The demultiplexer separates the C-band signal from the L-band signal and channels them to corresponding receiver. The C-band receiver system is composed of the basic frontend and the backend. A block diagram of the C-band system is shown in Fig. 3.

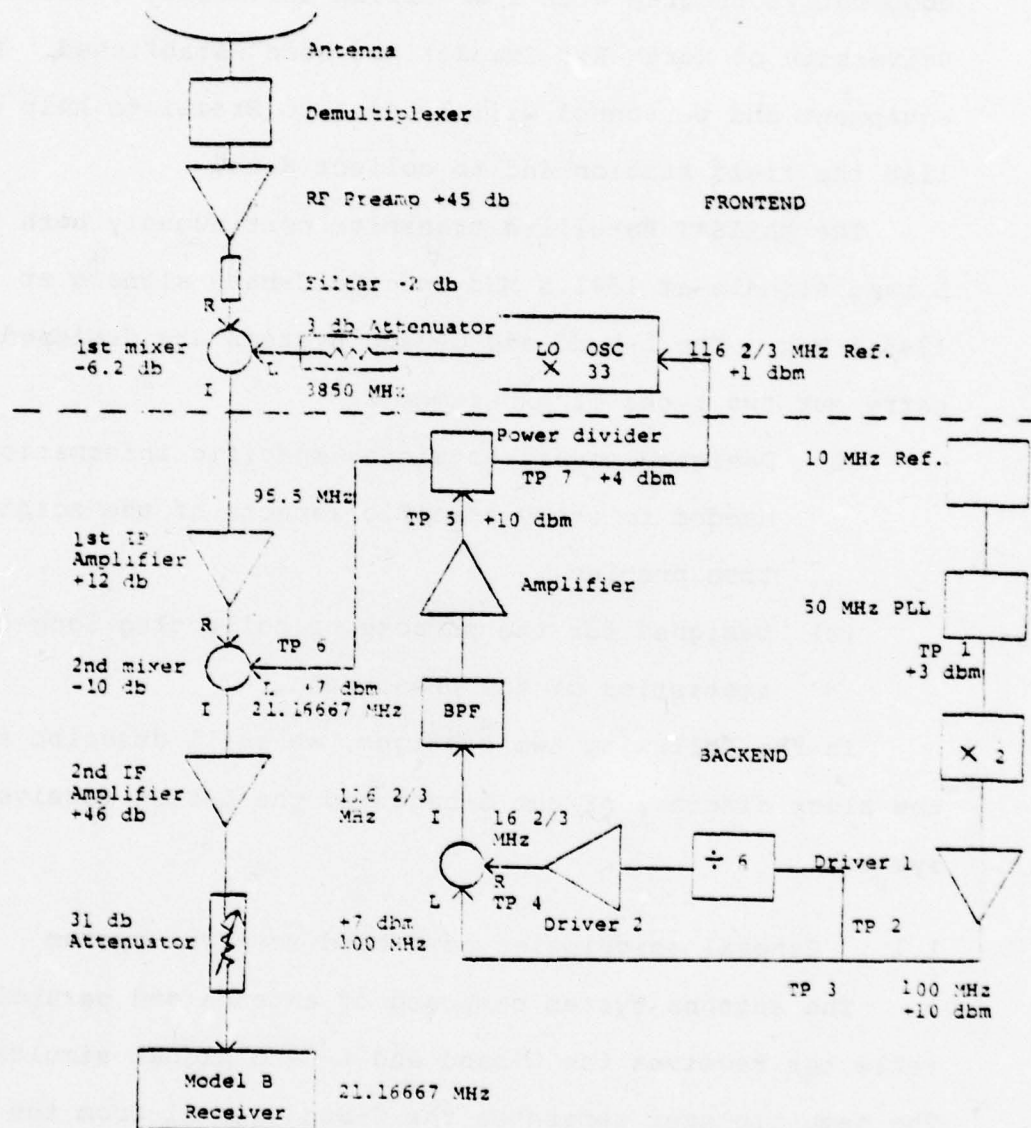


Figure 3. Block diagram of C-band receiver system.

In the backend there is a 10 MHz crystal reference oscillator which determines the operating frequency of the system. The frontend is basically a frequency down converter requiring a 3850 MHz LO signal. This LO signal is generated by multiplying by 33 times a $116 \frac{2}{3}$ MHz reference supplied by the backend. In the backend this reference signal is directly synthesized from the 10 MHz reference oscillator output. The 3945.5 MHz C-band signal is preamplified in a low noise transistor amplifier, then filtered and mixed with the 3850 MHz reference to generate the 95.5 MHz IF that feeds the backend. In the backend, this 95.5 MHz IF is further down converted with the $116 \frac{2}{3}$ MHz reference to a $21 \frac{1}{6}$ MHz 2nd IF signal. Then finally a model B receiver is used to detect this 2nd IF signal. The output of the model B receiver (AGC voltage) goes directly to the multi-channel digital data logging system with the voltage range from 0.2V to 0.8V and a signal dynamic range of 20 db. This multi-channel data logging system is fully described in a separate report [Yang and Hearn, 1977].

1.2 General description of L-band receiver system

The block diagram of the L-band receiver system is shown in Fig. 4. The reference for the L-band receiver is the crystal controlled LO oscillator MO-108XC with the frequency set at 1430 MHz. This signal is derived by multiplying a 102.14286 MHz reference frequency 14 times. The L-band signal is first preamplified and then mixed with the 1430 MHz

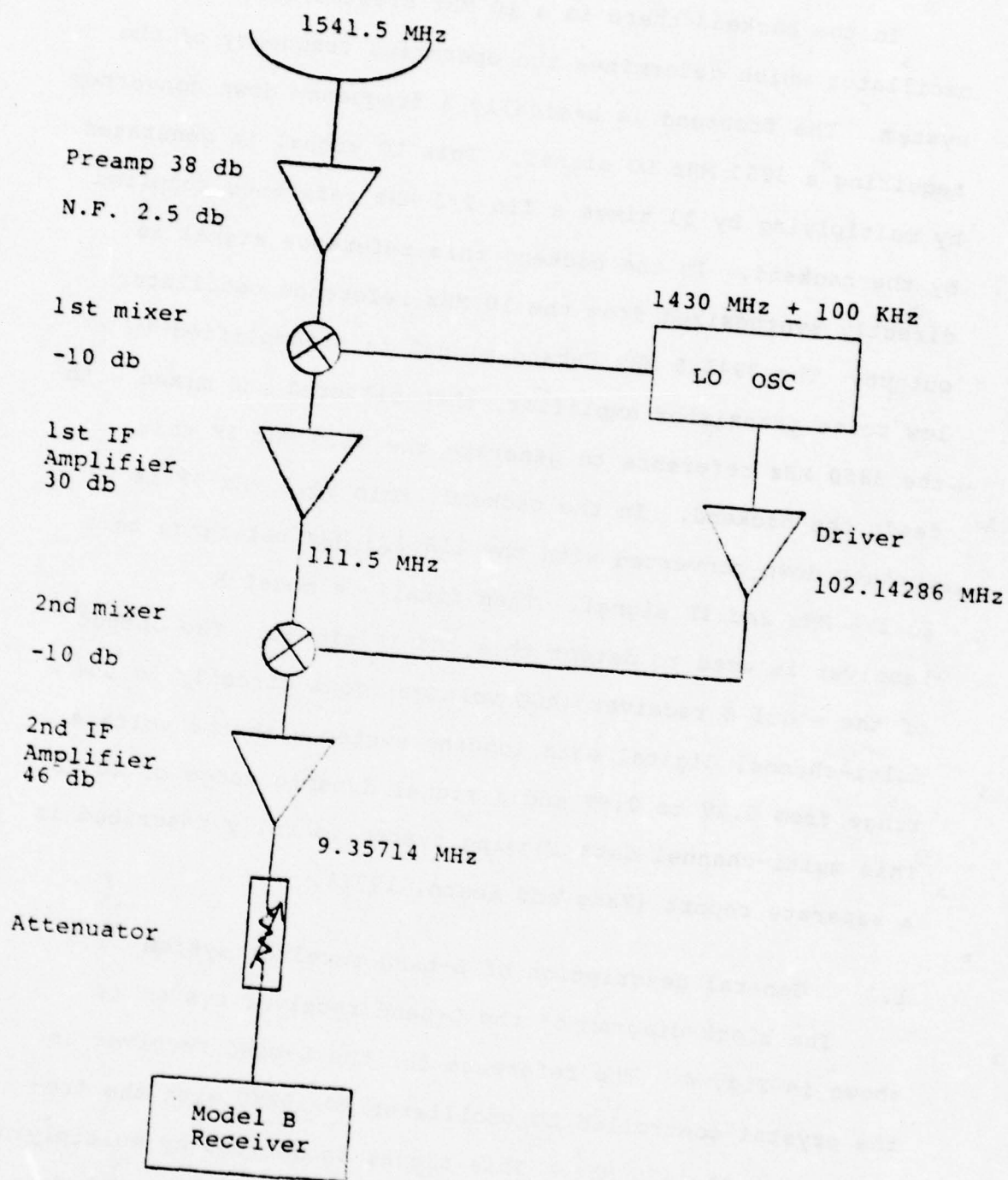


Figure 4. Block diagram of L-band receiver system

reference and resulted in a 111.5 MHz IF output. It is further down converted by reference again to the 102 MHz signal to form the 2nd IF signal at 9.35714 MHz. Again, the 2nd IF is fed into a model B receiver to generate a DC output to the data logging system for eventual recording on magnetic tapes.

1.3 Model B receiver

The model B receiver is designed to receive sub-microvolt signals from satellites in conjunction with ionospheric research activities. The bandwidth of the receiver is established at 4 KHz by fixed ceramic filters. The receiver employs an automatic gain control such that the output is logarithmically related to the level of the incoming signal. The relation has been found to be linear (in db) in Chap. 4.

The output of the model B goes to a multi-channel digital data logging system. The desired input voltage to the first four channels of the data logging system should range from 0.2V to 0.8V into 100,000 ohms. Checking the voltage range 0.2V to 0.8V with the Figs. 19 and 20, we find the operating point of the C-band receiver input should be approximately at -100 dbm. We can use the 31 db step attenuator to adjust the input power level to the model B receiver.

Although the model B receiver has a bandwidth of only 4 KHz, the input of the model B receiver in the C-band system will fall within this bandwidth because the stability of the 10 MHz reference is 10^{-11} and the signal coming from the satellite is precise enough. In Chap. 4 we will talk about how to operate the model B receiver in C-band system.

2. A Detailed Description of the Frontend

2.1 Antenna

The antenna used in the C-band system is an AEL Model APN 101B antenna for the parabolic reflector AEL model ALN 122B.

The model APN 101B is a pyramidal log periodic feed antenna with a frequency operating range 1 to 11 GHz. At 4 GHz, its 3 db beamwidth for the E plane is 58° and for the H plane is 61° . It has 8.7 db gain for a linear isotropic source at 4 GHz. The VSWR at 4 GHz frequency signal is 1.9 referenced to 50Ω impedance. The antenna receives the C-band and L-band signals simultaneously and they are separated by a demultiplexer. C-band signals then go into the C-band receiver and L-band signals the L-band receiver. The parabolic reflector ALN 122B has an effective diameter 6 ft.

2.2 Demultiplexer

The primary function of the demultiplexer is to separate the L-band and the C-band signals coming from the feed antenna. The schematic of this demultiplexer is shown in Fig. 5.

The input frequency in C-band is 3945.5 MHz, L-band 1541.5 MHz. The table of wavelength, half-wavelength, quarter wavelength is shown below:

	f	λ	$\lambda/2$	$\lambda/4$
L-band	1541.5 MHz	19.4481 cm	9.72405 cm	4.862025 cm
C-band	3945.5 MHz	7.59834 cm	3.79917 cm	1.899585 cm

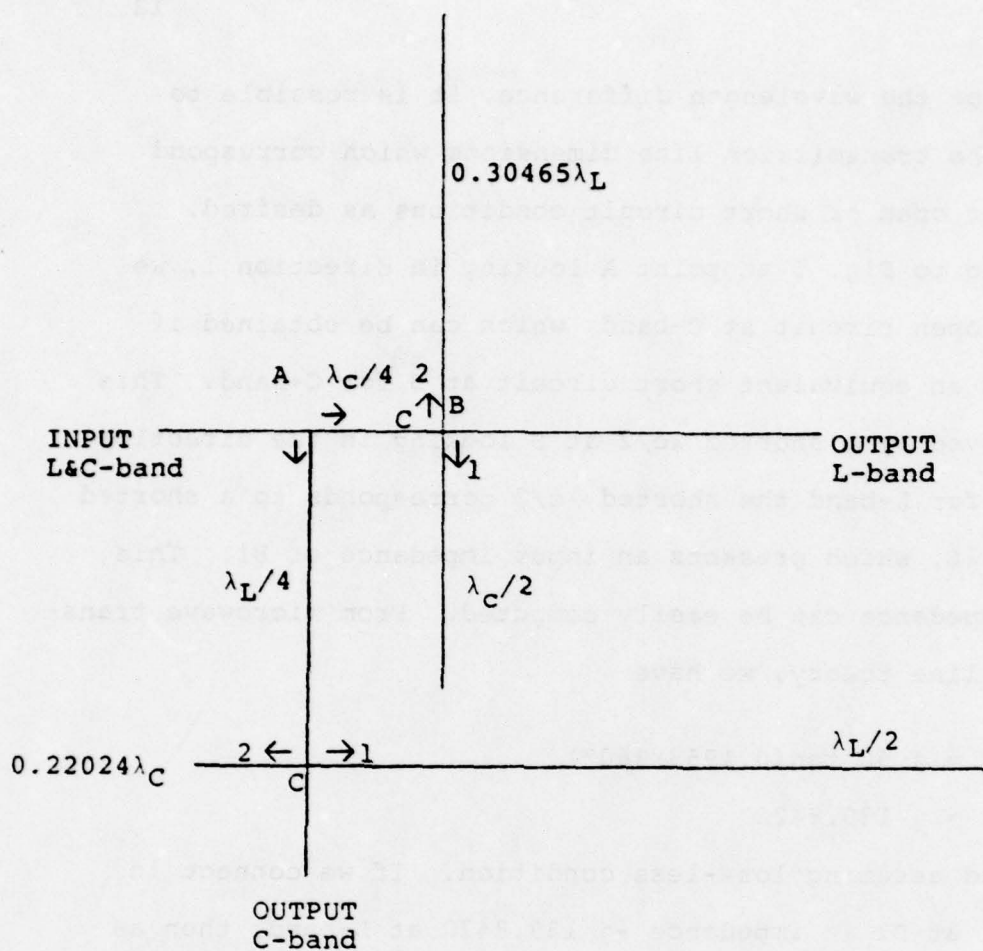


Figure 5. Schematic of the demultiplexer

Because of the wavelength difference, it is possible to create the transmission line dimensions which correspond to either open or short circuit conditions as desired. Referring to Fig. 5 at point A looking in direction 1, we need an open circuit at C-band, which can be obtained if there is an equivalent short circuit at B for C-band. This is achieved by a shorted $\lambda_c/2$ at B looking in the direction 1. But for L-band the shorted $\lambda_c/2$ corresponds to a shorted $0.19535 \lambda_L$, which presents an input impedance of B_1 . This input impedance can be easily computed. From microwave transmission line theory, we have

$$\begin{aligned} z_{B_1} &= j 50 \tan(0.1953 \times 360^\circ) \\ &= j 139.842\Omega \end{aligned}$$

at L-band assuming loss-less condition. If we connect in parallel at B_2 an impedance $-j 139.842\Omega$ at L-band, then as far as L-band is concerned, the parallel combination B_1 and B_2 will give infinite impedance since they are in parallel and in resonance. To achieve this required parallel impedance by a shorted line requires a phase shift looking in the direction 2 at B of $180^\circ - 70.3257^\circ = 109.6743^\circ$ or a length of $\frac{109.6743^\circ}{360^\circ} \lambda_L = 0.3046501 \lambda_L = 5.92488 \text{ cm.}$

At point A looking in direction 2, the same reasoning will apply except L and C are interchanged.

$$\begin{aligned} \text{At } C_1 \quad X_{C_1} &= j 50 \tan(1.27976 \times 360^\circ) \\ &= -j 264.275\Omega \text{ at C-band} \end{aligned}$$

Hence the required length C_2 is

$$\frac{(180^\circ - 100.7135^\circ)}{360^\circ} \times \lambda_c = 1.67346 \text{ cm}$$

This demultiplexer network was actually built with two halves made of brass. In each half, hollows of cylindrical shape to match the UG-25 A/U connector were made according to our design shown in Fig. 5. Trimmer screws were installed to maximize isolation and minimize insertion loss. The measurements on the demultiplexer network were made and the results are shown below.

Table 1. The measurements on the demultiplexer network.

	C band	L band
Insertion loss (db)	0.2	0.45
Isolation (db)	29.5	23.5
VSWR with matched load	1.7	1.75
VSWR with antenna and cable	1.9	3.5

The mismatch as shown between antenna and the demultiplexer is subsequently further trimmed off by inserting a sliding double stub tuner to minimize signal loss.

2.3 The frontend of the C-band receiver

The frontend of C-band receiver is contained inside a sealed metal box to shield from possible external noise sources. The block diagram has been shown in Fig. 3. The RF input comes from MARISAT-1 satellite at a frequency of

3945.5 MHz that has been demultiplexed by the demultiplexer. After feeding through the RF preamplifier and the filter, it is then mixed with the 3850 MHz signal at 7 dbm power level which is phase locked to the 116 2/3 MHz reference input. The 116 2/3 MHz reference input is applied and multiplied by a factor of 33 to 3850 MHz. The difference frequency 95.5 MHz is obtained from the output of the double-balanced mixer. The 95.5 MHz IF output goes to the RF input of the backend through the cable.

Note that the frontend box is located under the antenna. As we know, the typical temperature on the equator in the summer is very high. So it is necessary to test the reliability of the frontend of the C-band receiver under a high-temperature environment that the frontend box will eventually be exposed to. The testing was done using a heat blower and it had shown very dependable performance up to a temperature of 50°C.

2.4 3850 MHz phase locked oscillator

The reference oscillator manufactured by Frequency-West is shown in Fig. 6.

The reference input frequency is 116.666 MHz. After being multiplied by 33, it becomes 3850 MHz. The input of this phase locked oscillator comes from TP7 shown in Fig. 3. At TP7 the power level is 4 dbm. Because it is transmitted via a long cable, the power level will be attenuated to approximately 1 dbm when it reaches the oscillator. The power supply voltage of this oscillator is $-20V \pm 1.5\%$, so a -20V power supply will be needed. This oscillator will output

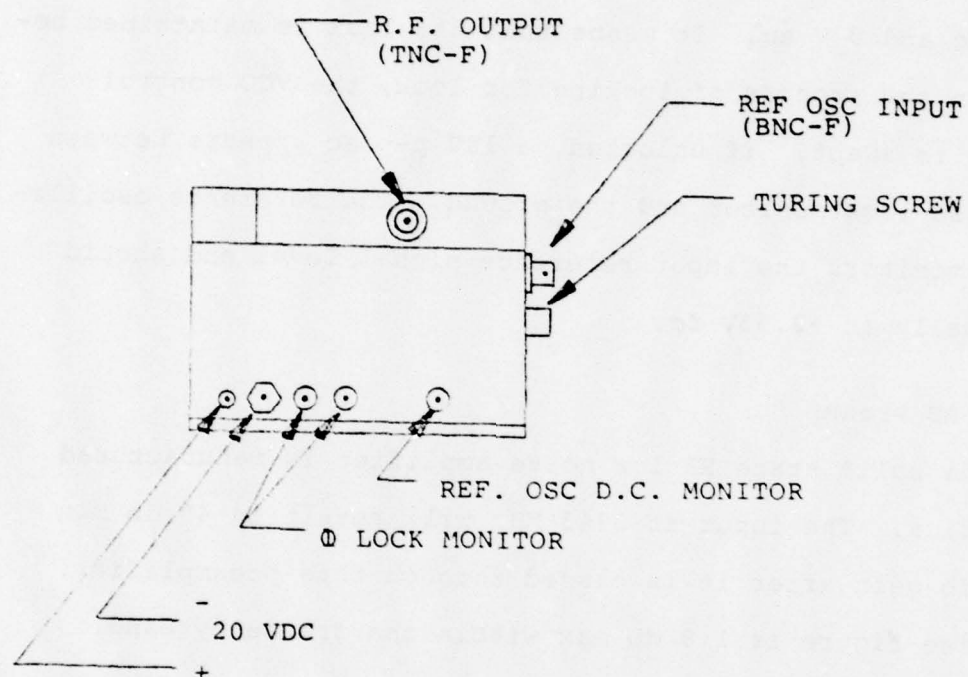


Figure 6. 3850MHz phase-locked oscillator

10 dbm R.F. power. It's buffered by a 3 db attenuator before feeding it to the mixer.

On the unit there are two pins connected together which constantly monitors the oscillator to see if it is in phase lock with the reference. If this is the case, the voltage between the phase lock monitor and the ground should be about -7.6V dc and 0 V ac. It means that the lock is maintained because in the process of looking for lock, the VCO control voltage is swept. If unlocked, a 18V p-p ac appears between the phase lock monitor and the ground. The reference oscillator dc monitors the input reference signal level and should be normally at +2.53V dc.

2.5 RF Preamp

The solid state RF low noise amplifier is manufactured by Amplica. The input at 3945 MHz will result in 45 db min \pm 0.3 db gain after it is passed through this preamplifier. The noise figure is 1.8 db max within the frequency band. The RF preamplifier is the only amplifier that amplifies the signal received from the antenna by the frontend of the C-band receiver. The input and output both have 50 ohm impedance with VSWR 1.5 max.

2.6 Bandpass filter

The purpose of the bandpass filter manufactured by CIRQTEL is to suppress the 3754.5 MHz image band. There are two possible bands of frequencies of RF signals which can be mixed with the 3850 MHz LO to produce a 95.5 MHz IF:

One is 3945.5 MHz, the other 3754.5 MHz. Since only the 3945.5 MHz input is desired, the 3754.5 MHz signal band in reality adds noise to the system. Since the signal to noise ratio is only 7 db for the input signal band to the RF preamp, noise from the image band will reduce that further to only 4 db which is definitely not adequate. Therefore a bandpass filter must be used to filter out this image band. The specifications for the filter are -2.5 db maximum at 3945.5 MHz and -40 db minimum at 3745.5 MHz. Thus, it is able to suppress the image noise source (3754.5 MHz). Its amplitude response curve is shown in Fig. 7. The bandwidth (the frequency width between two 3 db points) is 130 MHz. The output and input impedances are both 50 ohms and the connectors is of N-type M/F connectors.

2.7 Mixer M2040

The double balanced mixer M2040 manufactured by Western Microwave has a frequency specification range of 2-4 GHz, IF bandwidth D.C.-1.2 GHz and LO power input of +7 dbm. It is a balanced mixer which down converts the signal coming from the RF preamp (3945.5 MHz) with the signal of phase-locked local oscillator (3850 MHz) to an IF frequency of 95.5 MHz. The conversion loss at 3945.5 MHz is 6.2 db. Since the power of the RF input at R shown in Fig. 3 is -86.9 dbm, the IF output will be -93.1 dbm.

Attenuation,db

18

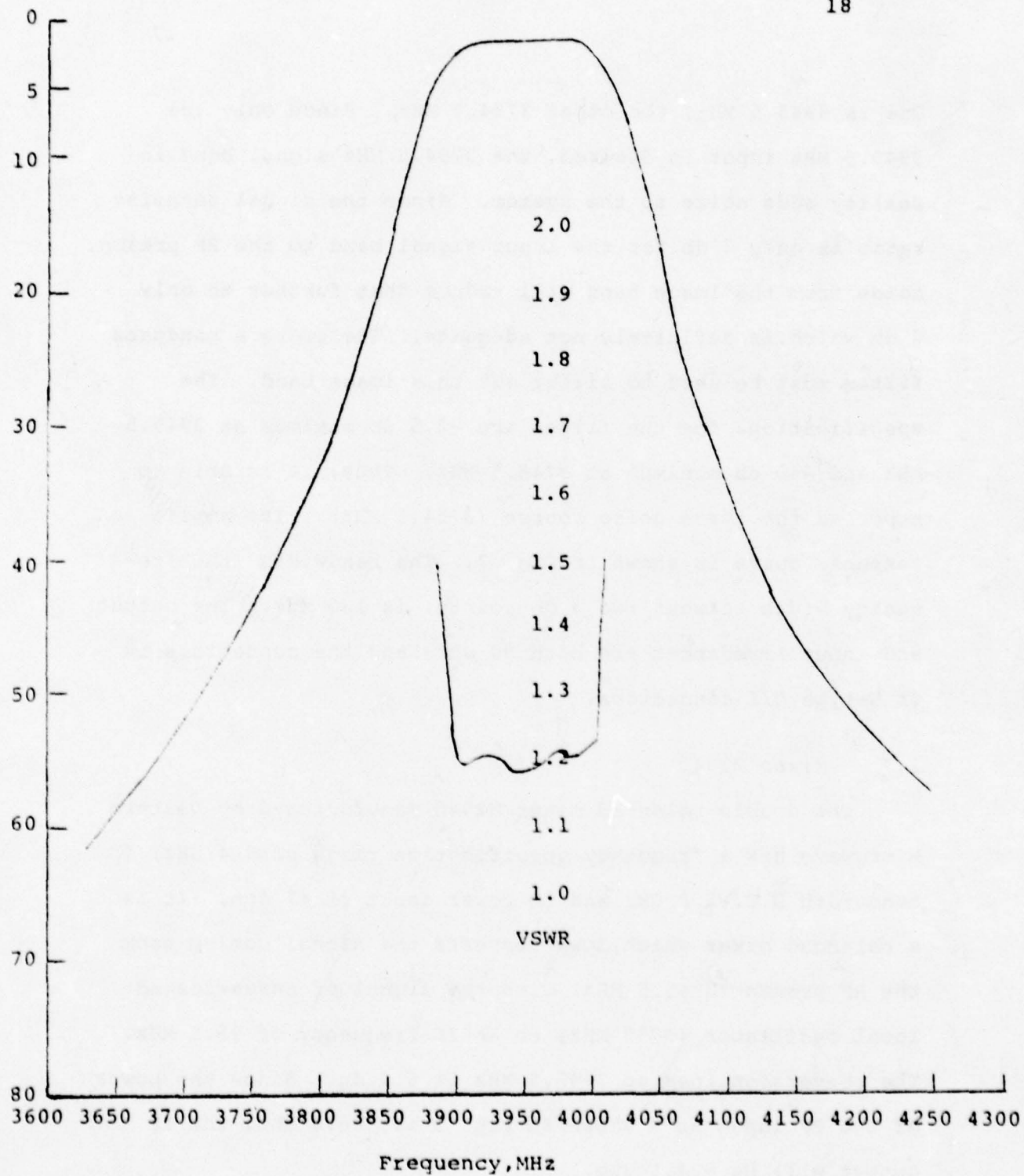


Figure 7. The amplitude response curve of the 3945.5 MHz bandpass filter

3. A Detailed Description of the Backend

The block diagram of the backend of the C-band receiver is shown in Fig. 3. The input to the back-end comes from mixer M2040 which mixes the antenna signal (3945.5 MHz) and 3850 MHz reference. So the frequency of the input signal is 95.5 MHz. Amplified by the 1st IF amplifier, the input signal mixes with the 116 $2/3$ MHz reference and produces a 21.1667 MHz mixed signal. Through the driver and the 31 db attenuator, the output goes to Model B receiver.

Most components of back-end are on the chassis except that the DC power supplier is beneath the chassis and the 31 db attenuator is mounted on the panel. Some switches, current meter, BNC connectors, fuses and LED warning light are also on the panel. In Brazil, the backend of the C-band receiver will be set into an air-conditioned room, so it is not necessary to worry about the operating temperature like the frontend.

We will describe the back-end in detail in the following.

3.1 10 MHz Crystal Oscillator

The HP Model 10544A 10 MHz crystal oscillator is extremely stable. The stability ($\Delta f/f$) is 10^{-11} in one second average. Its aging rate is better than 5×10^{-10} /day. This rate can be expected to gradually decrease and typically will reach 1.0×10^{-10} within one year. The coarse tuning permits periodic adjustment back to 10 MHz. The adjustment range is adequate to cover in excess of 10 years at the typical aging rate. The unit is designed to operate into a 1000 ohm load. After power on, it

will take 24 hours to stabilize the output frequency. The temperature of the oscillator oven is maintained by varying the duty-cycle of the oven input current through a control transistor. The output signal at pin 11 on the unit indicates the temperature condition of the oscillator oven. The signal voltage level depends on the value of oven supply voltage at pin 14 and 15. The schematic of the 10 MHz crystal oscillator is shown in Fig. 8. Duty cycle of the signal at pin 11 depends on the oven temperature; long duty cycle at turn on and short duty cycle at operating temperature. The corresponding dc voltage monitored with a high impedance voltmeter is maximum when oven is cold (at turn-on) and minimum when oven is at operating temperature.

3.2 50 MHz PLL (Phase locked loop)

The schematic of the 50 MHz PLL circuit is shown in Fig. 9. At first, we will illustrate the theory of phase-locked loop simply and will then go into 50 MHz PLL circuit analysis.

Block Diagram of a Phase-Locked Loop is shown in Fig. 10. If an input signal is applied to the system, the phase comparator compares the phase of the input signal with the VCO phase and generates an error voltage, $V_e(t)$, that is related to the phase difference between the two signals. This error voltage is then filtered and applied to the control terminal of the VCO. If the input frequency, f_s , is sufficiently close to f_0 , that is within the capture range, the feedback nature of the PLL causes the VCO to synchronize or to lock

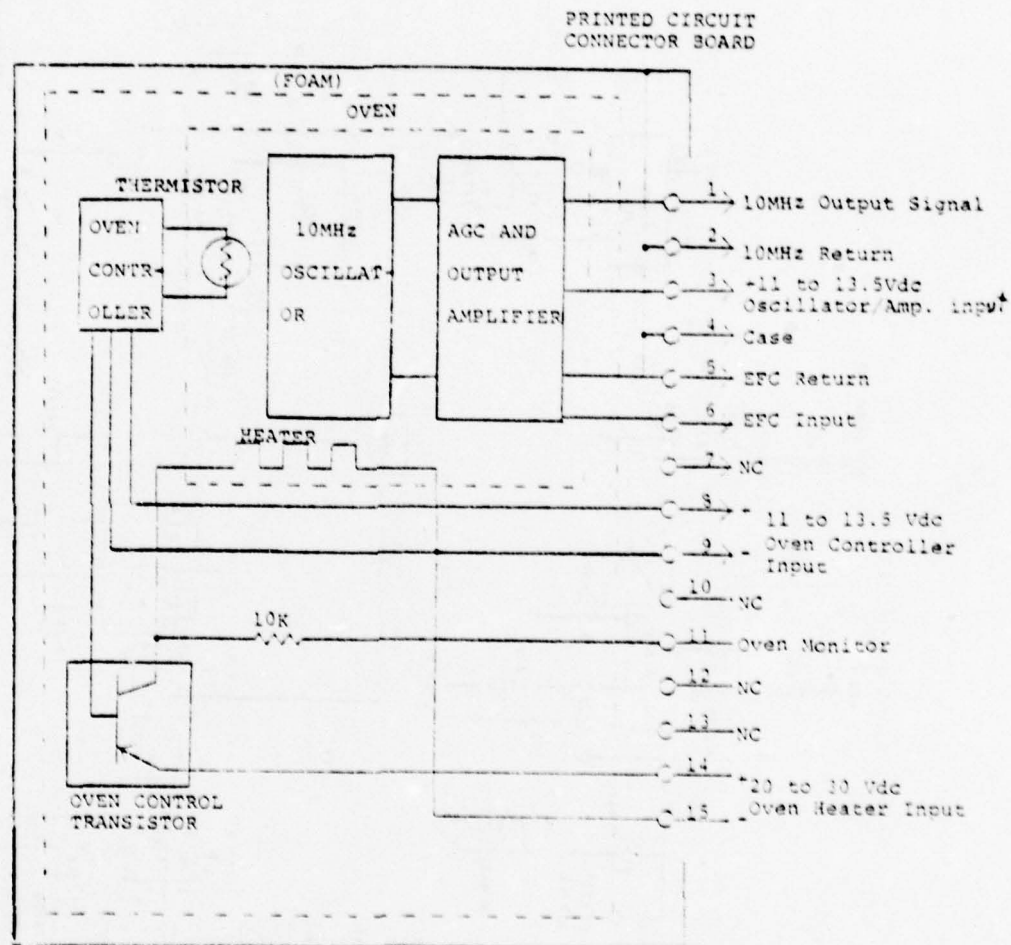


Figure 8. Block diagram of 10 MHz crystal oscillator.

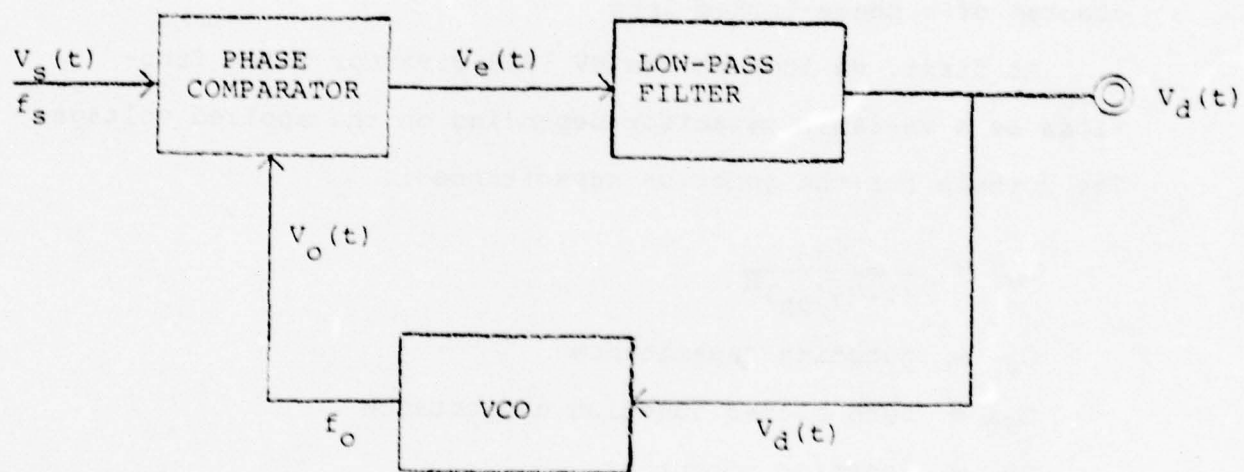


Figure 10. Block diagram of a phase-locked loop

onto the incoming signal. Once in lock, the VCO frequency is identical to the input signal, except for a constant phase difference.

In the following the 50 MHz PLL circuit will be analyzed part by part.

Oscillator:

The schematic of oscillator circuit is shown in Fig. 11. It works as a voltage-controlled oscillator (VCO) in block diagram of a phase-locked loop.

At first, we look at the MV 1628 varactor which functions as a variable capacitor depending on the applied voltage. The formula for the junction capacitance is

$$C_J = \frac{C_{JO}}{(1 - V_J/PB)^M}$$

C_J = junction capacitance

C_{JO} = zero biased junction capacitance

PB = junction potential

M = grading coefficient

V_J = junction voltage (positive for the forward bias
and negative for reverse bias)

Because the MV 1628 varactor is always reverse -biased, V_J is negative. When V_J decreases (more negative) C_J will decrease and oscillating frequency f_0 increases. Inversely if V_J increases then C_J increases and f_0 decreases. The loop reactance decides the oscillating frequency.

The VCO control signal $V_d(t)$ coming from phase comparator MC 4044 changes the reverse voltage of the MV 1628 varactor.

This is just a negative feed-back system to make f_0 locked to the 10 MHz crystal oscillator. From the data of the measurement, $V_d(t)$ ranges from 2.30V to 2.80V.

To trim the oscillator frequency f_0 to be exactly 50 MHz, we can adjust the series variable capacitor ranging from 5.5 pF to 13 pF.

50 MHz amplifier:

As shown in Fig. 12, the transistor 2N5179 is used to amplify the 50 MHz oscillator signal. Now the analog signal will be converted to TTL level by an RC circuit and TTL inverters (74S04). The drain current I_{OL} multiplied by $2k$ elevates the DC signal level by $I_{OL} \times 2k$. The reason to do this is to make possible the digital gate to respond to a weak input signal. Using two TTL inverters in tandem sharpens the waveform of the output TTL signal. In Fig. 13, the analog input and the square wave output are shown.

Comparator:

The schematic of comparator is shown in Fig. 14. The chip MC 4044 compares the phase of the 2.5 MHz reference and 2.5 MHz signal. The 2.5 MHz reference comes from HP 10 MHz crystal oscillator with less than 10^{-11} deviation. The 10 MHz frequency of the reference is divided by 4 in the chip SN 7473 and results in a 2.5 MHz reference. The 2.5 MHz signal is obtained by dividing the 50 MHz oscillator signal through the divider scaling 20 that is composed of SN 74196 and 7473. When phase comparator MC 4044 detects the phase difference (frequency difference) between the 2.5 MHz reference

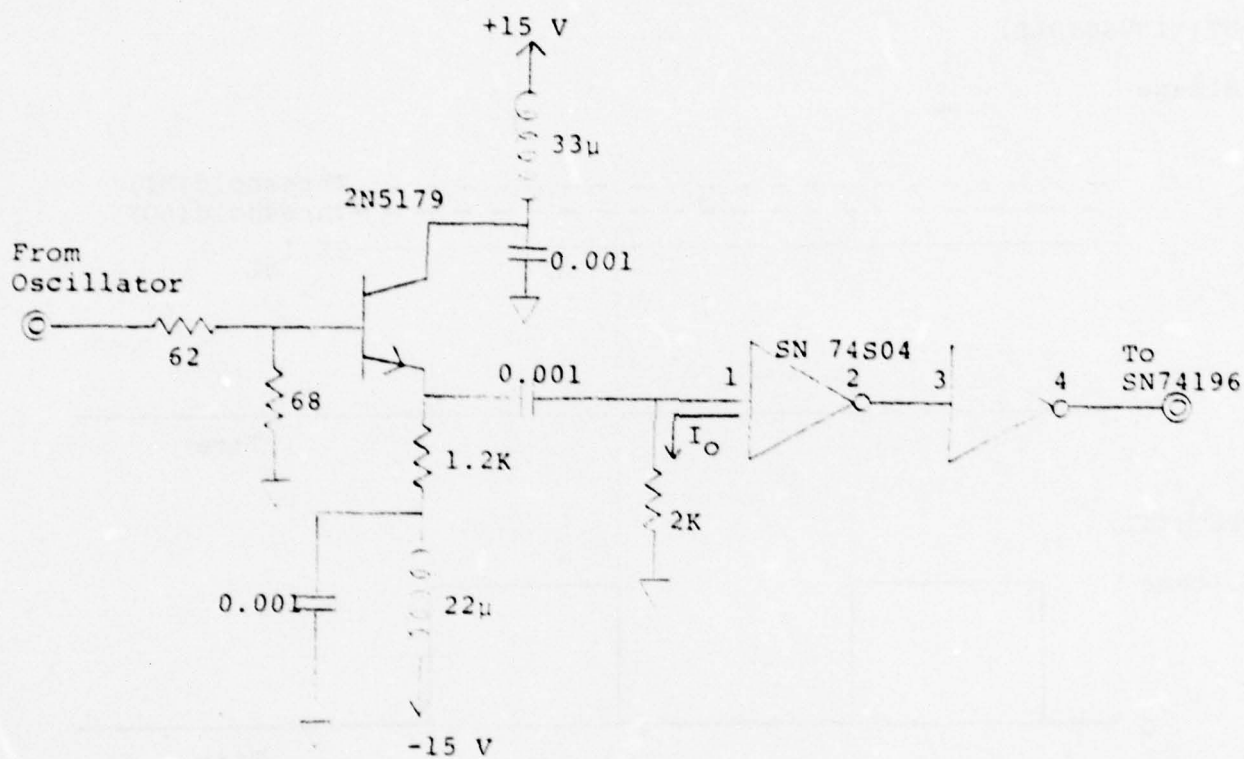


Figure 12. Schematic of 50 MHz amplifier.

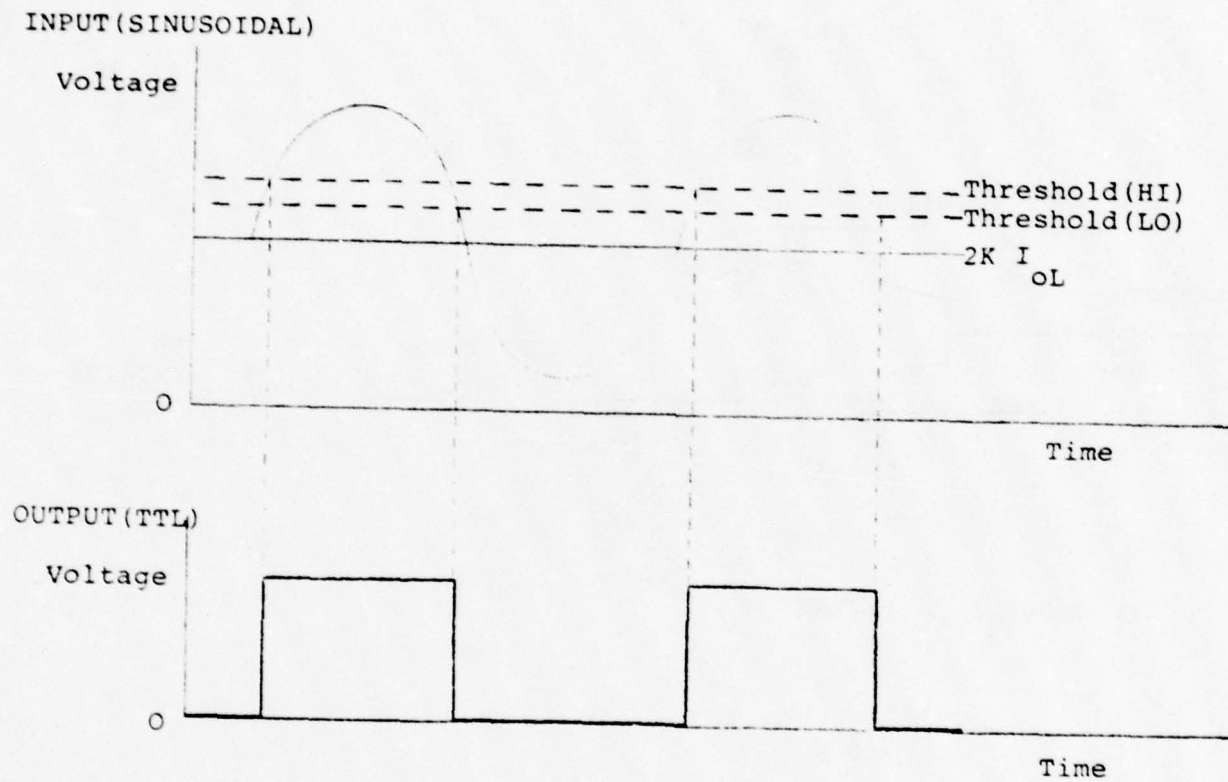


Figure 13. Analog signal is converted to TTL level

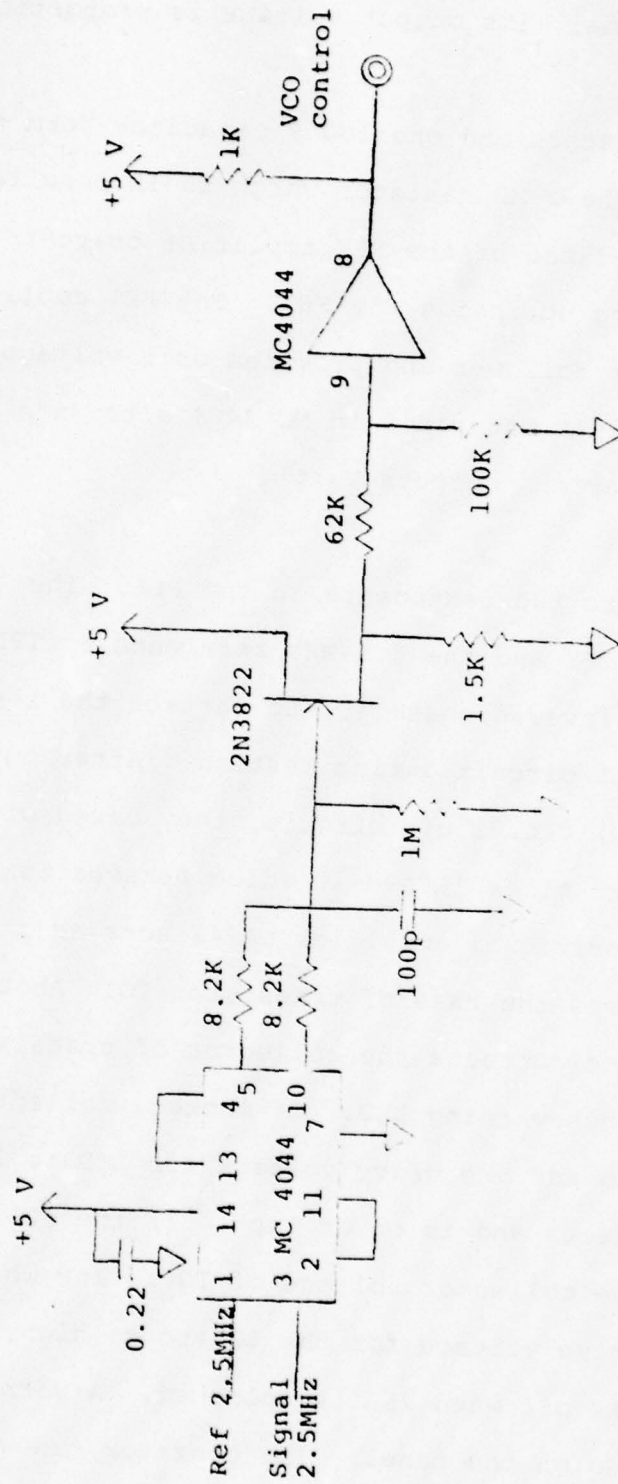


Figure 14. Schematic of comparator

and the 2.5 MHz signal, its output voltage is proportional to the difference.

Two 8.2 K resistors and one 100 P capacitor form the low-pass filter. The 1 M Ω resistor which is in parallel with the input impedance of the FET amplifier prevents the charge from building up inside the FET. The FET amplifier works as an emitter follower and provides unit voltage gain. The part between pin 8 and pin 9 in MC 4404 acts as a current-to-voltage converter and outputs $V_d(t)$.

Phase lock monitor:

TPR and TPS are two testpoints in the PLL. The 2.5 MHz signal appears at TPS and the 2.5 MHz reference at TPR. They are both taken in inverse phase (\bar{Q}) to isolate the test probes from the PLL circuit during testing. After buffered by a series R(470 Ω) C(0.01 uf) circuit, they mixed with each other in a balanced mixer (RFA-M-1) which behaves as a phase detector. The operational amplifier $\mu A741$ acts as a Schmitt trigger which drives the base of transistor TO. Another inverter in cascade connects the collector of transistor TO for driving the lock warning LED. If locked, collector voltage of TO is high and the drive voltage for LED is low. So the LED link conducts and is on at lock. If the PLL is unlocked, then the collector voltage of TO is low which in turn makes the drive voltage for the LED to go high. As a result, the LED is off when PLL is unlocked. A warning LED light is installed on the panel. The operator can watch the

warning light to determine whether the PLL is locked or not.

The PLL circuit board that is mounted on the chassis of the C-band receiver is of the kind of VECTOR D.I.P. Plugboard. There are three power supplies needed, $\pm 15V$ and $+5V$. Because the operating frequency is very high on the board. We need $0.001\mu f$ and $10\mu f$ capacitors to bypass the power supplies to ground to improve circuit stability.

3.3 Frequency doubler and driver

The schematic is shown in Fig. 15. The input comes from 50 MHz phase-locked loop circuit at 3-dbm power level. Look at the circuit schematic, 50 MHz signal is coupled in by a transistor. Two HP2810 diodes generates the harmonics of 50 MHz such as 100 MHz, 150 MHz, 200 MHz . . . in ascending order because the current-voltage curve is nonlinear for the diode. When input is at positive cycle, D1 cuts down and D2 conducts. Inversely, input at negative cycle, D1 conducts and D2 cuts down. So we can get full-wave harmonics. Amplifier $\mu A703$ and its interfaces constitute an active filter centered at frequency 100 MHz, which filters out higher order harmonics. The driver is an amplifier and composed of biased resistors, transistor and collector-coupling transformer. The output at 100 MHz has been adjusted to +10 dbm level by controlling the input of the driver. The 10 dbm output goes to a power divider to be separated into two equal parts, each part at +7 dbm power level.

3.4 Frequency divider by six

The schematic is shown in Fig. 16. The input comes from frequency doubler and driver 1 (see Fig. 3). After divided by power divider, the 100 MHz signal goes to the divider-by-six and driver 2. The other output of the power divider goes directly to the L-end of the mixer. For the schematic shown, 2 self-biased inverters (74S04) are used to supply TTL level. Two J-k flip-flop (2N74S112) are wired to function as a frequency divider by 3. Another J-k flip-flop of 74H73 follows as a frequency divider by 2. So the frequency at the output of this frequency divider is $16 \frac{2}{3}$ MHz now. The L-C in series ($L=1\mu H$ $C=100pF$) maximizes the 16 MHz component. Because the input signal of the mixer should be much smaller than the LO to prevent intermodulation from occurring, an attenuator is needed at the $16 \frac{2}{3}$ MHz output. Using one computer program, a π -type attenuator of -24 db pad is designed as $R_S=390\Omega$ and $R_P=56\Omega$. The $16 \frac{2}{3}$ MHz output goes to the mixer. After being mixed, the sum and difference of two input frequencies will be generated. Bandpass filter is used to eliminate the unwanted image band. This is discussed in the next section.

3.5 $116 \frac{2}{3}$ MHz bandpass filter

The double balanced mixer mixes the 100 MHz signal with the $16 \frac{2}{3}$ MHz signal. After mixing there would be two sidebands. One is $116 \frac{2}{3}$ MHz, another $83 \frac{1}{3}$ MHz. Since only the $116 \frac{2}{3}$ MHz signal is desired, the $83 \frac{1}{3}$ MHz signal in

reality adds noise to the system and reduces the signal-to-noise ratio. Therefore, a bandpass filter must be used to filter out this image band. The amplitude response of this filter manufactured by CIRQTEL is shown in Fig. 17.

Its central frequency is $f_0=117$ MHz with a bandwidth (frequency width between two 3 db point) of 16 MHz. Connector is of BNC M/F type.

3.6 Amplifiers

There are three amplifiers used in the backend of the C-band receiver. Because the frequencies used are in the UHF range, each amplifier is contained in an aluminium box in order to minimize radiation interference.

The first one is an RF amplifier (Aydin Vector MHD-175). MHD 175 modular amplifier consists of multiple stages of amplification on a single aluminium thick film substrate. The entire assembly is mounted in a hermetically sealed 4 pin dual-in-line package. It functions as an amplifier to get +10 dbm output at $116 \frac{2}{3}$ MHz frequency. The input comes from $116 \frac{2}{3}$ MHz bandpass filter. The output goes to power divider to supply the reference-in of the frontend of the C-band receiver and the mixer HP 10514A. The gain in frequency range 1-250 MHz is 33 ± 1 db and noise figure 5.0 db max. The supply voltage is 15V and the rated current is 75 mA.

The second one is an IF amplifier (Aydin Vector GA-2). The GA-2 modular amplifier consists of a single stage

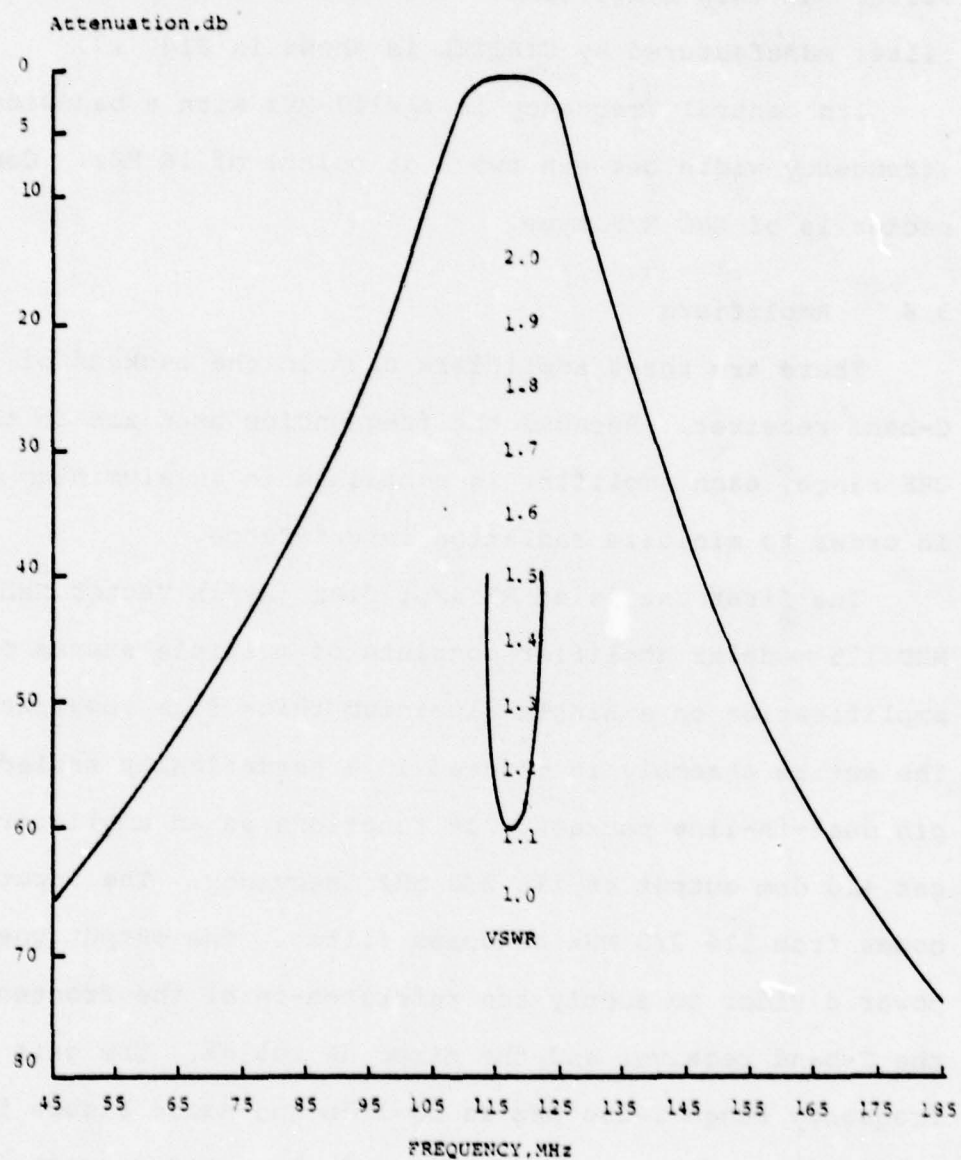


Figure 17. Amplitude response curve of 116 2/3 MHz bandpass filter.

amplification on an aluminium thick film substrate. The entire assembly is mounted in a hermetically sealed 4 pin TO-12 package. Its input is connected to the RF output of the frontend of C-band receiver and output to the R end of the mixer HP 10514A. The gain is 12 db in frequency range 5-400 MHz. Some other specifications are 5.5 db N.F. and +15V DC at 25mA supply source. The frequency used in this amplifier is 95.5 MHz.

The third amplifier used is a wideband transistor HF driver. The circuit is shown in Fig. 18. It inputs from I-end of the mixer HP 10514A and outputs enough signal to model B receiver through the 31 db step attenuator. The gain of this amplifier is 46 db. Some other specifications are 2.8 db NF and 15 VDC supply voltage at 30mA.

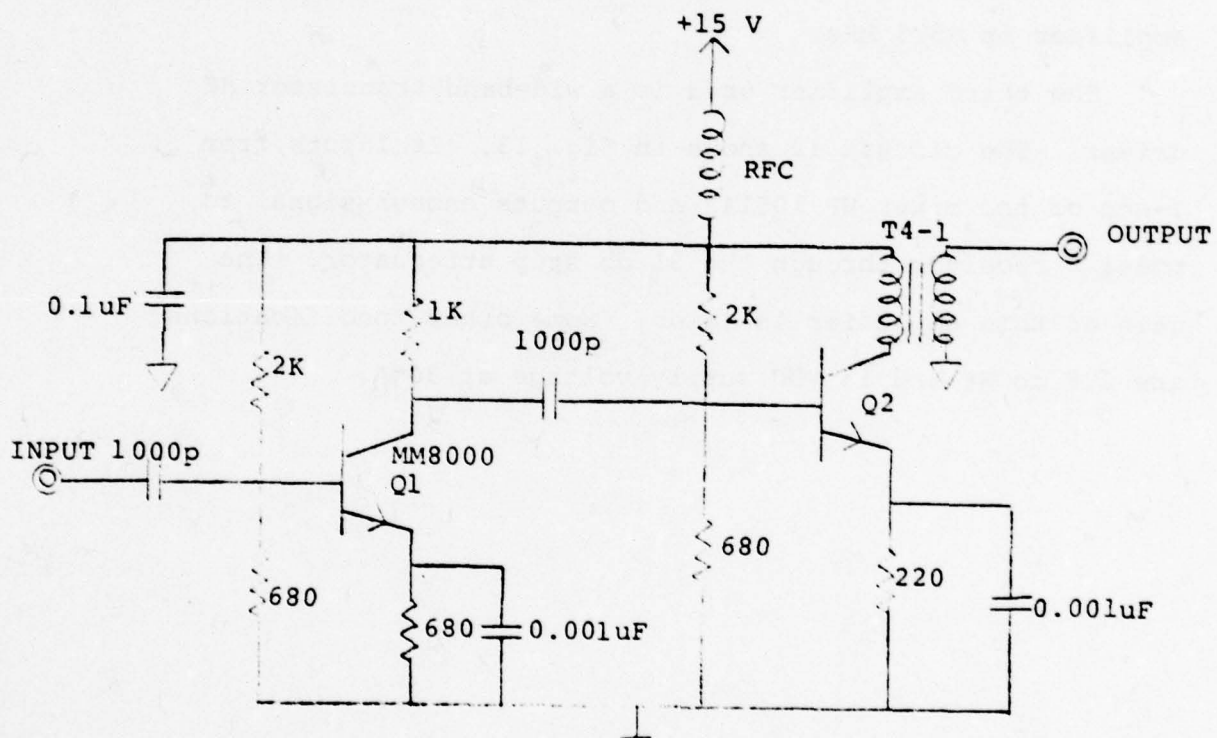


Figure 18. Schematic of model B driver.

4. Receiver Performance

4.1 The linearity test of C-band & Model B receiver

To test the linearity of the C-band and Model B receivers, we feed a 95.5 MHz signal to the input of the C-band backend and measure the output AGC voltage of the model B receiver. The power range of the input is from -60 dbm to -125 dbm. There are two plug-ins available for the model B receiver. It shows some minor differences between them and one of the differences is that the required input range is not the same. By switching in or out 31 db step attenuators, we can get the desired input power to the model B receiver. The AGC output voltage of the model B receiver should range from 0.2V to 0.8V to fit the requirement of the multi-channel digital data logging system. We would like to enlarge the AGC voltage range in the test and look at how they vary with the input power level. The noise level of the model B AGC is found to be -0.13V in the absence of any input.

To carry out this linearity test, the following several steps are taken.

- (1) Set up the model B receiver and backend of the C-band receiver. The input of the backend of the C-band receiver comes from the signal generator. Adjust this HP signal generator to get 0 dbm output power at first. Then turn the knob to set the output power level needed. We start it from the -125 dbm and raise it in 5 dbm steps. Turn the frequency control to the desired frequency. Then adjust fine-tuning frequency control to find the exact

frequency following the procedures described in step 3.

- (2) Connect the output of the backend of the C-band receiver to the BNC connector on the front panel of the plug-in unit of model B receiver. This input is matched at 50 ohms. Plug the input of the earphone to the jack marked "PHONES" on the front panel of the model B receiver. In order to measure the AGC output voltage, we connect a digital voltage meter with the AGC output on the panel of model B receiver. Then apply the voltages to model B receiver (C-band receiver has been energized). Note that the required dc voltages to model B receiver are -12.4V and +8.4V and reversed voltage polarities will cause permanent damage to the receiver.
- (3) In order to establish the tone output, the "BFO" must be turned on. The BFO switch applies power to the BFO. The audio gain control is ganged to a SPST switch. When the audio gain control is rotated clockwise, the audio amplifier is turned on and the signal may be heard through earphone. The BFO PITCH control varies the frequency of the BFO and changes the pitch of the beat note. The PITCH control is set so that a "zero beat" or zero frequency beat note will occur when the AGC output voltage is at its peak while trimming the input frequency. After this adjustment, don't touch the PITCH knob again. The PITCH control is now fixed. Because the signal generator has some frequency drift, when you

change the input power level each time, adjust the fine frequency-tuning control back and forth to get back to the exact frequency by searching for a zero beat. Look at the voltage shown on the digital voltage meter and record it.

- (4) Repeat steps (1) and (3) for each input power level from -125 to -60 dbm in 5 dbm steps. Draw the volt/power curve relating the AGC voltage with input power. In the midband of the curve, it's found to be linear. For the two plug-ins for the model B receiver, the data are listed below and the AGC output vs. 95.5 MHz input power in dbm curves are shown in Fig. 19 and Fig. 20. It should be mentioned these measurements were made with the 31 db attenuation shown in Fig. 3 all in.

Table 2. Linearity Test of the Backend of the C Band Receiver

Input of the Backend (dbm)	Model B AGC Output (V)	
	#1	#2
-125	-0.206	-0.14
-120	-0.279	-0.185
-115	-0.391	-0.264
-110	-0.496	-0.369
-105	-0.615	-0.501
-100	-0.733	-0.639
-95	-0.865	-0.770
-90	-0.984	-0.904
-85	-1.078	-1.020
-80	-1.134	-1.098
-75	-1.154	
-70	-1.182	

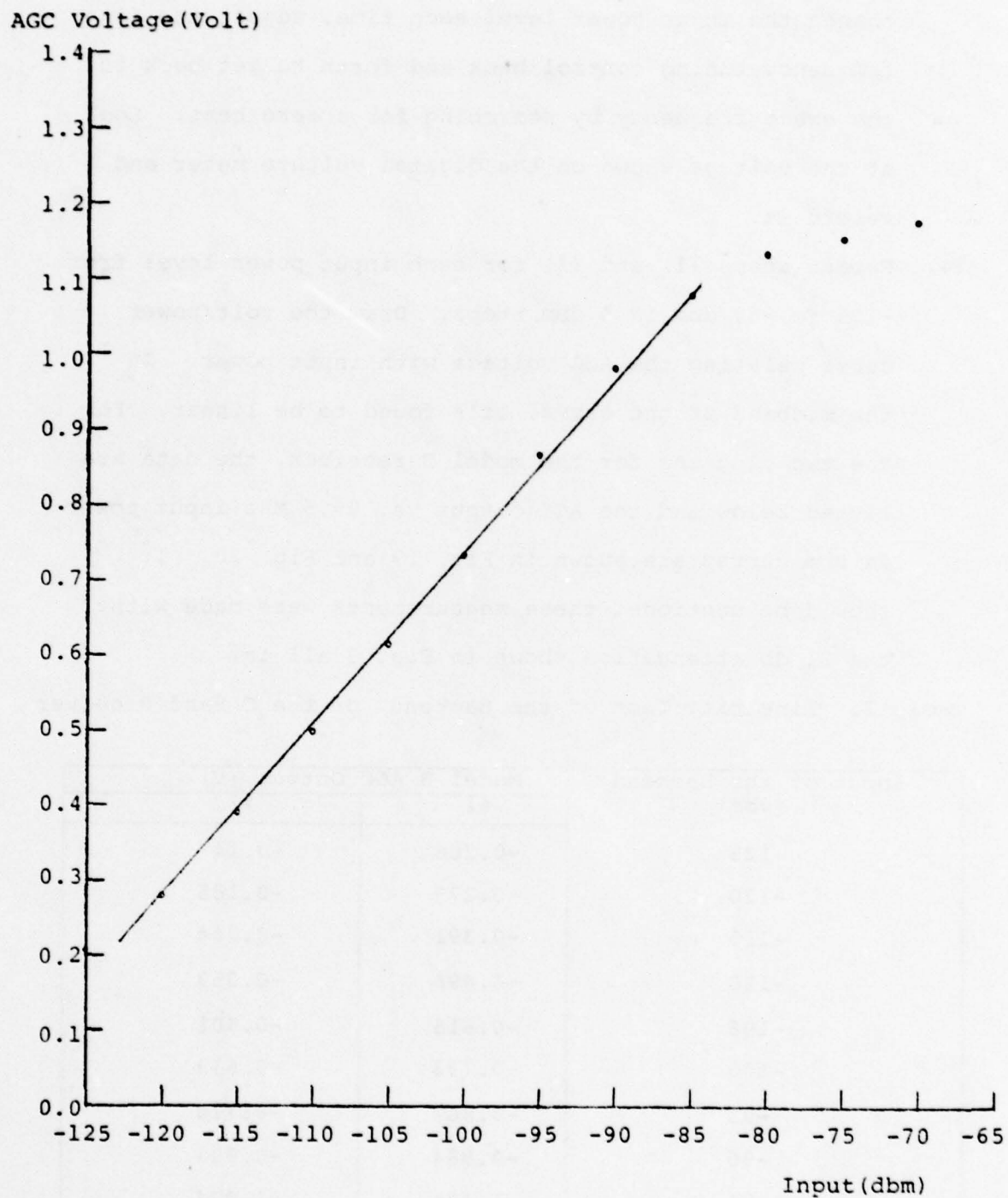


Figure 19. Linearity test for C-band (backend) and model B receiver (plug-in #1)

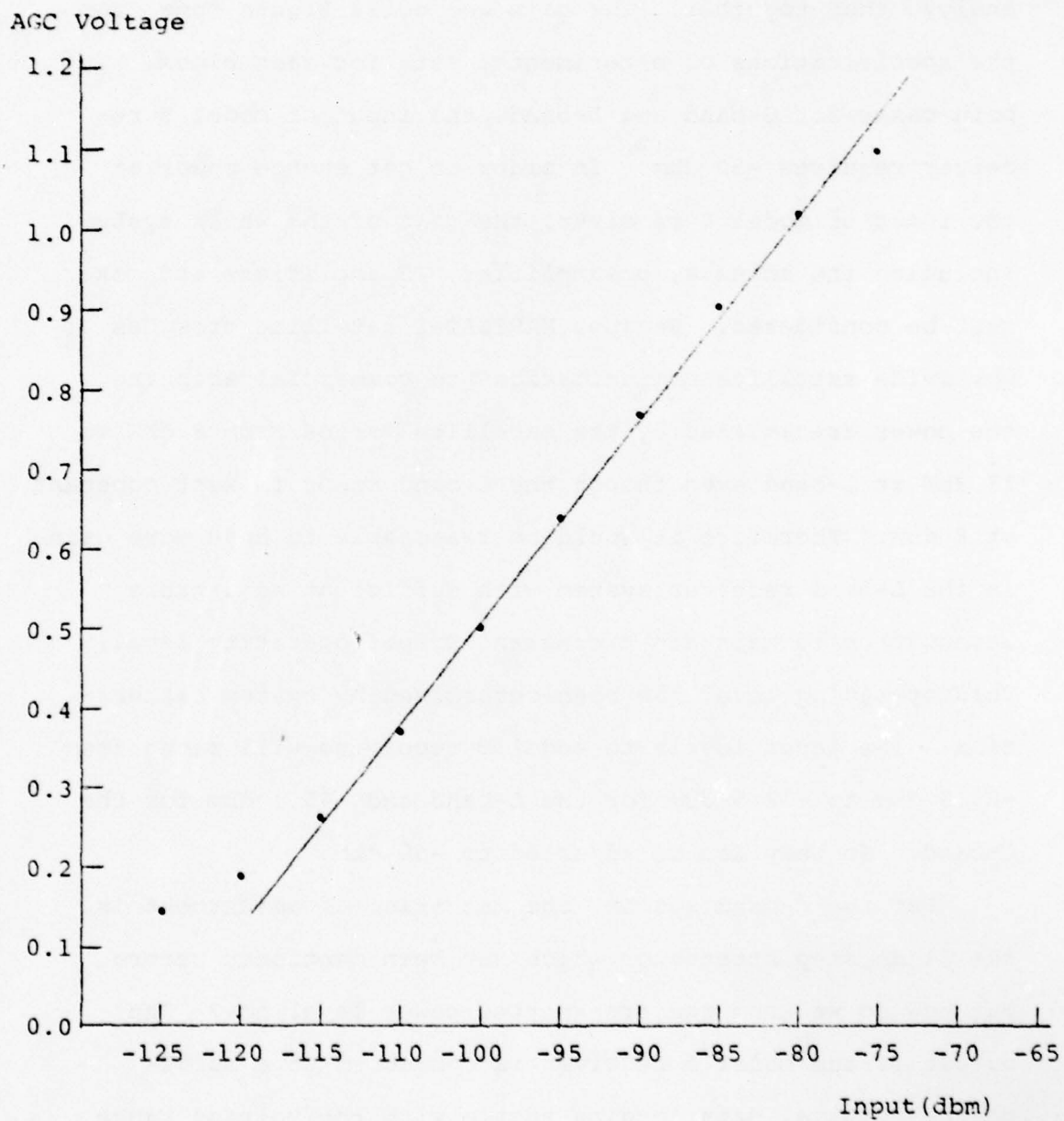


Figure 20. Linearity test for C-band (backend) and model B receiver (plug-in #2)

4.2 Gain and signal-to-noise ratio in the C-band and L-band systems

Since the antenna, the parabolic reflector and the demultiplexer are used for both C-band and L-band systems, we analyze them together. The gain and noise figure come from the specifications or experimental data for each block. In both cases for C-band and L-band, the input of model B receiver requires -50 dbm. In order to get enough power at the input of model B receiver, the gain of the whole system including the antenna, preamplifier, IF amplifiers and mixer must be considered. Because MARISAT-I satellite provides worldwide satellite communications to commercial shipping, the power transmitted by the satellite varies from 8 dbW to 17 dbW at L-band even though the C-band power is kept constant at 8 dbW. Therefore it would be reasonable to have more gain in the L-band receiver system with sufficient adjustable attenuation to maintain a constant proper operating level. This operating level has been determined by system calibration. The input levels to model B receivers will range from -23.5 dbm to -32.5 dbm for the L-band and -45.1 dbm for the C-band. So they can be adjusted to -50 dbm.

For the C-band system, the mechanism of adjustment is the 31 db step attenuator which has been mentioned before. But how do we know the transmitted power level now? The output of the model B receiver is connected to a multi-channel digital data logging system with the voltage range from 0.2V to 0.8V. By connecting the output of model B receiver (AGC voltage) in parallel with the current meter

installed on the panel of the backend of C-band receiver, the operator is then able to detect any deviations from the proper 0.2-0.8V operating range. If such deviation occurs, the operator is instructed to switch in or out the 31 db step attenuator to obtain the desired operating point.

Another point for us to consider is the signal-to-noise ratio of the system. The image sideband as a source of noise has been eliminated by a bandpass filter. Now, we must also consider sky noise, cable noise and preamplifier noise and compute the total noise power present at the input of the preamplifier. This is done separately for L-band and C-band in the following.

(1) L-band system

The noise figure of preamplifier is 2.5 db, which corresponds to a noise temperature of 256°k. The total noise temperature at input of preamplifier is equal to 606°k composed of sky noise 300°k, cable noise 50°k and preamplifier noise 256°k. We have the following formula concerned with the noise power.

$$P_N = kTB$$

where

P_N is the noise power, T the noise temperature, k the Boltzmanns constant and B the bandwidth of the receiving system. For a 4 kHz bandwidth the expected noise power at input of preamplifier is computed to be 3.345×10^{-17} watts or -164.7 dbW.

We will compute the signal and the signal-to-noise ratio at input of preamplifier in the following way:

effective power radiated at the satellite	8dbw to 17dbw
propagation attenuation	-188db
antenna gain	+ 24db
cable loss	- <u>0.5db</u>
Signal at input of preamp	-156.5dbw to -147.5dbw
Signal-to-noise ratio	8.2db to 17.2db

To calculate the power available to model B receiver, we proceed as below:

Effective satellite radiated power	+ 8dbw to +17dbw
propagation attenuation	-188db
antenna gain	+ 24db
cable loss	- 0.5db
pre-amp gain	+ 38db
1st mixer	- 10db
1st IF gain	+ 30db
2nd mixer	- 10db
2nd IF gain	+ <u>46db</u>
power available to model-B receiver	-62.5dbw to -53.5dbw

The power available to model B will range from -53.5dbw (or -23.5dbw) to -62.5dbw (or -32.5dbm) and Model B receiver needs -50dbm as its operating point. So it is more than adequate.

(2) C-band system

The preamplifier noise temperature is 149°K which is equivalent to a noise figure of 1.8db. The total noise temperature at input of preamplifier equals to 449°K composed of sky noise 250°K , cable noise 50°K and pre-amplifier noise 149°K . Using the formula in the previous section, we get the noise power at input of preamplifier 2.478×10^{-17} watts or -166 dbW.

In the following are computed the signal and the signal-to-noise ratio at the input of the preamplifier.

effective power radiated at the satellite	+8dbw
propagation attenuation	-196db
antenna gain	+ 29db
cable loss	- 0.9db
Signal at input of preamplifier	-159.9dbw
Signal-to-noise ratio	6.1db

The power available to the model B receiver is computed in the following way.

effective satellite radiated power	8dbw
propagation attenuation	-196db
antenna gain	29db
cable loss	- 0.9db
RF pre-amp gain	+ 45db
Filter attenuation	- 2db
1st Mixer loss	- 6.2db
1st IF gain	+ 12db
2nd mixer loss	- 10db
2nd IF gain	46db
power available to model B receiver	- 75.1dbw

At the input of the backend of C-band receiver, (i.e. immediately after the first mixer in Fig. 3) the expected power is -93.1 dbm at 95.5 MHz. Referring to Figs. 19 and 20, this power level is near the desirable linear operating point.

5. Conclusion

Equatorial ionosphere is known to possess one of the most intense ionospheric irregularities in nature. These irregularities can scatter radio waves and result in the scintillation phenomenon. For purpose of observing these scintillations we have established a cooperative program with Universidade Federal do Rio Grande do Norte, Natal, Brazil where the field station is located. Under this program the UHF, the C-band and the L-band receiver systems were designed, built, laboratory tested and finally set up as a part of an overall scintillation receiving station to carry out several types of experiments. Both the UHF and the L-band receivers have been established and worked according to design expectations. Currently, both receivers produce data. However, the C band receiver is encountering some difficulties in the field even though it was put under power and checked frequently for a duration of over three months in the laboratory.

According to the calculation for L-band receiver in this thesis, the expected signal-to-noise ratio is about 8.2 db-17.2 db depending on the signal traffic at the satellite. From analyzing the data recorded in the field station, we deduced the signal-to-noise ratio to be 11 db. It is within the range specified in our theoretical calculation.

For the C-band system, the expected signal-to-noise ratio is only about 6.1 db maximum and this may prove to be

too low for adequate measurements. The antenna used in the system is a 6-foot diameter paraboloid. If a larger paraboloid could be used, the signal-to-noise ratio will improve. For example, if we enlarge the dish using a 12-foot diameter paraboloid, the signal-to-noise ratio will be increased by 6 db. This points to the need for a larger antenna. With a larger collecting area, the signal-to-noise ratio for the L-band receiver will also improve.

Appendix 1

Test Points and Check of Phase Lock

Power level detector and test points

A power level detector is designed to measure the approximate output power level at various test points. The schematic of the detector is shown in Fig. 21.

To measure the power, connect point 1 to a dc current meter. Point 2 and point 3 represent a feed-through connection and are to be used within a 50 ohms transmission system.

For the 1N270 diode, the diode current and applied voltage can be approximated by a square law relation

$$I \propto V^2$$

The power P is proportional to V^2/R . Thus, the dc current measured between point 1 and the ground will be proportional to the power available on that test point. The set-up for the power level detector is shown in Fig. 22.

There are seven test points labeled TP1 through TP7 in the backend of the C-band receiver. Connect the power level detector to the test point with a 50 ohms termination at point 3. We use a Simpson meter to measure the dc current flowing through point 1 and the ground. To calibrate the power level detector, connect the test probe of the oscilloscope to the test point. We can measure the peak-to-peak voltage at the test point. Because the impedance of the BNC adapter is 50 ohm, the available power can be represented by the formula

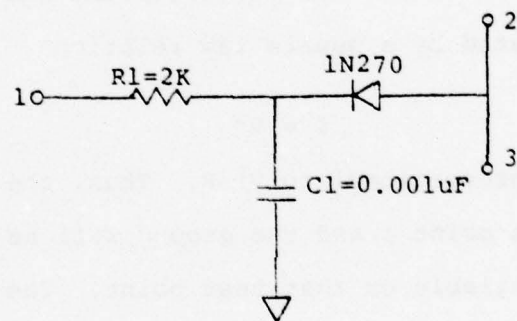


Figure 21. Power level detector.

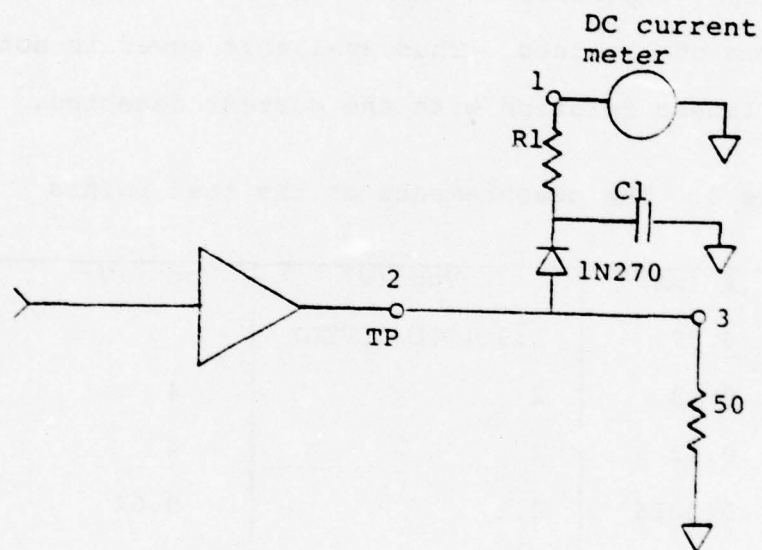


Figure 22. Setup of power level detector.

$$P = \frac{V_{rms}^2}{50}$$

Measurements have been made on the test points labeled TP1 through TP7. The data that resulted is shown in Table 3 below. Since at different TP's the frequencies are all different, we can not expect the uniform frequency response. Also, the output impedance at these points are slightly different from one another. Thus available power is not strictly in linear relation with the current detected.

Table 3. The measurements on the test points

	I (mA)	Vpp (V)	Vpp ² (V ²)
TP1	0.37	1.5 (TTL LEVEL)	
TP2	0.13	2	4
TP3	0.12	2	4
TP4	0.0026	0.2	0.04
TP5	0.18	2.6	6.76
TP6	0.11	1.8	3.24
TP7	0.05	1	1

After checking 10 MHz crystal oscillator and 50 MHz PLL, one may examine the testpoints one by one to ascertain that all components are working correctly. The currents measured by the power level detector on testpoints have been shown on Table 3.

50 MHz PLL

The 50 MHz PLL uses a LED monitoring light to indicate whether the 50 MHz PLL is in-lock at any moment. When it is locked in, the low potential produced by the output of the sensing circuit (which is the same as the base of T0) causes the collector of T0 to go high. The inverter will then present a low potential to the cathode of LED, forcing it to conduct. Thus the monitoring light will be on when the PLL circuit is in-lock. It goes off immediately upon the unlocking of the PLL circuit.

TPR on the PLL circuit board indicates the 2.5 MHz reference input to the phase detector from the 10 MHz crystal reference oscillator. TPS on the PLL circuit board is the test point that indicates the 2.5 MHz signal derived from the VCO signal. When locked-in, waveforms at these TP's will be synchronized. There is a lock adjustment screw connected to a variable capacitor on the PLL circuit board. By turning the screw, the VCO frequency can be adjusted to within the capture range of the PLL, thus causing initial lock-up.

3850 MHz phase-locked oscillator

There is only one way to check whether the 3850 MHz phase-locked oscillator has been locked in. When in lock the voltage of the phase lock monitor to the ground should be approximately -7.6V dc and 0V ac. If unlocked, 18Vp-p will appear between the phase-lock monitor and the ground. The reference oscillator DC monitor indicates the level of the input reference signal (116 2/3 MHz) which is normally at 2.53V. To simulate actual operating condition in equatorial

environment, the frontend of the C-band receiver has been exposed to hot air flow from a 350W hair blower. After half hour of heating, the receiver had shown no signs of instability or deviations from its intended operations.

Appendix 2

31db Attenuator in 1db Steps

The 31db attenuator is constructed by cascading 5 resistive π -network attenuator. These networks are weighted in a binary fashion such that any attenuation between 0db and 31db can be selected by switches. Fig. 23 shows the schematic of the 31db attenuator. The components for the resistive π -network are specified completely by its characteristic impedance z_0 and its attenuation G . It has the configuration shown in Fig. 24. For each π -section we demand the voltages and currents to satisfy

$$V_{in} = I_{in} Z_{in}$$

$$V_o = I_o Z_o$$

If $Z_o = Z_{in} = 50\Omega$ as the condition in C-band receiver, the resistors R_s and R_p must have values to satisfy

$$R_p^2 (1-G) - 100 G R_p - 2500 (1+G) = 0 \quad (1)$$

$$R_s = \frac{5000 R_p}{R_p^2 - 2500} \quad (2)$$

The computation for the values of these components can be easily carried out with a simple program in a programmable calculation such as the HP9825A.

The computed values of the resistor generally do not match those of the standard resistors. Therefore, small modifications of the values are required as long as the modified values will produce results within about 5%.

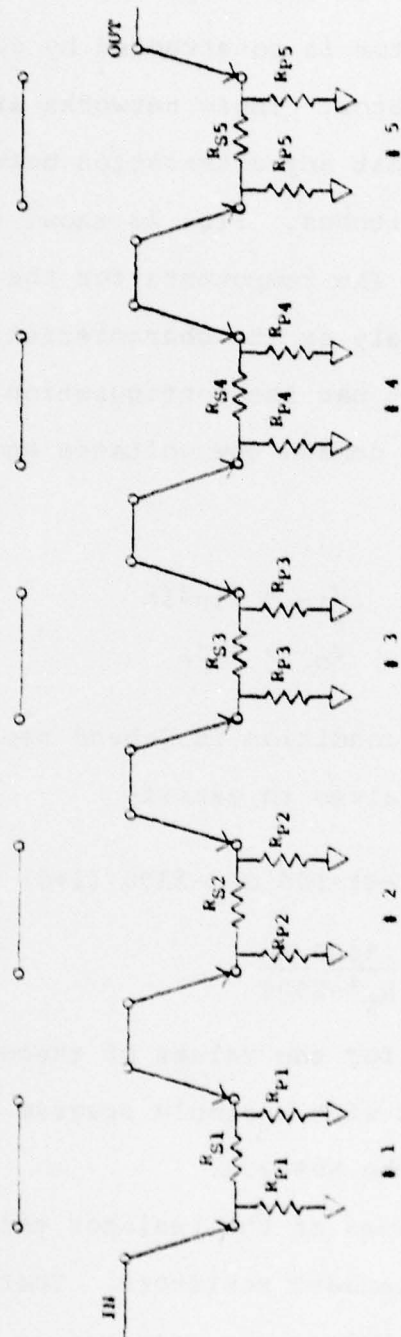


Figure 23. Schematic of the 31db attenuator in 1db steps.

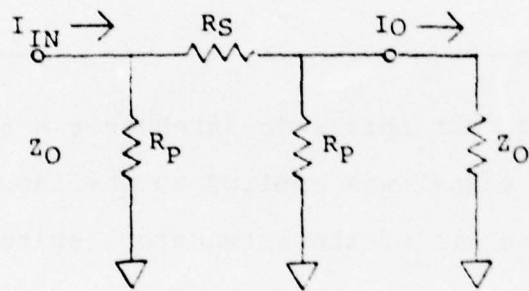


Figure 24. Configuration of the resistive π -network.

The five attenuators designed in this way are shown in Table 4.

Table 4. Design of 31db step attenuator.

	1db Attenuator	2db Attenuator	3db Attenuator	4db Attenuator	5db Attenuator
$R_s (\Omega)$	5.60	12	24	51	150
$R_p (\Omega)$	820	423	220	110	68
Input Z (Ω)	49.54	50.17	50.02	48.07	49.27
Attenua- tion (db)	0.98	2.06	4.02	7.90	15.86

In order to test this 31db attenuator a 60mV peak-to-peak sinusoidal signal was applied to the input of the 31db attenuator. With all of the attenuators switched in, we can measure the voltage at the output of each attenuator and get the following data.

Attenuators switched in	V_o (peak to peak)
1db	54 mV
1db & 2db	42 mV
1db, 2db & 4db	27 mV
1db, 2db, 4db & 8db	11 mV
1db, 2db, 4db, 8db & 16db	2 mV

Calculating the attenuation at the output of each attenuator, we get the results shown as follows.

$$1\text{db} = 20 \log \frac{60}{54} = 0.915$$

$$\text{error} = -0.085\text{db}$$

$$3\text{db} = 20 \log \frac{60}{42} = 3.098$$

$$\text{error} = +0.098\text{db}$$

$$7\text{db} = 20 \log \frac{60}{27} = 6.936$$

$$\text{error} = -0.064\text{db}$$

$$15\text{db} = 20 \log \frac{60}{11} = 14.735$$

$$\text{error} = -0.265\text{db}$$

$$31\text{db} = 20 \log \frac{60}{2} = 29.542$$

$$\text{error} = -1.458\text{db}$$

The results seem good enough to be satisfied.

References

- Engineering Staff, TTL Data Book for Design Engineers,
Texas Instruments Incorporated, 1973.
- Model B Receiver, Operation and Maintenance. The Magnavox
Company, Government and Industrial Division, Urbana, IL.
- Morris, R. L. and Miller, J. R., Designing with TTL Integrated
Circuits, McGraw-Hill Book Co., 1971.
- Umeki, R., Liu, C. H. and Yeh, K. C., (1977) Multifrequency
Studies of Ionospheric Scintillations, Radio Science,
12, 311-317.
- Yang, K. S. and Hearn, A. L., (1977), A multi-channel digital
data logging system for ionospheric scintillation
studies. Technical Report 61, Ionosphere Radio Labora-
tory, Department of Electrical Engineering, University
of Illinois at Urbana-Champaign.
- Yeh, K. C., Liu, C. H., and Youakim, M. Y., (1975), A
Theoretical Study of The Ionospheric Scintillation
Behavior Caused by Multiple Scattering, Radio Science,
10, 97-106.

Appendix H

A COMPUTER SCHEME FOR STUDYING SCINTILLATION
OBSERVATIONS AT NATAL

by

S. J. Meros

ACKNOWLEDGEMENT

The author would like to thank Dr. K. C. Yeh for the direction and helpful suggestions provided throughout the course of this work. My gratitude is also extended to senior research engineer K. S. Yang for his guidance in the digital hardware design portion of this project. Finally, I wish to thank Mrs. Linda Houston for the skillful typing of this manuscript.

This work was supported by the Army Research Office under grants DAAG 29-76-G-0286 and DAAG 29-78-G-0101.

TABLE OF CONTENTS

	Page
1. INTRODUCTION	1
2. HISTORY.	2
2.1 Experiment Design	2
2.2 Data Logging System	2
3. HARDWARE INTERFACE	5
4. DATA ANALYSIS.	17
4.1 Sampling Data	17
4.2 Error Correcting Schemes.	17
4.3 Autocorrelation	21
4.4 Cross Correlation	23
4.5 Fourier Transform	23
4.6 Power Spectrum.	26
4.7 S_4 Index.	28
5. RESULTS.	30
6. CONCLUSION	43
REFERENCES.	45
APPENDIX.	46

ABSTRACT

A data analysis scheme for studying the scintillation of transionospheric radio signals near the equator is discussed in this thesis. This thesis describes a digital system which takes the decoded scintillation data and uses a Hewlett-Packard 9825A desk calculator to selectively sample and store the data on a small tape cartridge. The H.P.9825A is then used to analyze the data. Data analysis consists of error correcting schemes as well as computation of data autocorrelation, crosscorrelation, power spectrum and S_4 index. Several pieces of data are chosen and analyzed.

1. INTRODUCTION

Fluctuations in the amplitude and phase of radio wave signals are a result of transmission through the perturbed ionosphere. Slow variations are caused by changes in the ionospheric total electron content. Relatively fast random fluctuations in the received signals' amplitude and phase are produced by ionospheric irregularities. Studies of the ionosphere's effect on communication signals are used in modeling satellite communication channels and in investigating physical characteristics of the ionosphere.

For the purpose of studying these fluctuations experimentally, analog transmissions from a radio beacon satellite are received at Natal, Brazil and are digitized and stored on a reel-to-reel type magnetic tape in a di-phase encoded form. A complete description of the digital system can be found in a report (Yang and Hearn, 1977). This thesis describes a digital system which takes the decoded scintillation data and uses a Hewlett-Packard 9825A desk calculator to selectively sample and store the data on a small tape cartridge. The HP9825A is used to analyze the data. Data analysis consists of data dropout error correcting schemes as well as computation of data autocorrelation, cross correlation power spectrum and S_4 index. Several pieces of data will be chosen and then analyzed.

2. HISTORY

2.1 Experiment Design

This thesis is concerned with a data analysis scheme for studying the scintillation of transionospheric radio signals near the equator. The geostationary satellite Marisat 1 which is located at 15.4°W longitude transmits right circularly polarized signals at 257.55 MHz, 1541.5 MHz, and a number of other frequencies. In June of 1977 a receiving system was set up on the campus of Universidade Federal do Rio Grande do Norte in Natal, Brazil. From this location the elevation angle of Marisat 1 is 66° and its azimuth angle is 74° east of north. The receiving system at Natal uses a 6-foot parabolic reflector antenna with a conical helix feed to receive the 1541.5 MHz L band signal and a helical antenna to receive the 257.55 MHz UHF signal. The system signal-to-noise ratio is 11 db at L band and 23 db at UHF band.

In addition to the University of Illinois receiving system, the Air Force has a 30-foot reflector antenna which is positioned 278 meters east of where our equipment is located. The 30-foot reflector has 16.5 db more gain than does the 6-foot reflector at L band and consequently the signal-to-noise ratio of the Air Force system is as high as 27.5 db. At the UHF band the Air Force system signal-to-noise ratio is about 27 db.

2.2 Data Logging System

The signal from each of the receiving systems is multiplexed onto a single line by a data logging system. This

the input reference signal (116 2/3 MHz) which is normally
at 2.53V. To simulate actual operating condition in equatorial

3

single line is digitized to give a 3 digit BCD data word.
A single BCD digit channel identification and a two BCD digit
frame count for timing purposes are added to the data word.
This 6 BCD digit word has 24 bits of useful information per
sample. Because of the multiplexing process each frame will
consist of one data block for each receiving channel and will
represent one sample point. In addition, 2 digits are hard-
wired into the format to be used as a flag to mark the end
of a data block. Thus, the 32 bit data block has the following
format

800	400	200	100	80	40	20	10	8	4	2	1	8	4	2	1	
DATA												CH.ID				} 32 bits
80	40	20	10	8	4	2	1	80	40	20	10	8	4	2	1	
FRAME COUNT								BLOCK END MARK								

These 32 bits are shifted serially out of a shift register
to provide a single channel of serial data. This channel is
di-phase encoded. Only a single channel is required to rep-
resent both the data and the timing clock pulses. This audio
signal is recorded on a single track of magnetic tape. The
tape is then shipped to the University of Illinois for de-
coding and analysis.

When the tape is received at Illinois it will first be
decoded. The playback from an AKAI 4400 audio tape deck is
fed into a previously built decoder device. The decoder first

reshapes and sharpens the di-phase encoded bit stream. An edge detector with decoder logics converts the di-phase encoded data back into its original bit form. The data is next shifted into a 32 bit shift register. When the flag which marks the end of the data block is detected, 24 of the bits are strobed into a parallel latch. The data will remain frozen at the output of the latch circuit until the next end mark flag is detected. In the meantime, the input data stream is fed continuously into the shift register. Outputs from the latches are available as useful data. The decoder uses a digital led device to display the contents of the latches for any channel that the user may select. The display consists of

- 3 digits -- data
- 1 digit -- channel ID.
- 2 digits -- frame count.

3. HARDWARE INTERFACE

A digital circuit has been designed and built that will act as an interface between the HP9825A desk calculator and the previously described decoder. This circuit accepts the decoded BCD data as input and then under program control, outputs the data in binary form to the HP9825A. The circuit allows the operator to choose the channel that will be analyzed and the rate at which the binary data will be sampled. This digital interface is described in the remainder of this section.

Useful BCD data is available at the output of three SN74100 eight-bit bistable latches that are found in the decoder. (I have previously explained how the di-phase encoded data is decoded and then transferred to the latches.) These latches are shown in Figure 3.1 and are labeled as being M17, M18, and M19. The output of integrated circuit M17 represents the changing frame count. The output of integrated circuit M18 contains the channel number that the data represents. The data which describes the amplitude of the received satellite signal is found on integrated circuit chips M18 and M19. The output of these three chips is wired into the hardware interface. Since the Hewlett-Packard calculator most efficiently handles binary input data, the digital interface converts the BCD data to a binary form.

We now have 24 lines of useful binary information. The calculator is not capable of accepting 24 lines of input so the information is broken up into 2 sets containing 12 lines

E



each. Three SN74157 chips are used to switch between the two data sets in a way that allows the calculator to read first the amplitude data and then upon stimulus from the interface, read the channel and frame count data. Success of this data transfer scheme depends entirely on the calculator reading the 12 output lines at precisely the right moment.

The circuit in Figure 3.2 shows how the READ STROBE signal is generated. This signal is sent to the H.P. calculator and controls when all data transfer operations take place. The first part of the circuit is the SAMPLE RATE CONTROL. The user selects the rate that will be used when sampling the digital data stream. The five possible choices are 1, 2, 4, 10 and 20 Hz. The data was originally sampled at a 20 Hz rate. If in the data analysis the user wishes to analyze every possible point he would re-sample the data at a 20 Hz rate. If longer data lengths were desired every other point could be sampled (10 Hz rate) or every twentieth data point could be sampled (1 Hz rate). For example, assume that the user wants to sample the data at a 2 Hz rate. Every tenth data point will be recorded. To guard against the possibility of having a data point drop out and then consequently sampling future points at the wrong time, the frame count is decoded and only those points that have an associated frame count of 5, 15, 25, . . . , or 95 will be sampled. Thus the

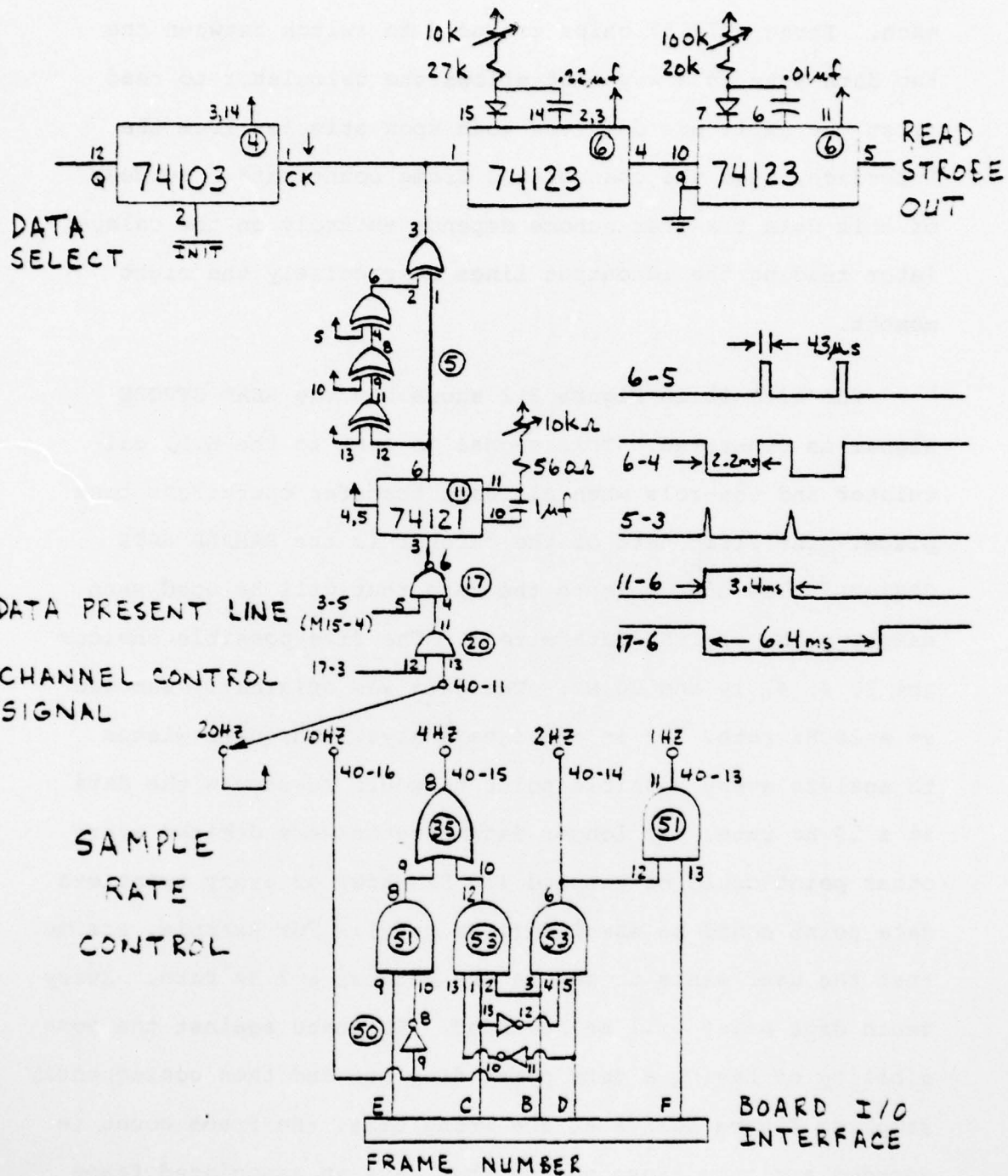


Figure 3.2. Sample Rate Control Circuit.

sampling technique is immune from some errors caused by data dropouts. The output of the SAMPLE RATE CONTROL is a 1 whenever data should be sampled and a 0 otherwise.

The output of the SAMPLE RATE CONTROL is ANDED with the CHANNEL CONTROL SIGNAL. The user selects the channel of the data that he wants to record. When data is present, and the channel describing the data is identical to the one that the user has selected, the CHANNEL CONTROL SIGNAL is high. At all other times it is low. Thus far the circuit has determined 1) when data is present 2) when the data represents the user selected channel and 3) if the data has a frame number that corresponds to a frame that should be sampled. When these three conditions are true, pin 6 of integrated circuit 17 is low. It is normally high.

Pin 6 will be low for a duration of 6.4 ms. During this time all 24 lines of data will be sampled by the HP9825A and then temporarily stored in internal memory. The procedure for recording the data follows. When pin 6 makes a transition from a high to a low state, the output of J-K Flip-Flop SN74103 toggles low. Figure 3.1 shows how this output, which is labeled 4-12, is wired to each of the three data multiplexers. In this case it causes the A inputs of the multiplexer to be copied onto the 12 output lines. After 2.2 ms the READ STROBE OUT line pulses high. The response of the calculator is to read the status of the twelve data lines. The B inputs are then copied onto the 12 output lines.

After a short period the READ STROBE OUT pulses high and the data corresponding to the channel and frame number is stored in the computer. The circuit that controls these data transfer operations is shown in Figure 3.2 along with the associated timing diagrams.

For a calculator input operation, when data is transferred from the interface to the calculator, the READ STROBE OUT signal indicates to the calculator that a read operation should take place. Figure 3.3 shows the method used in synchronizing the data exchanged between the calculator and the interface. The I/O line tells the interface which direction data is to be transferred, low indicates a calculator output operation, high indicates a calculator input operation. When data is to be sampled, a computer program read command causes the I/O line to go high. This disables output pin 1 of chip 36. The READ STROBE signal is then output to the calculator on the PFLG line. When the PFLG line makes a transition from a "busy" to a "ready" state the calculator will read the status of all of its data lines. This information is then stored in the calculator's memory.

At the start of any sampling operation the hardware interface must be initialized. Counters must be reset and flip-flops must be set to proper states. This requires a calculator output operation. When the I/O line is forced low the READ STROBE input is disabled and the PCTL input is enabled. The PCTL line changes from a control clear to a control set status indicating that output data is available

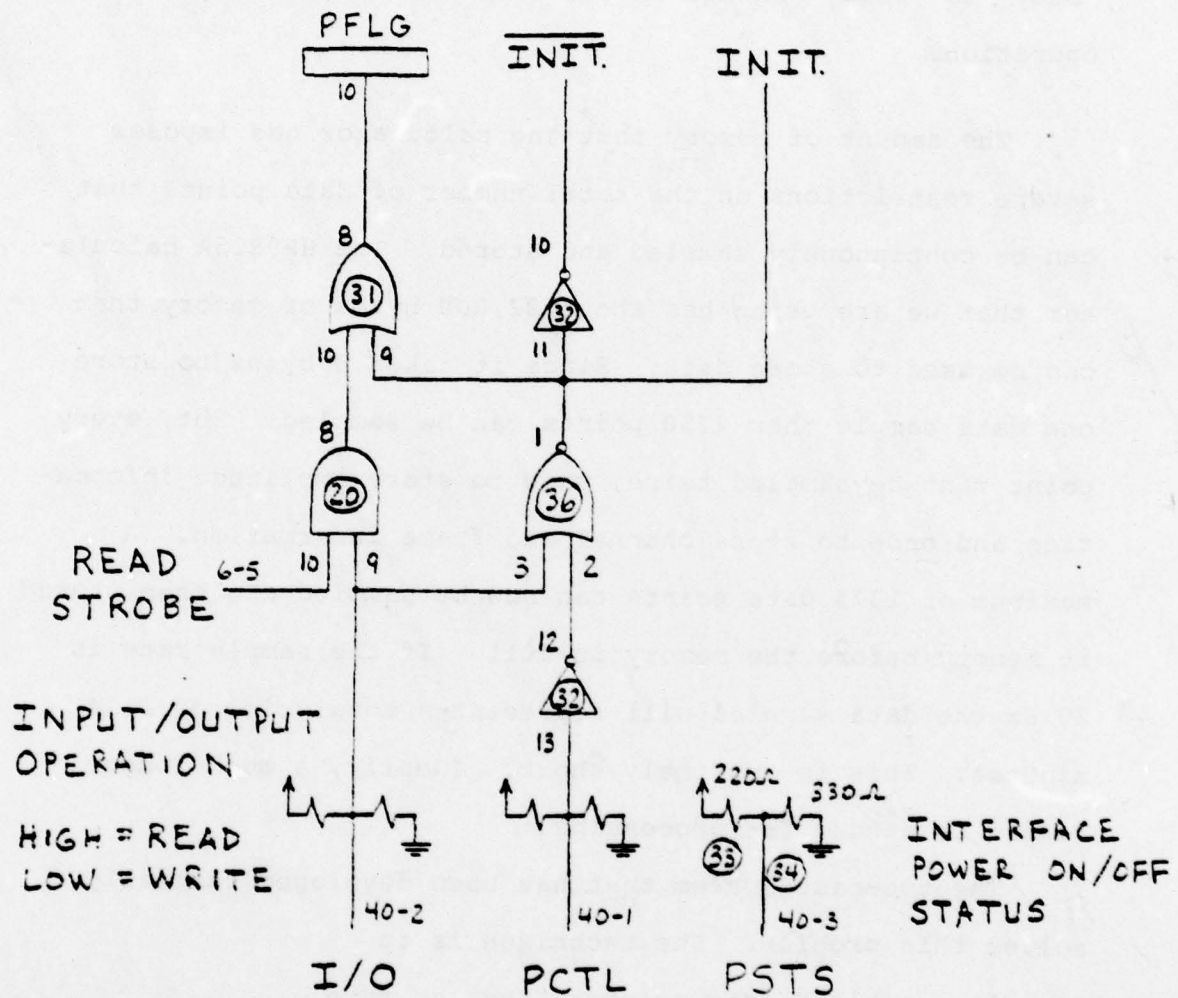


Figure 3.3. Data Transfer Synchronization Circuit.

on the output lines. This triggers a change in the INIT. and the INIT. lines that causes the circuit to be reset. The "busy" to "ready" change in the PFLG line completes the write operation.

The amount of memory that the calculator has imposes severe restrictions on the total number of data points that can be continuously sampled and stored. The HP9825A calculator that we are using has about 22,000 bytes of memory that can be used to store data. Since it takes 8 bytes to store one data sample then 2750 points can be sampled. But, every point must be sampled twice, once to store amplitude information and once to store channel and frame information. A maximum of 1375 data points can now be sampled and then stored in memory before the memory is full. If the sample rate is 20 Hz the data sampled will represent a total time of 1.14 minutes. This is extremely short. Ideally, a much longer record is needed for processing.

The two-pass system that has been developed partially solves this problem. The technique is to

- 1) sample N data points; store on tape
- 2) wait for N points to pass
- 3) sample N data points; store on tape
- 4) rewind data tape to identical starting point used in 1).
- 5) wait for N points to pass
- 6) sample N data points; store on tape
- 7) wait for N points to pass
- 8) sample N data points; store on tape.

In this system $4 \cdot N$ data points are sampled. When the blocks are interlaced properly all $4N$ data points will be continuous.

The circuit shown in Figure 3.4 controls the two-pass system. As soon as frame count "0" is detected the point counter is reset. The next 1024 data points that are sampled advance the counter one each. After 1024 points have been sampled the output of the J-K flip-flop goes low, ending the sampling operation. The calculator stores the data on a small tape cartridge. Meanwhile, the counter is counting out the next 1024 data points. At the end of the count, the counter is reset, the flip-flop is reset, and sampling resumes. When 1024 data points are sampled the data tape is rewound to the original starting point. The operation repeats itself with the exception that sampling and waiting tasks are reversed.

Data points are sampled at a very regular interval that is equal to the sampling interval. If a data point drops out it will not be sampled but to keep the timing information accurate it must be counted. The MISSING PULSE DETECTOR circuit shown in Figure 3.4 determines when a data point drops out, and in these cases inserts a pulse that will advance the counter. The counter will always indicate the number of data points that should have been detected and will not be in error due to data dropouts.

The four preceding circuits are combined into a total system in Figure 3.5. This data transfer system takes the

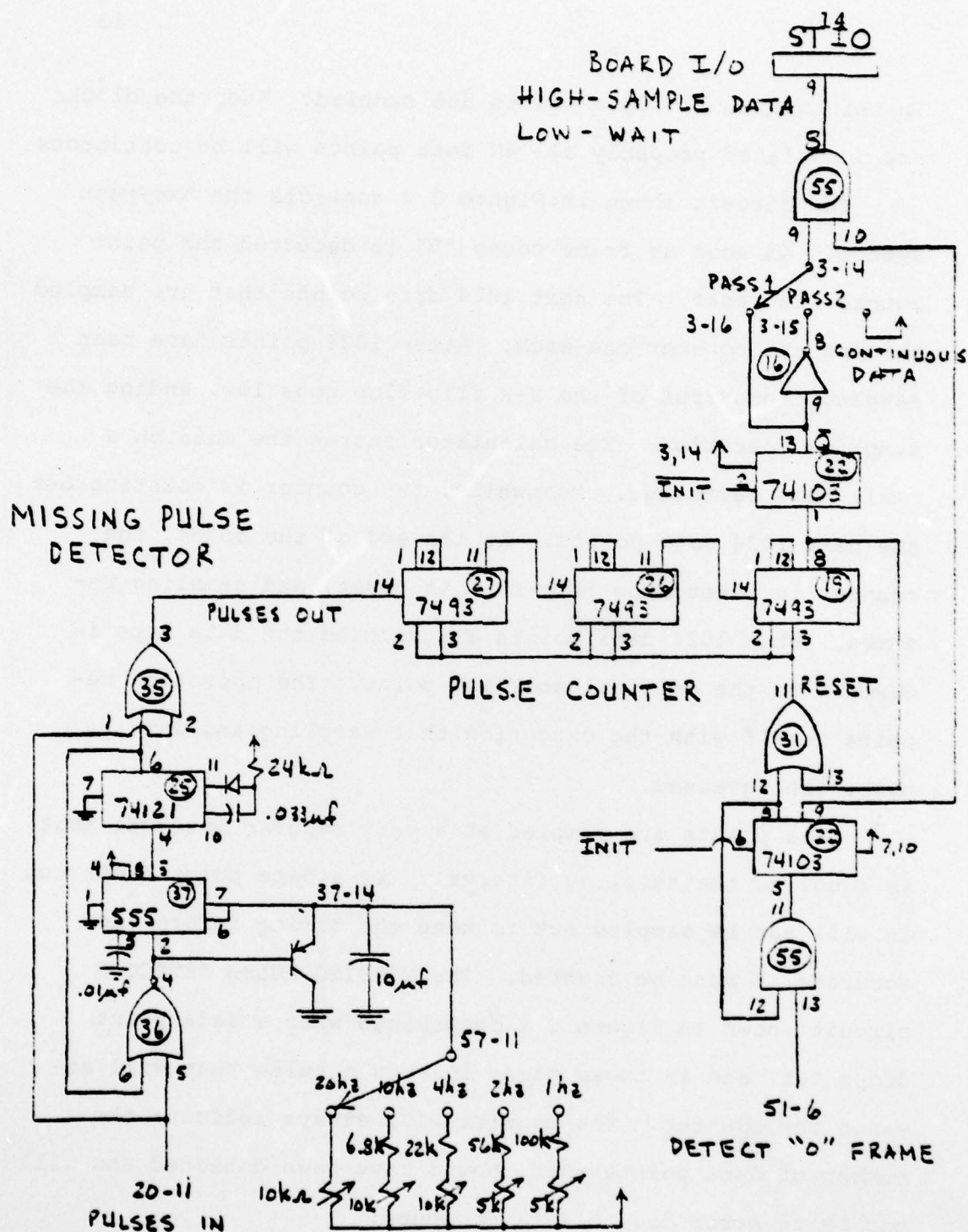


Figure 3.4. Two-Pass System Control Circuit.

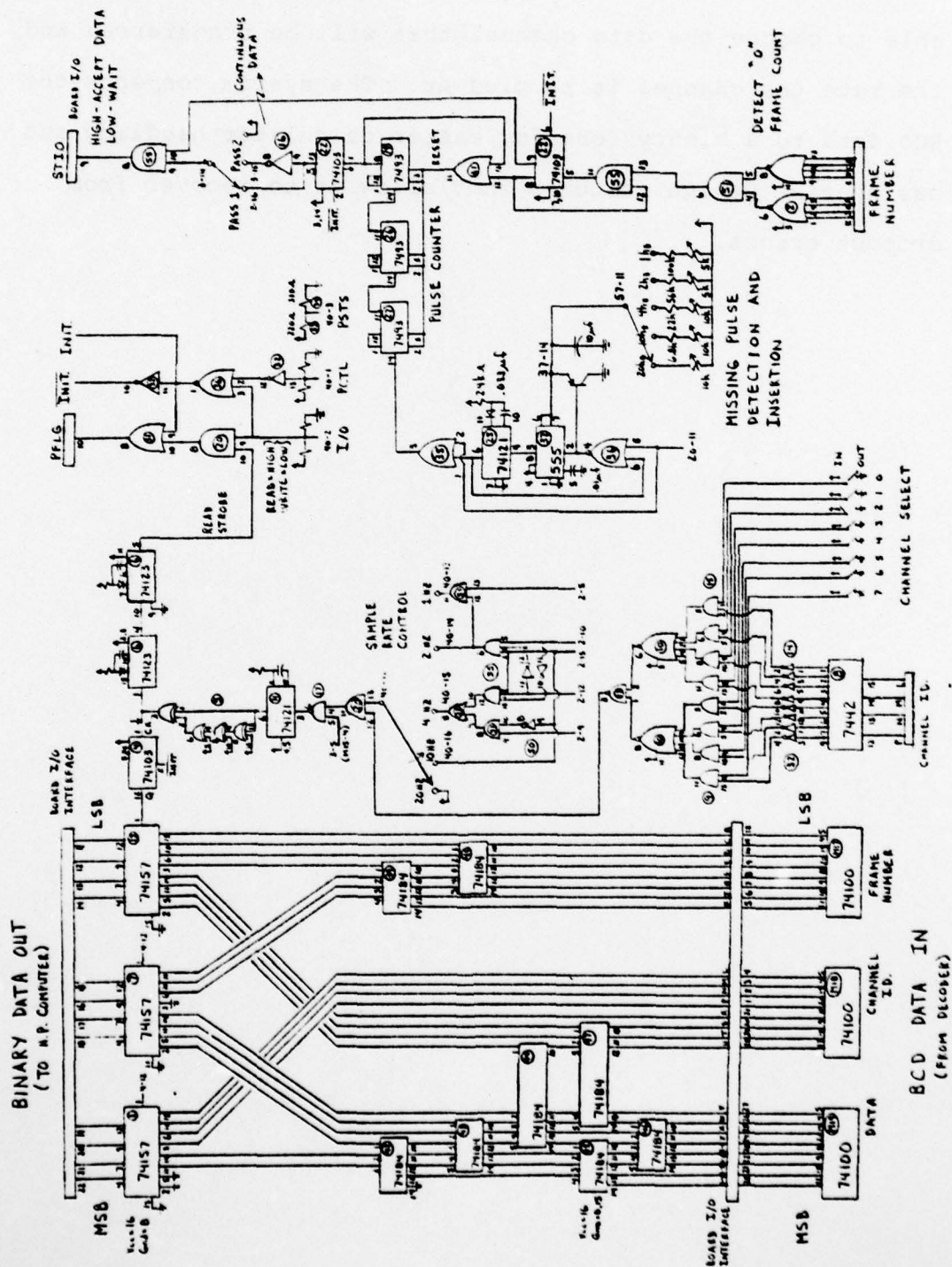


Figure 3.5. Data Transfer System.

decoded scintillation data and transfers it to the HP9825A calculator. The data can then be analyzed. The operator is able to choose the data channel that will be transferred and the rate the channel is sampled at. The system converts the BCD data to a binary form for easier calculator handling and has special design features that allow it to recover from dropout errors.

4. DATA ANALYSIS

4.1 Sampling Data

To analyze the data it must first be transferred from the 7-inch magnetic tape to the small H.P. tape cartridge. It can then be accessed under program control. In Natal, the analog satellite transmissions were sampled at a rate of 20 Hz and then digitized and recorded on tape. When the data is decoded the programmer must choose to sample the decoded data stream at one of the following rates: 20 Hz, 10 Hz, 4 Hz, 2 Hz or 1 Hz. Since the total memory capacity of the calculator is fixed, the choice of sampling rate is a trade-off between high resolution and increased record length in seconds. The programmer must also select the channel that will be sampled. Thus, there is control over which communication channel will be studied.

4.2 Error Correcting Schemes

When collecting data many errors will occur. If the conclusions drawn from the data analysis are expected to be accurate then it is necessary to be able to locate the obvious errors and then apply appropriate correction schemes. For the data logging system that has been described previously the information has been recorded in terms of its amplitude and a changing frame count. Timing information is recorded alongside of the amplitude information. Thus, if a data point drops out or is not detected, a careful study of the timing information would reveal that the data is not continuous.

If the timing information also indicates that the addition of one data point would make the data continuous about the dropout position then an automatic error correcting scheme can be used.

A computer program has been developed that will automatically locate many of the most common timing errors and then apply a correction technique. The program works in the following way.

Let $X(t)$ represent the amplitude of the received analog satellite transmission as a function of time. Let $F(t)$ describe a changing integer frame count that satisfies

$$F(t+T_s) = \begin{cases} F(t)+1 & \text{if } 0 \leq F(t) \leq 98 \\ 0 & \text{if } F(t) = 99 \end{cases}$$

where T_s is the sampling interval.

We describe the data set D that results when $F(t)$ and $X(t)$ are sampled simultaneously every T_s seconds as

$$\begin{aligned} D(i) &= F([i+1]T_s/2) & i &= 1, 3, 5, \dots, 2N-1 \\ D(i+1) &= X([i+1]T_s/2). \end{aligned}$$

Because of the way that $F(t)$ is defined we know that for all odd values of i

$$D(i+2) - D(i) = 1 \text{ or } -99.$$

A computer routine checks the preceding condition for all

odd i . If it is not met for a particular value of i a timing error has been discovered. I call this value of i , i_e . If further analysis reveals that the insertion of one sample pair at location i_e would cause the data to be continuous about i_e then one sample pair will be inserted. A single sample pair is inserted by ① making room for the new data by relocating all data pairs that are described by having i greater than i_e+1 , ② defining the new frame count to equal $D(i_e)+1$, and ③ using an averaging method to predict what the amplitude of the signal $X([i+1]T_s/2)$ was for $i=i_e+2$. This averaging method equates the unknown amplitude value to be equal to the average of the immediately preceding and immediately following sampled amplitude values. If the data has been sampled much faster than twice the highest frequency component of interest then this correction technique should reduce the error to a tolerable level.

When collecting and recording digital data under noisy conditions it is possible that a "0" may be interpreted as a "1" or that a "1" may be interpreted as a "0". This type of error will cause a large or small change in the timing or amplitude of the data. The amount of change is determined by the position of the bit. I have previously described a program that uses frame count information to correct timing errors in the data. I will now describe a way to reduce the magnitude of errors found in the amplitude part of the data when caused by the above source.

UNCLASSIFIED

UIIU-ENG-79-2559

ARO-14260.8-ELX

NL

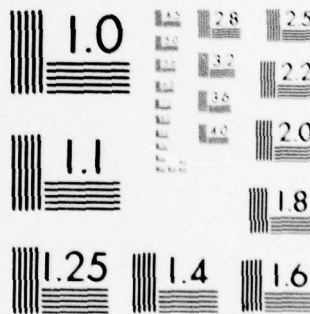
3 OF 3

AD
A076622

END
DATE
FILMED

12-79

DDC



MICROCOPY RESOLUTION TEST CHART
NATIONAL BUREAU OF STANDARDS-1963-A

Assume that one of the twelve bits used to describe the amplitude of a sampled data point has been misinterpreted. Since the data is coded in a BCD form, an error in one bit will cause a change in amplitude ranging from 1 to 800. A large change in the magnitude of any one data point will result in a very noticable discontinuity when compared with adjacent data points. A computer program has been written that will locate and then perform an averaging correction on each discontinuity that is greater than an arbitrary level.

This level will be a function of the data and must be large enough so that rapid changes in the data will not be effected, but small enough so that large discontinuities in the data caused by errors can be identified. Thus, if the data is slowly varying the level can be set low. If the data varies rapidly the level must be set high. Let $X(t)$ represent the amplitude of the received signal at time t . A correctable discontinuity is said to exist whenever

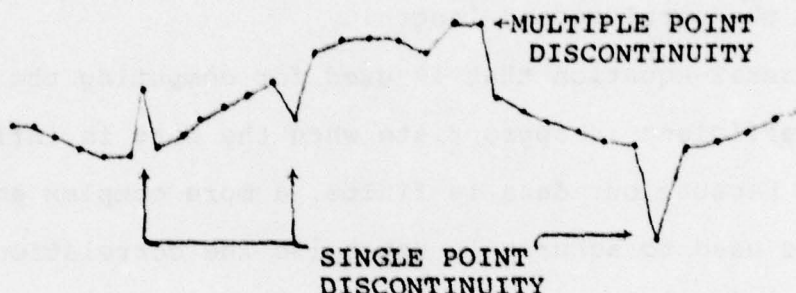
$$X([i+1]T_s) - X(iT_s) > S \quad i=1,2,\dots,N-1$$

where T_s is the sampling interval and S is defined to be

$$\frac{2.5}{N} \sum_{i=1}^{N-1} |X([i+1]T_s) - X(iT_s)| = S.$$

When a discontinuity is found, the program first determines whether the discontinuity involves a single point or

involves more than one point.



For a multiple point discontinuity the location is noted and the program operator is notified. Single point discontinuities are handled automatically. For single point discontinuities, the value of the data where the discontinuity exists is set equal to the average of the amplitudes of the immediately preceding and immediately following points.

This error correcting scheme will not identify transmission errors when the resulting discontinuity is less than level S. However, in these cases the error should be small and should have negligible effects on future data analysis.

4.3 Autocorrelation

After the data has been cleaned-up by the use of error correcting programs it is ready to be analyzed. The autocorrelation of the data is determined first.

In a typical situation the data is sampled at a 20 hz rate. The available memory in the HP9825A calculator limits the number of data samples used in a correlation routine to 1024. Thus the maximum duration of the data that can be correlated is limited to 51.2 seconds. This is a short piece

of data and consequently, the confidence in the results of the autocorrelation will be reduced for displacements greater than 10% of the total record length.

The general equation that is used for computing the correlation coefficient is appropriate when the data is infinite in length. Because our data is finite, a more complex equation must be used to accurately determine the correlation coefficient. Starting with a finite, non-zero mean data set given by

$$X(iT_s) \quad i=1,2,\dots,N$$

where T_s is the sampling interval and $X(iT_s)$ is the amplitude of the received satellite signal, the coefficient of correlation k units apart is computed from

$$r_k = \frac{\sum_{i=1}^{N-k} (X(iT_s) - \bar{X}') (X[(i+k)T_s] - \bar{X}'')}{\sqrt{\sum_{i=1}^{N-k} (X(iT_s) - \bar{X}')^2 \sum_{i=1}^{N-k} (X[(i+k)T_s] - \bar{X}'')^2}}$$

where

$$\bar{X}' = \frac{1}{N-k} \sum_{j=1}^{N-k} X(jT_s)$$

$$\bar{X}'' = \frac{1}{N-k} \sum_{j=1}^{N-k} X[(j+k)T_s]$$

and $N=1024$. Notice that the mean is computed after every change in the displacement k and is based on only the remaining $N-k$ data values.

4.4 Cross Correlation

The cross correlation of two signals can be computed using a method that is similar to the one used when computing the autocorrelation function. When given two sampled signals $X(iT_s)$ and $Y(iT_s)$ where $i=1,2,\dots,N$ the coefficient of correlation k units apart is computed from

$$r_k' = \frac{\sum_{i=1}^{N-k} (X(iT_s) - \bar{X})(Y[(i+k)T_s] - \bar{Y})}{\sqrt{\sum_{i=1}^{N-k} (X(iT_s) - \bar{X})^2 \sum_{i=1}^{N-k} (Y[(i+k)T_s] - \bar{Y})^2}}$$

where

$$\bar{X} = \frac{1}{N-k} \sum_{j=1}^{N-k} X(jT_s)$$

$$\bar{Y} = \frac{1}{N-k} \sum_{j=1}^{N-k} Y[(j+k)T_s].$$

4.5 Fourier Transform

In order to compute the power spectrum of the data the Fourier transform of the data must first be determined. This thesis uses a special computation procedure, taken from Brigham (1974), to compute the discrete Fourier transform

of a $2N$ point function by means of an N point transform.
The procedure is outlined below.

Given the sampled values of the received signal

$$x(i) \quad i=0,1,2,\dots,2N-1$$

where $N=1024$, first compute the mean of the sampled values
from

$$M = \frac{1}{2N} \sum_{i=0}^{2N-1} x(i).$$

Now subtract the mean from each of the sampled values.

$$x'(i) = x(i) - M \quad i=0,1,2,\dots,2N-1$$

Transforming any piece of finite data has the same effect as multiplying the data by a rectangular window and transforming the product. Since multiplication in the time domain corresponds to convolution in the frequency domain, the spectrum of the data is convolved with the Fourier transform of the window function. The spectrum of the data is thus distorted by the window function. Since the Fourier transform of a Hanning window has much lower sidelobes than the transform of a rectangular window, distortion by sidelobe effect will be reduced with a slight sacrifice in resolution if the data is multiplied by a Hanning window function. The Hanning window function is defined to be

$$W(i) = \begin{cases} .5 - .5 \cos \left(\frac{360i}{2N} \right) & , i=0,1,\dots,2N-1 \\ 0 & , \text{elsewhere.} \end{cases}$$

Multiply the data by the Hanning window function to obtain

$$x''(i) = (.5 - .5 \cos [\frac{360i}{2N}]) x'(i), \quad i=0,1,\dots,2N-1.$$

Divide $x''(i)$ into two functions

$$h(i) = x''(2i) \quad , \quad i=0,1,\dots,2N-1$$

$$g(i) = x''(2i+1).$$

Form the complex function

$$y(i) = h(i) + jg(i) \quad , \quad i=0,1,\dots,2N-1.$$

The Fourier transform of $y(i)$ is defined to be

$$\begin{aligned} Y(n) &= \sum_{i=0}^{N-1} y(i) e^{-j2\pi ni/N}, \quad n=0,1,\dots,N-1 \\ &= R(n) + jI(n) \end{aligned}$$

where $R(n)$ and $I(n)$ are the real and imaginary parts of $Y(n)$, respectively. To save computation time a Fast Fourier Transform (FFT) routine is used to compute the discrete transform.

The output of the FFT program must now be converted into meaningful transform data. This is necessary because we originally start with $2N$ real data points and then transform N real and N imaginary points. The real and imaginary parts of the $2N$ point discrete transform of $x''(i)$ are respectively given by

$$\begin{aligned} X_r(n) &= .5([R(n) + R(N-n)] + [I(n) + I(N-n)] \cos \frac{\pi n}{N} \\ &\quad - [R(n) - R(N-n)] \sin \frac{\pi n}{N}) \end{aligned}$$

$$\begin{aligned}
 X_i(n) = & .5([I(n)-I(N-n)]-[I(n)+I(N-n)] \sin \frac{\pi n}{N} \\
 & - [R(n)-R(N-n)] \cos \frac{\pi n}{N}) \\
 & , n=0,1,\dots,N-1.
 \end{aligned}$$

The output of the Fourier transform program will now be examined. The input to the program is $2N$ real sample values ($N=1024$) that are separated in time by the sampling interval T_s . The output of the program is 1024 real values (even function) and 1024 imaginary values (odd function). Adjacent data points are separated in frequency by

$$f = \frac{1}{2NT_s} = \frac{f_s}{2N}.$$

$X_r(n)$ and $X_i(n)$ represent the n th components of the real and imaginary parts of the Fourier transform. The frequency that the n th component corresponds to can be written as

$$f = \begin{cases} \frac{nf_s}{2N} & n=0,1,\dots,\frac{N}{2}-1 \\ \frac{f_s}{4} \text{ and } \frac{-f_s}{4} & n=\frac{N}{2} \\ \frac{-(N-n)f_s}{2N} & n=\frac{N}{2}+1, \frac{N}{2}+2,\dots,N-1. \end{cases}$$

4.6 Power Spectrum

To plot a normalized power spectrum the total power in the spectrum must first be determined. For discrete functions, the relationship between power as computed in the time domain and as computed in the frequency domain is given by

$$\sum_{i=0}^{N-1} x^2(i) = \frac{1}{N} \sum_{n=0}^{N-1} |X(n)|^2.$$

This is known as Parseval's theorem. We have used a special computation procedure to compute the discrete Fourier transform of a $2N$ point function by means of an N point transform. Because of this Parseval's theorem becomes

$$\sum_{i=0}^{2N-1} x^2(i) = \frac{1}{2N} \sum_{n=0}^{N-1} |X(n)|^2.$$

The total power in $x(t)$ is given by

$$\int_0^T x^2(t) dt.$$

If we let $2N=T/T_s$ then for small T_s

$$\int_0^{2NT_s} x^2(t) dt \approx \sum_{i=0}^{2N-1} x^2(iT_s) T_s.$$

The total power in the spectrum must be

$$P = \frac{T_s}{2N} \sum_{n=0}^{N-1} [X_r^2(n) + X_i^2(n)].$$

This is expressed in decibels as

$$10 \log(P) \text{ db.}$$

To plot the positive frequency portion of the normalized power spectrum the magnitude of every point must be

normalized. Therefore, the n th point in the power spectrum will be plotted with a magnitude of

$$10 \log \left(\frac{2T_s^2}{P} [X_r^2(n) + X_i^2(n)] \right)$$

and a frequency of

$$\frac{n}{2NT_s}.$$

4.7 S_4 Index

The S_4 index is a positive number, normally ranging between 0 and 1, that gives an indication of the severity of scintillation. If the S_4 index is less than .3 the scintillation is described as being weak. For S_4 values greater than .7, scintillation is strong. On occasion the S_4 index can be greater than 1. This would suggest that there may exist focussing effects.

If the amplitude of the received satellite transmission is sampled every T_s seconds and given by

$$X(iT_s) \quad i=1,2,\dots,N$$

then the S_4 index is computed from

$$S_4 = \sqrt{\frac{V-M^2}{M^2}}$$

where

$$V = \frac{1}{N} \sum_{i=1}^N X^*(iT_s)$$

$$M = \frac{1}{N} \sum_{i=1}^N X^2(iT_s).$$

5. RESULTS

Using the computer software described in previous sections, three pieces of data have been analyzed. In this section of the report the results of the data analysis for data recorded on September 7, 1977 will be discussed. The statistical analysis of the two remaining pieces of data is given in the Appendix but is not discussed. For the cases chosen, a single piece of data is composed of 2048 sample points. Since the channel was sampled at a 20 Hz rate, the record length spans a time of 102.4 seconds. Channel 1 refers to the signal received by the University of Illinois receiving system. Channel 2 refers to the signal received by the Air Force receiving system. The Air Force antenna is located 278 meters east of the University of Illinois antenna.

Figure 5.1 is a plot of 102.4 seconds of scintillation data that was recorded by the University of Illinois receiving system at an approximate time of 01:07 U.T. The amplitude scaling is relative, i.e. the fluctuation of the amplitude is linear relative to some arbitrary base value. It can be seen that the data goes thru large positive and negative variations with respect to its mean value. We can quantify this last statement by computing the S_4 index of the data record. The S_4 index is a measure of the severity of scintillation. As given in Figure 5.1, the S_4 index of the data is .566. This would indicate that scintillation is moderately strong. Visual inspection of the data reveals that the data is noisy. This

SEPT 7 1977

Amplitude

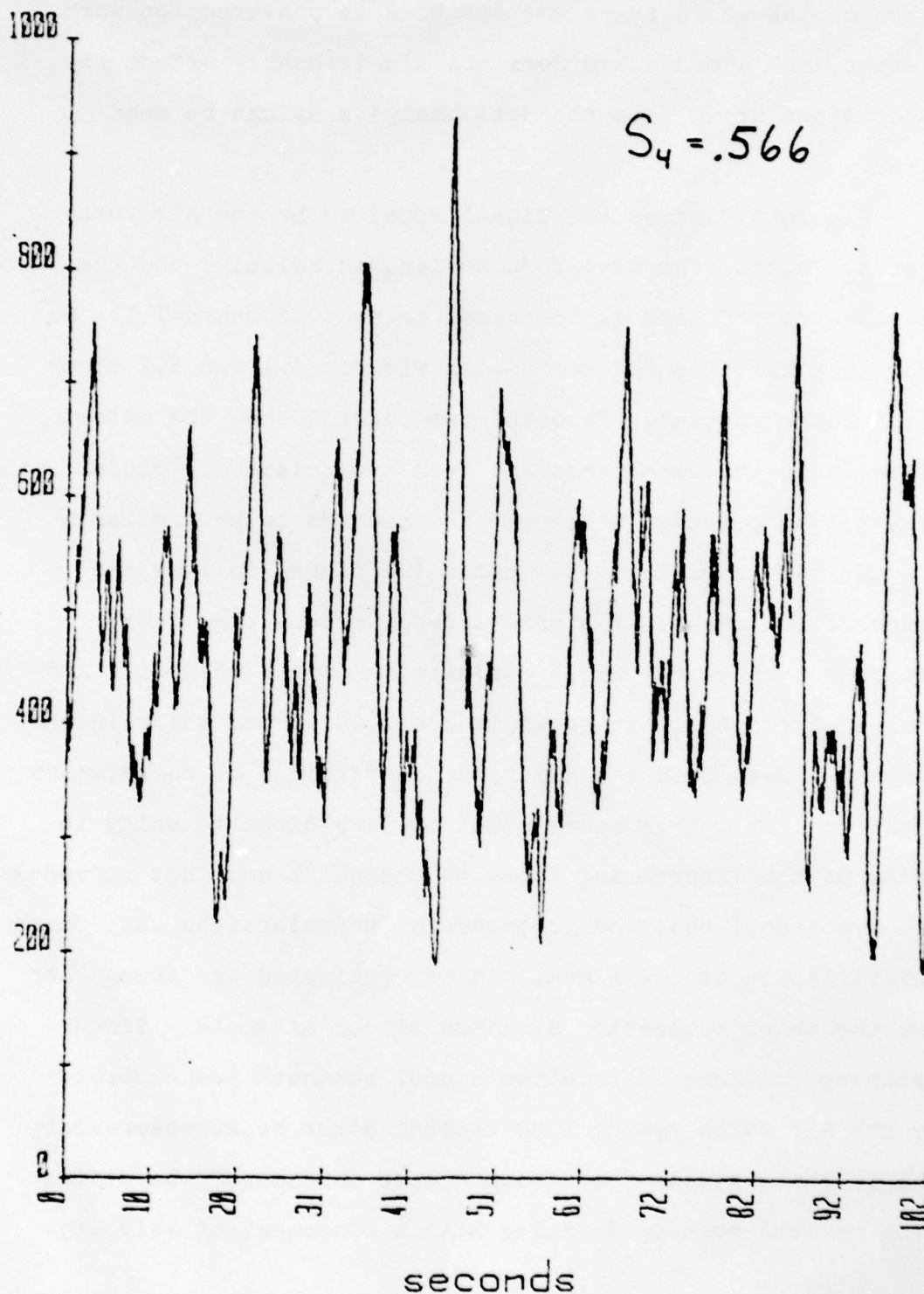


Figure 5.1. Scintillation data - Channel 1 (01:07 UT).

might be caused by the fact that the University of Illinois antenna is on the Universidade Federal do Rio Grande do Norte campus where there was appreciable construction work. However, the added noise does not significantly affect the conclusions drawn from the data analysis as can be seen later.

Figure 5.2 shows the signal received by the Air Force system. Again, the amplitude scaling is relative and the absolute record time is identical to that of channel 1. We know that the time "0" seconds in Figures 5.1 and 5.2 occur at the same instant. Thus the two records show the effect of studying the same phenomena from two relatively close observation points. We expect the records to be similar, and they are similar. The channel 2 signal follows the shape of the channel 1 signal after a slight time delay. Figure 5.3 shows the cross correlation of the channel 1 and channel 2 records. It shows that a 2.00 second shift in the channel 2 data produces a maximum coefficient of correlation equal to .905. This coefficient is very close to unity in spite of the interfering noise on channel 1 and thus supports the hypothesis that the ionospheric irregularities that cause scintillation of the signal can be considered as "frozen-in" for the short separation distance of our antennas. Since matching contours of received signal strength are observed by the Air Force system 2.00 seconds after being observed by the Illinois system the "frozen" distribution of the diffraction pattern must be drifting with a component of velocity

SEPT 7 1977

Amplitude

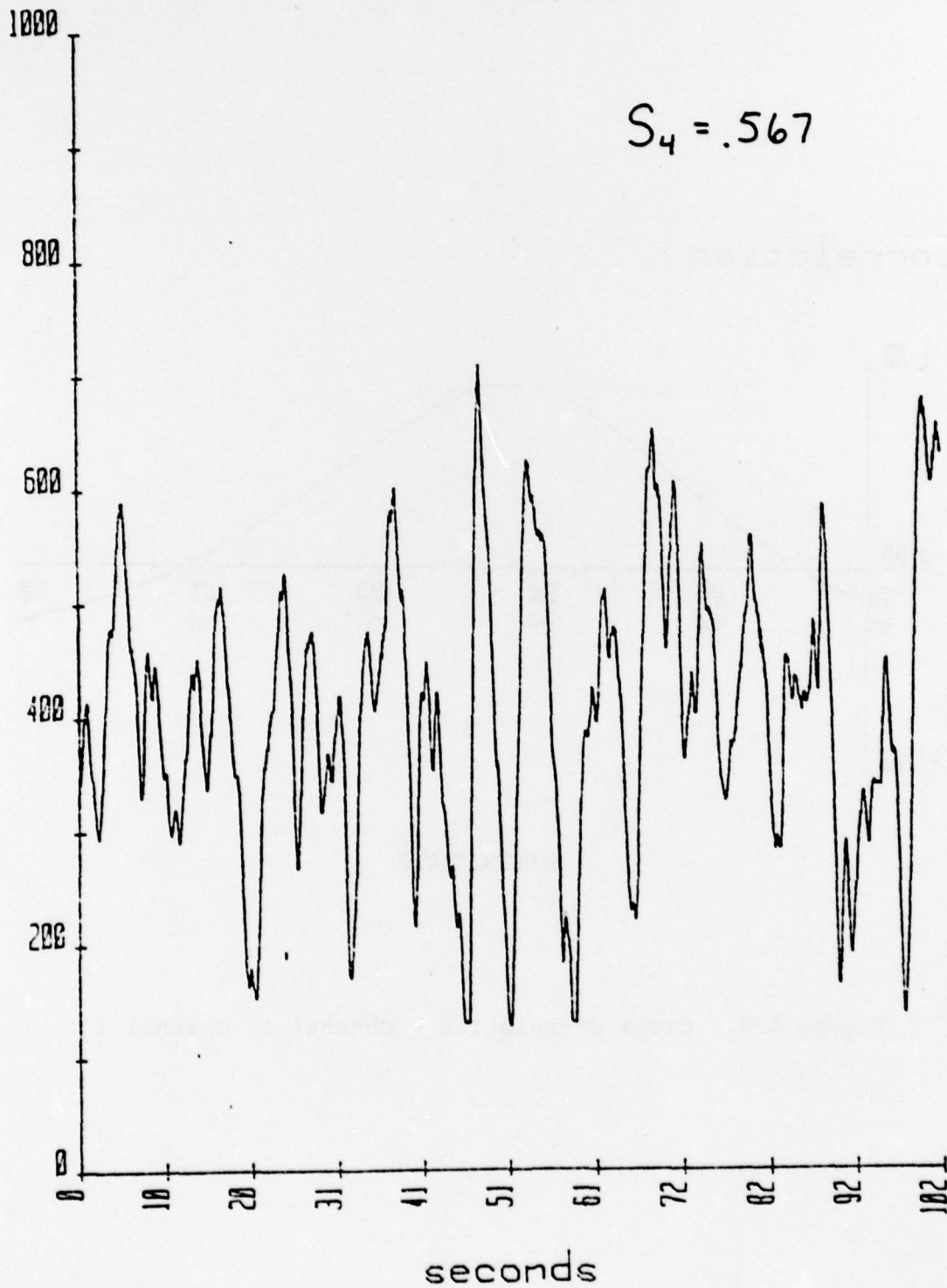


Figure 5.2. Scintillation data - Channel 2 (01:07 UT).

SEPT 7 1977

Correlation

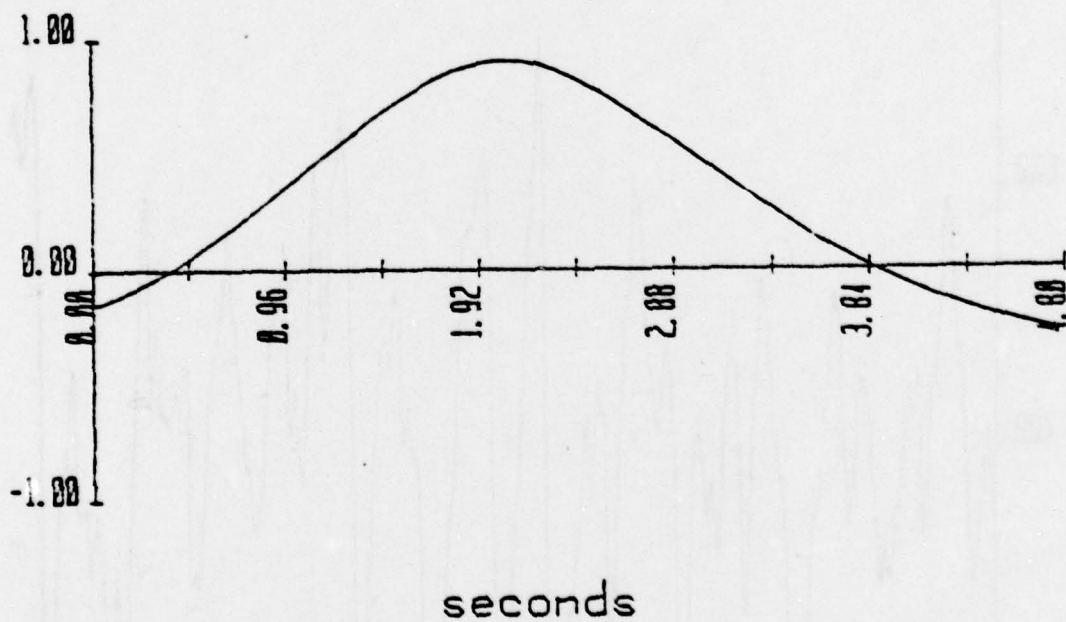


Figure 5.3. Cross Correlation - Channel 1, Channel 2

equal to

$$V_d = \frac{278\text{m}}{2.00\text{s}} = 139 \text{ m/s}$$

to the east.

Figures 5.4 and 5.5 give the autocorrelation function for channel 1 and channel 2 records respectively. Since the data has a finite length the maximum displacement of the autocorrelation function was limited to 5% of the total record length. Thus there is high confidence in the computed correlation functions. One of the most important features of the correlation function is its correlation interval. The correlation interval is the time displacement of the data that is required to reduce the correlation to zero. This can be used to give us an indication of how fast the signal fades. Figure 5.4 shows that the correlation interval for channel 1 data is 1.75 seconds. For the Air Force data the correlation interval is 1.83 seconds. Because of the high degree of cross correlation between the two channels you would expect the fading rates and autocorrelation functions to be as closely matched as Figures 5.4 and 5.5 show them to be. The time it takes for the autocorrelation coefficient to reduce from 1 to .5 is approximately 1 second for both channel 1 and channel 2 data. This shows close agreement with the results obtained by Mullen et al. (1977) for 254 MHz data recorded at Huancayo, Peru.

If we compute the Fourier transform of the channel 1 and channel 2 data we will be able to analyze the power spectra

SEPT 7 1977

Correlation

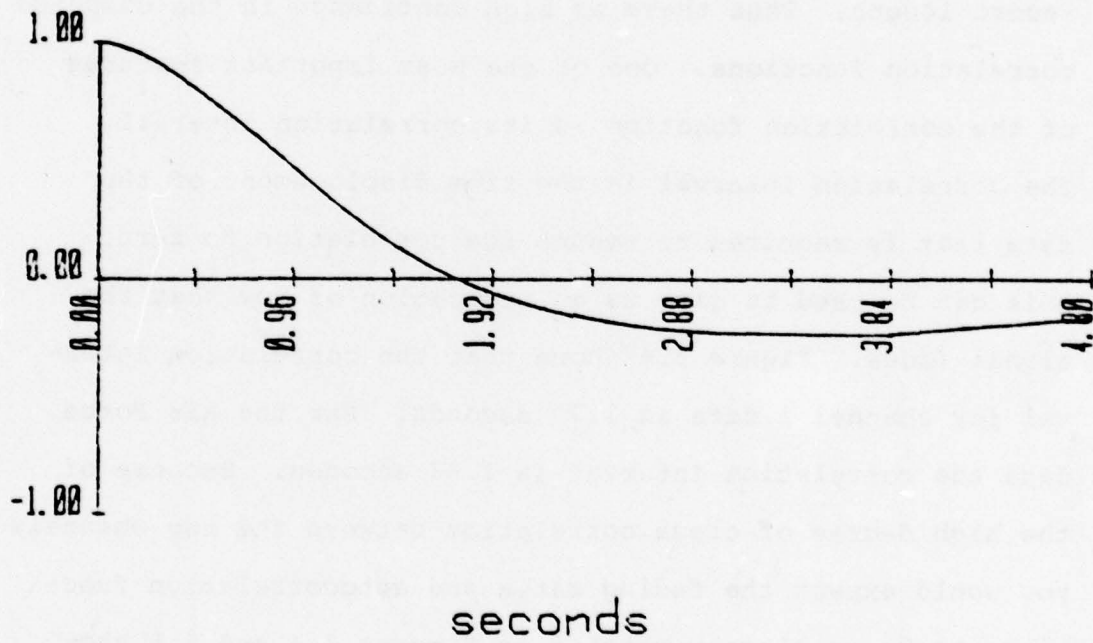


Figure 5.4. Autocorrelation - Channel 1.

SEPT 7 1977

Correlation

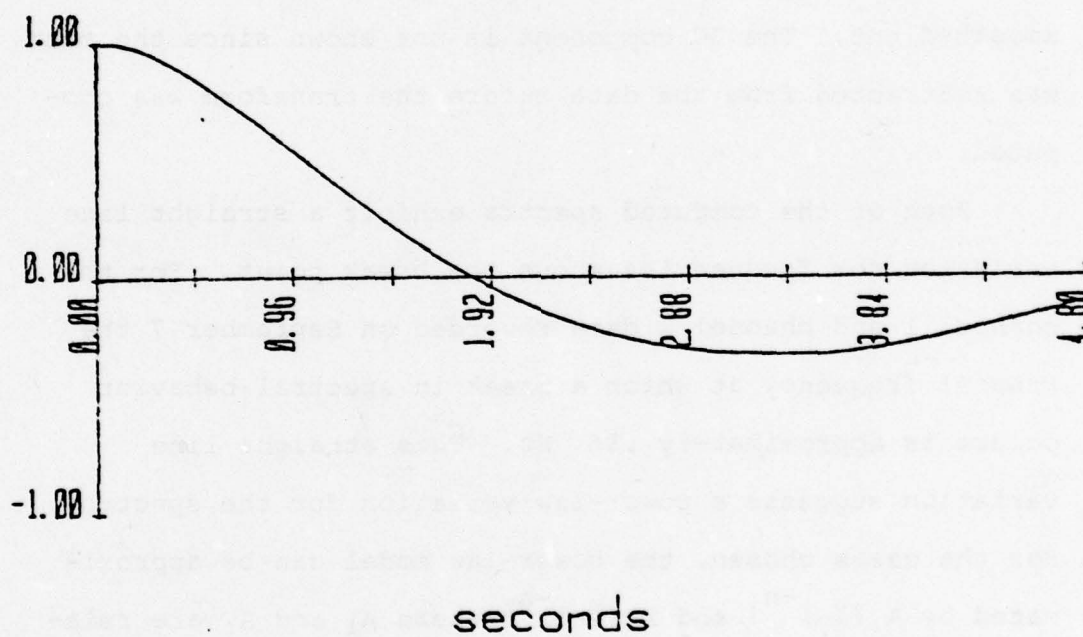


Figure 5.5. Autocorrelation - Channel 2.

of the ionospheric radio scintillations. Figures 5.6 and 5.7 show the normalized power spectrums for the University of Illinois data and the Air Force data. A normalized spectrum with power expressed in dB and frequency dependence plotted logarithmically is shown because it emphasizes the important characteristics of the transformed data.

The spectrum shown in Figure 5.7 is relatively flat for low frequencies. A longer piece of data would show this more clearly since the abrupt changes in magnitude would be smoothed out. The DC component is not shown since the mean was subtracted from the data before the transform was computed.

Both of the computed spectra exhibit a straight line variation for frequencies above the break point. For the channel 1 and channel 2 data recorded on September 7 the Fresnel frequency at which a break in spectral behavior occurs is approximately .16 Hz. This straight line variation suggests a power-law variation for the spectrum. For the cases chosen, the power-law model can be approximated by $A_1 \left(\frac{\nu}{\nu_F}\right)^{-n_1}$ and $A_2 \left(\frac{\nu}{\nu_F}\right)^{-n_2}$ where A_1 and A_2 are relative magnitudes, $\nu_F = .16$ Hz and is the Fresnel frequency, and the exponents $n_1 = 3.4$ and $n_2 = 3.6$ characterize the slope of the line.

For frequencies above 1.5 Hz the spectrum in Figure 5.6 starts to level off. At this point the signal power is very small and partially contaminated by noise. Because the Air

NORMALIZED POWER SPECTRUM

Magnitude in DB

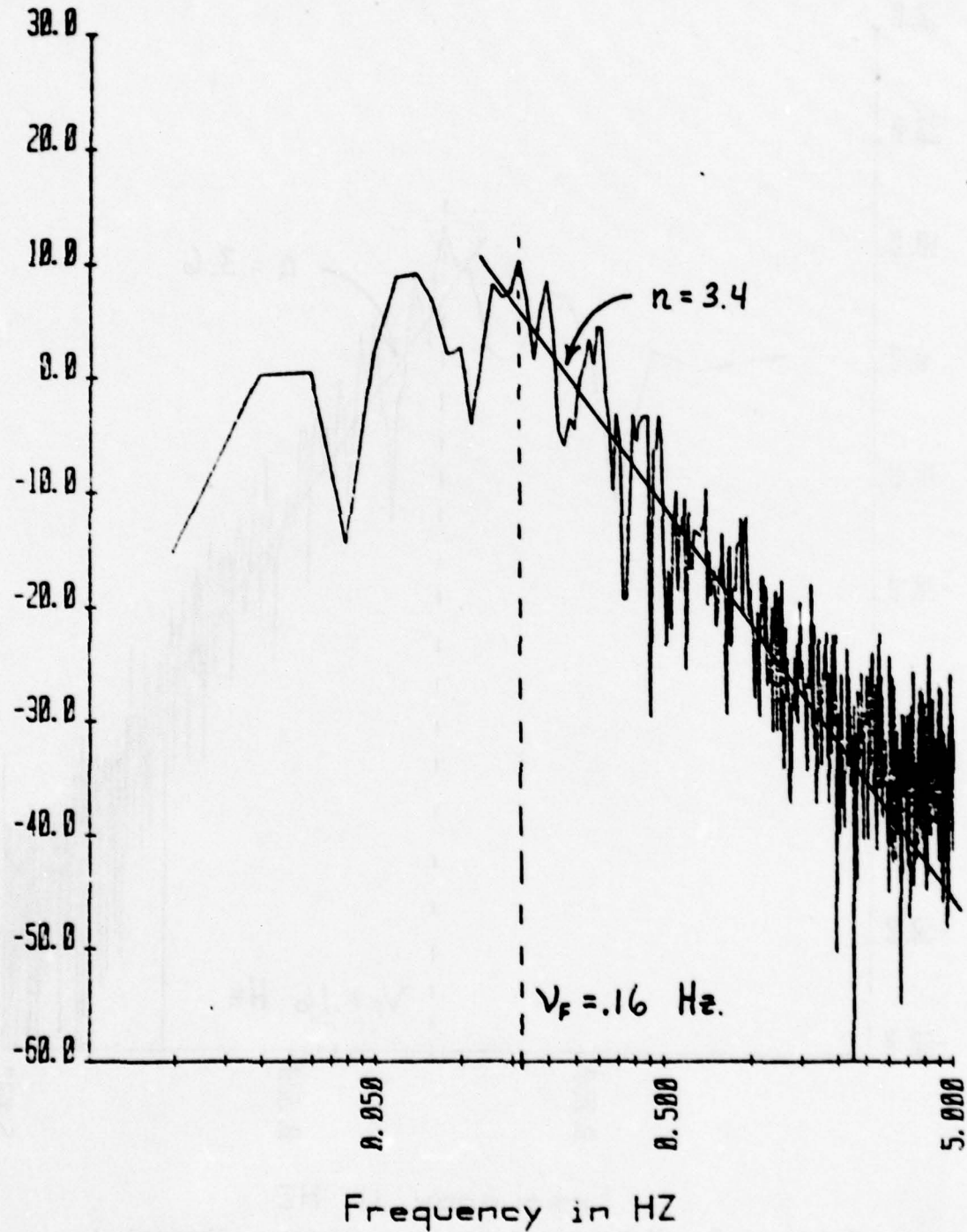
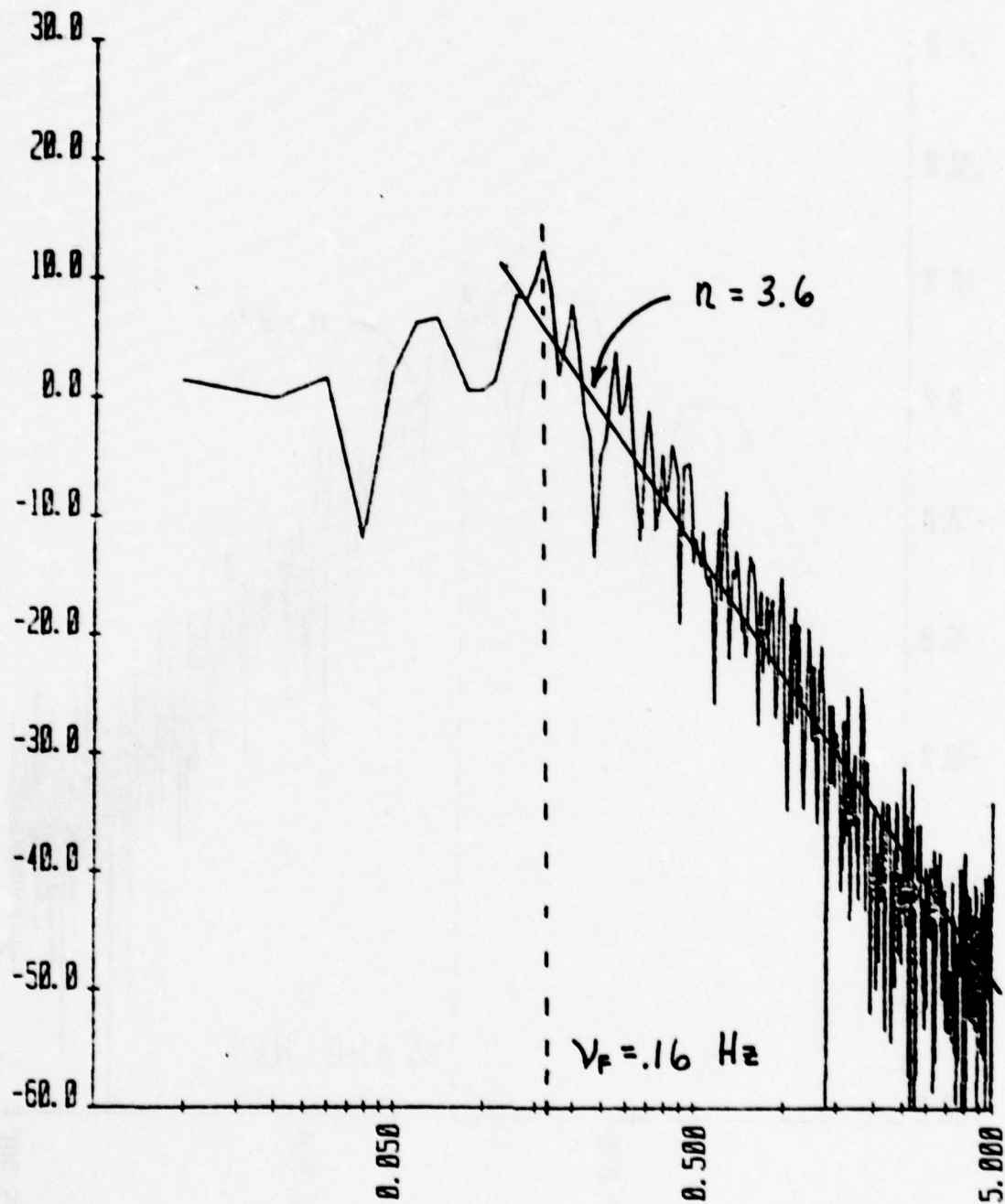


Figure 5.6. Normalized Power Spectrum - Channel 1.

NORMALIZED POWER SPECTRUM

Magnitude in DB



Frequency in HZ

Figure 5.7. Normalized Power Spectrum - Channel 2.

Force antenna has a higher gain and is located in a less noisy environment, the channel 2 signal is much less distorted. This can be seen by noting that the high frequency portion of the spectrum shown in Fig. 5.7 (channel 2) begins to flatten at a higher frequency than that shown in Fig. 5.6 (channel 1).

Using the relationships given by Rufenach (1972), the mean height of the irregularities can be easily determined, provided that the weak scatter theory is applicable. The mean height is given by

$$z = \frac{1}{\pi \lambda} \left(\frac{v_d}{v_F} \right)^2$$

where λ is the wavelength of the transmitted signal, v_d is the drift velocity of the frozen irregularity distribution, and v_F is the Fresnel frequency taken from the normalized power spectrum. For the two pieces of data, the mean height of the irregularities is computed to be 206.2 km. This height is much lower than we would expect. There are two reasonable explanations. The expression used in computing the mean height of the irregularities was derived for the case where scattering is weak. For the data the figures are based on, scintillation is moderately strong ($S_4 = .566$), and multiple scattering effects can no longer be considered negligible. Second, Umeki et al. (1977) have found that when scintillation is strong, broadening of the spectrum is expected. They have found that for cases involving multiple scattering the sharp break at the Fresnel frequency is

replaced by a gradual decrease in the spectral shape. Based on these findings it is possible that the true Fresnel frequency may be lower than visual inspection of the spectrum would suggest. For example, if the true Fresnel frequency was 25% lower than the spectrum would suggest, the mean height of the irregularities would be 366.6 km.

6. CONCLUSION

A data analysis scheme for studying the scintillation of transionospheric radio signals near the equator has been presented in this thesis. The first part of this scheme required that a digital system be designed. This digital interface circuit selectively samples the decoded scintillation data and then transfers the sampled values to an HP9825A desk calculator where they can later be analyzed. The operator is able to select the data channel that is to be sampled and then sample that channel at one of five different rates (20 Hz, 10 Hz, 4 Hz, 2 Hz, or 1 Hz).

The second part of this scheme requires that we be able to locate obvious errors that occur in the data and then apply appropriate correction techniques. These errors are often caused by data dropouts and noise. Full recovery from the error can not be accomplished. But, by using an error correcting scheme the error can be reduced in magnitude, so that it is small and has negligible effects on future data analysis.

Three sets of data were selected and analyzed in this thesis. Only one set of data was discussed in the results section. The three data sets were recorded in September 1977, between 00:00 UT and 01:30 UT, and are of 102.4 seconds length. The S_4 indices ranged from .148 to .725. Although channel 1 was noisier than channel 2 comparisons based on correlation and spectral analysis showed many similarities. The correlation interval, the time required for the correlation

to be reduced from 1 to 0, was about 2 seconds for all cases. Cross correlation of the two signals produced maximum values for displacements varying from 1.90 seconds to 3.10 seconds. Since the receivers were separated by 278 meters the frozen irregularity distribution had drift velocities that varied from 146 m/s to 90 m/s from west to east.

Comparison of the normalized power spectrums for each of the three data sets produced several interesting results. All of the spectra followed a power-law behavior for frequencies above the break point. For the three cases it was found that the Fresnel frequency, at which a break in spectral behavior occurs, increased when the S_4 index increased.

This is summarized below.

S_4 Index	Fresnel frequency (Hz.)
.164	.12
.567	.16
.725	.21

This thesis demonstrates the utility of a digital data analysis scheme which has been used to produce statistical properties of scintillating radio signals. The three sets of data analyzed in detail were selected in random and should not be construed as a trend nor interpreted in any geophysical significance. It is recommended that a more systematic analysis program can be carried out so that morphological studies can be carried out.

REFERENCES

- Brigham, E. O., (1974), The Fast Fourier Transform, Prentice-Hall, Inc., New Jersey.
- Mullen, J. P., Whitney, H. E., Basu, S., Bushby, A., Lanat, J., and Pantoja, J., (1977), Statistics of VHF and L-band Scintillation at Huancayo, Peru, J. Atmos. Terr. Phys., 39, 1251-1261.
- Rufenach, C. L., (1972), Power-law Wavenumber Spectrum Deduced from Ionospheric Scintillation Observations, J. Geophys. Res., 77, 4761-4772.
- Umeki, R., Liu, C. H., and Yeh, K. C., (1977), Multifrequency Spectra of Ionospheric Amplitude Scintillations, J. Geophys. Res., 82, 2752-2760.
- Yang, K. S. and Hearn, A. L., "A Multi-Channel Digital Data Logging System for Ionospheric Scintillation Studies", Ionosphere Radio Lab. Tech. Rep. 61, UIUC, July 1977.

APPENDIX

This appendix contains the computer analysis for two sets of equatorial scintillation data recorded on September 16, 1977 and September 28, 1977. The analysis includes computation of data autocorrelation, cross correlation, power spectrum and S_4 index.

SEPT 16 1977

Amplitude

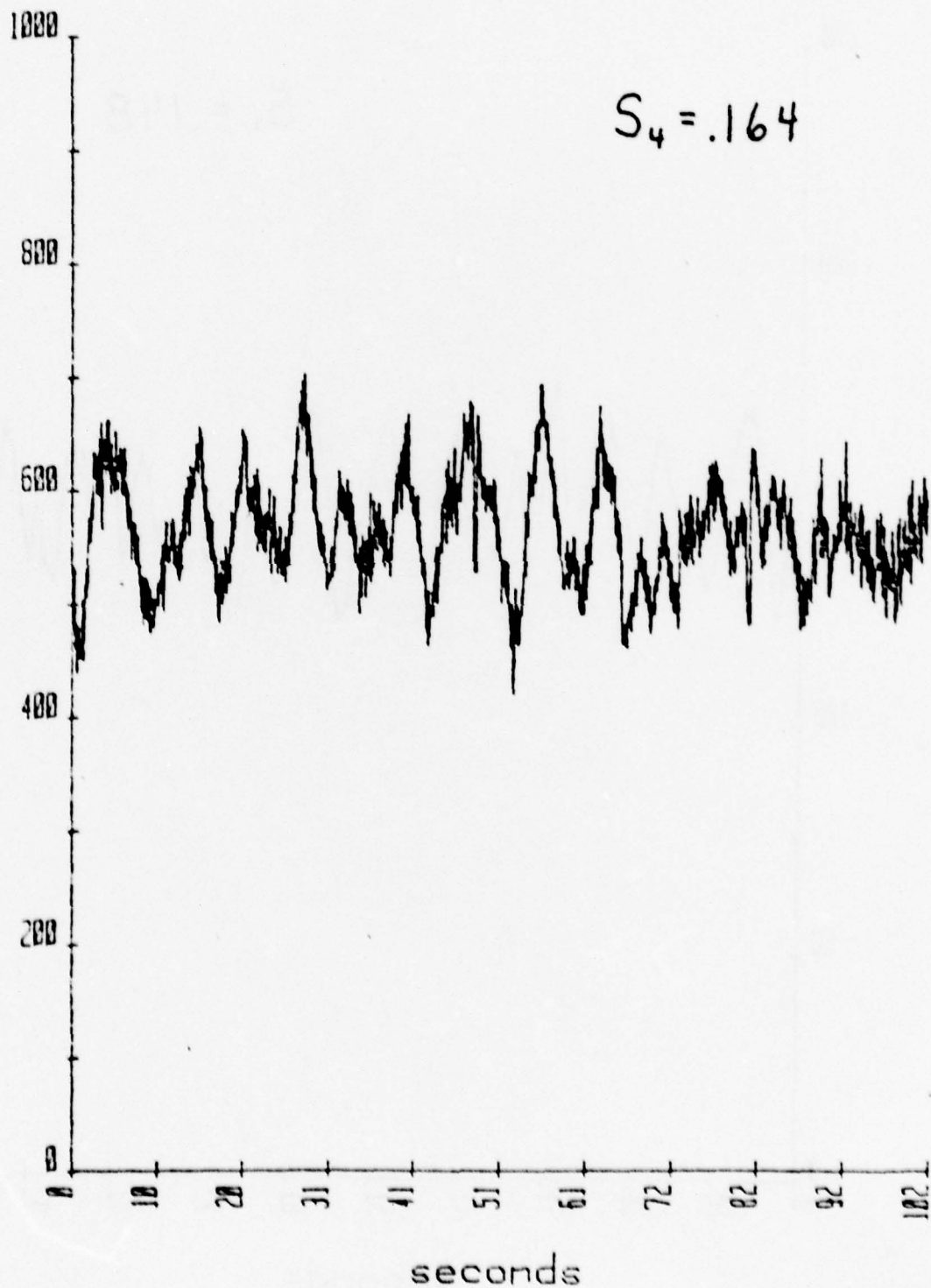


Figure A.1. Scintillation data - Channel 1 (00:18 UT).

SEPT 16 1977

Amplitude

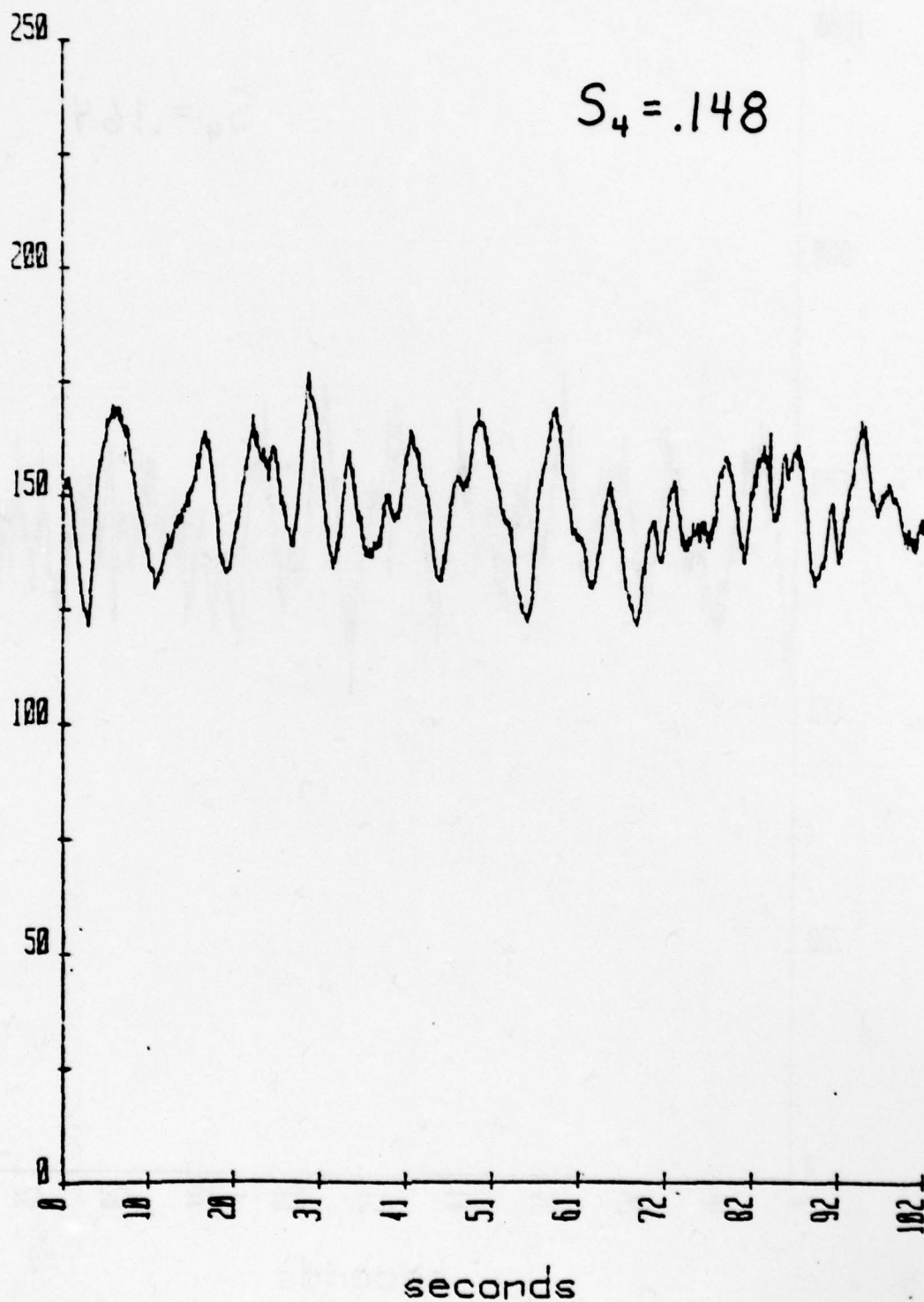


Figure A.2. Scintillation data - Channel 2 (00:18 UT).

SEPT 16 1977

Correlation

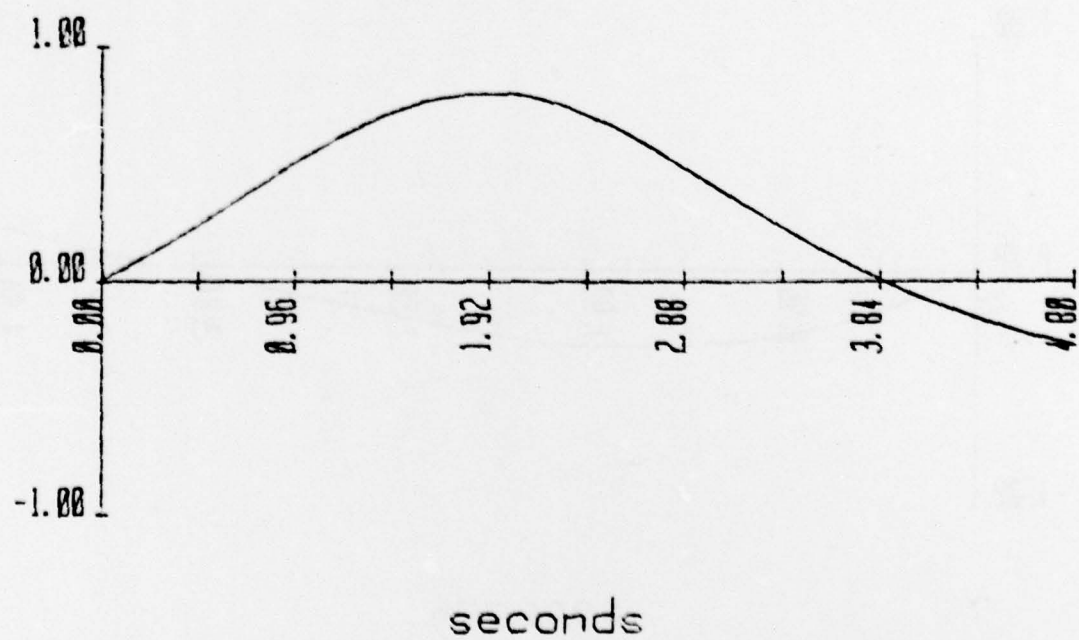


Figure A.3. Cross Correlation - Channel 1, Channel 2.

SEPT 16 1977

Correlation

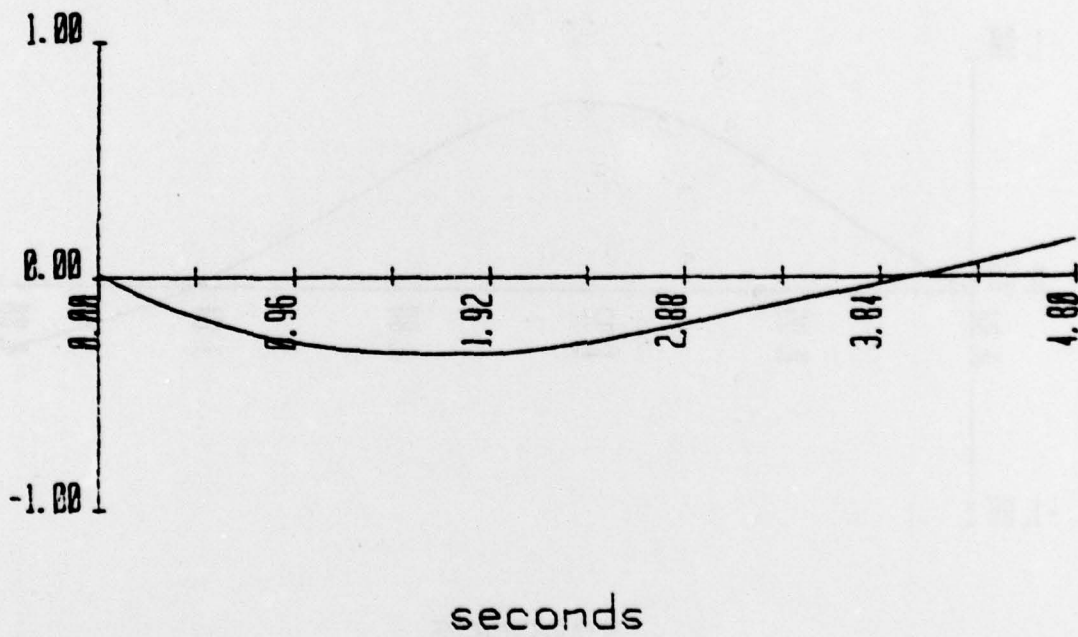


Figure A.4. Cross Correlation - Channel 2, Channel 1.

SEPT 16 1977

Correlation

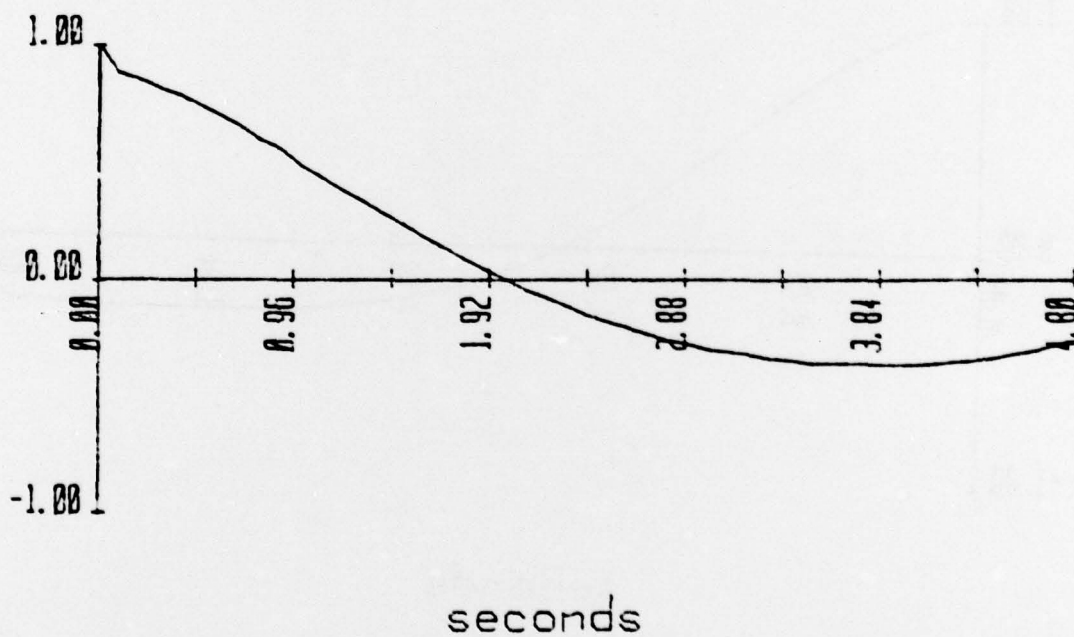


Figure A.5. Autocorrelation - Channel 1.

SEPT 16 1977

Correlation

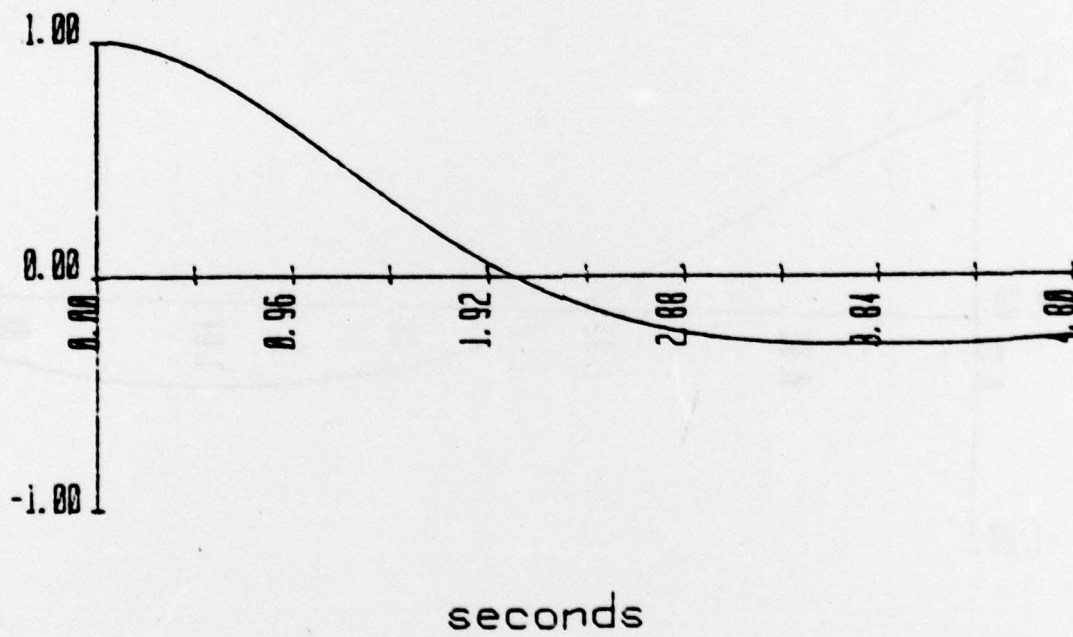


Figure A.6. Autocorrelation - Channel 2.

NORMALIZED POWER SPECTRUM

Magnitude in DB

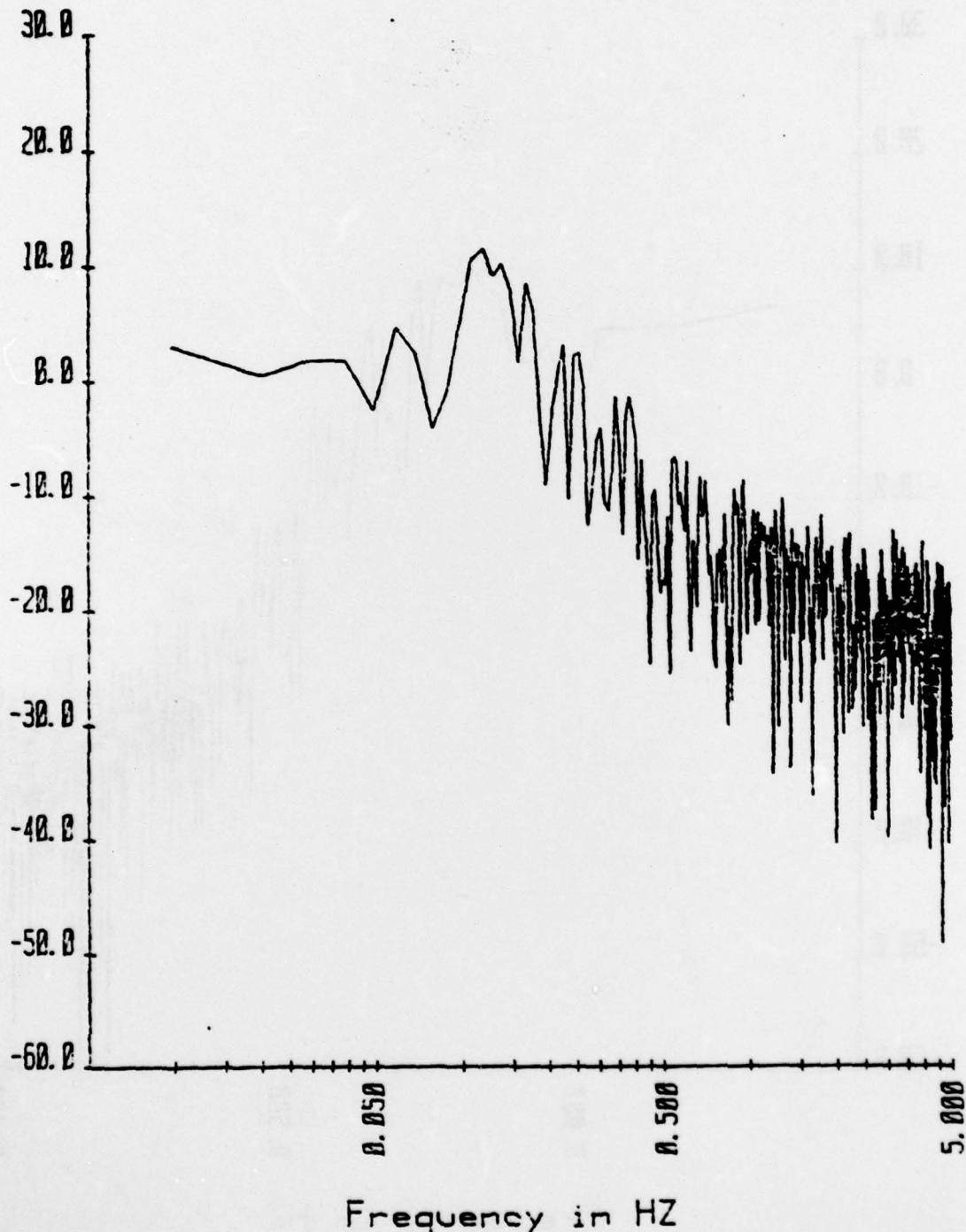


Figure A.7. Normalized Power Spectrum - Channel 1.

NORMALIZED POWER SPECTRUM

Magnitude in DB

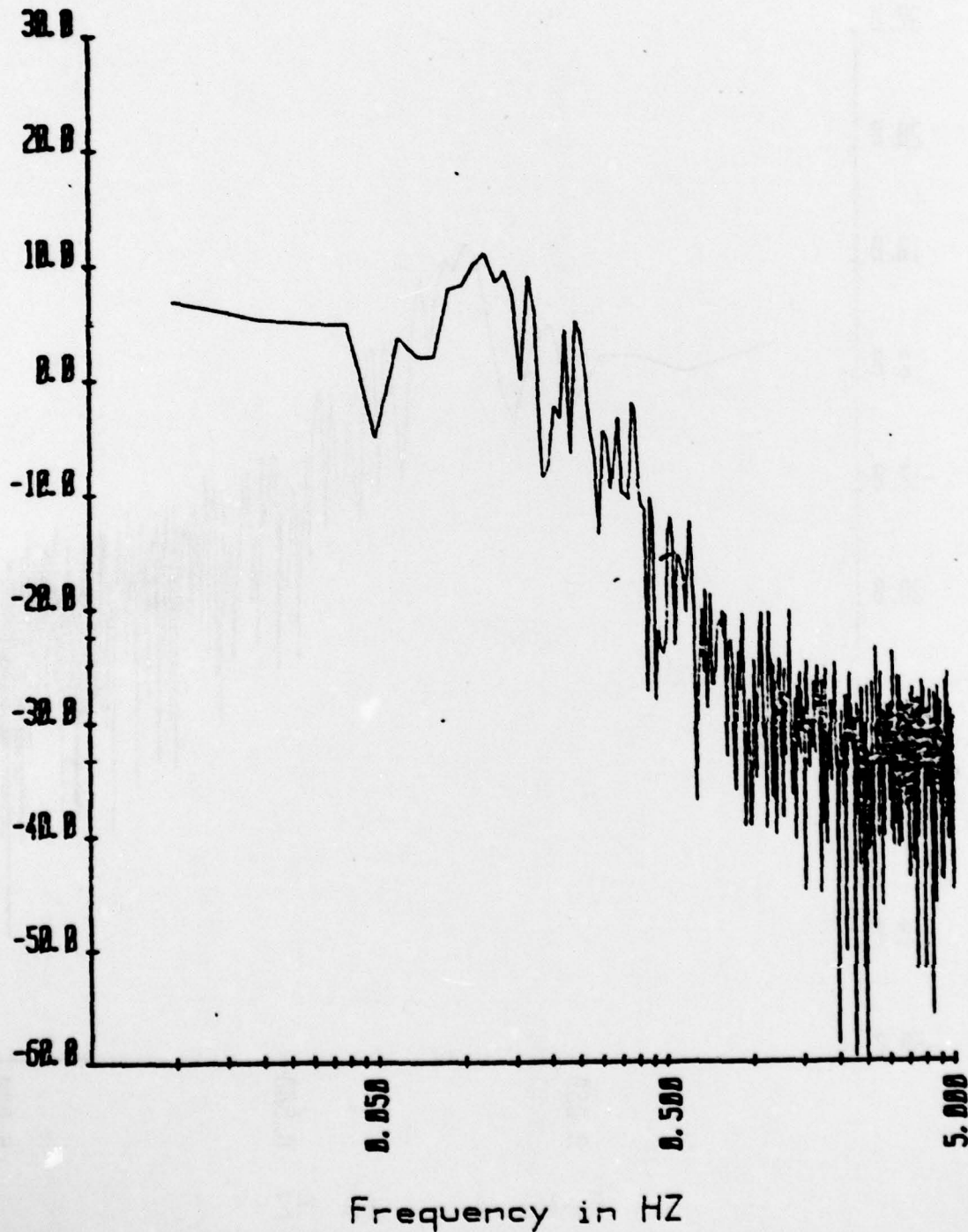


Figure A.8. Normalized Power Spectrum - Channel 2.

SEPT 28 1977

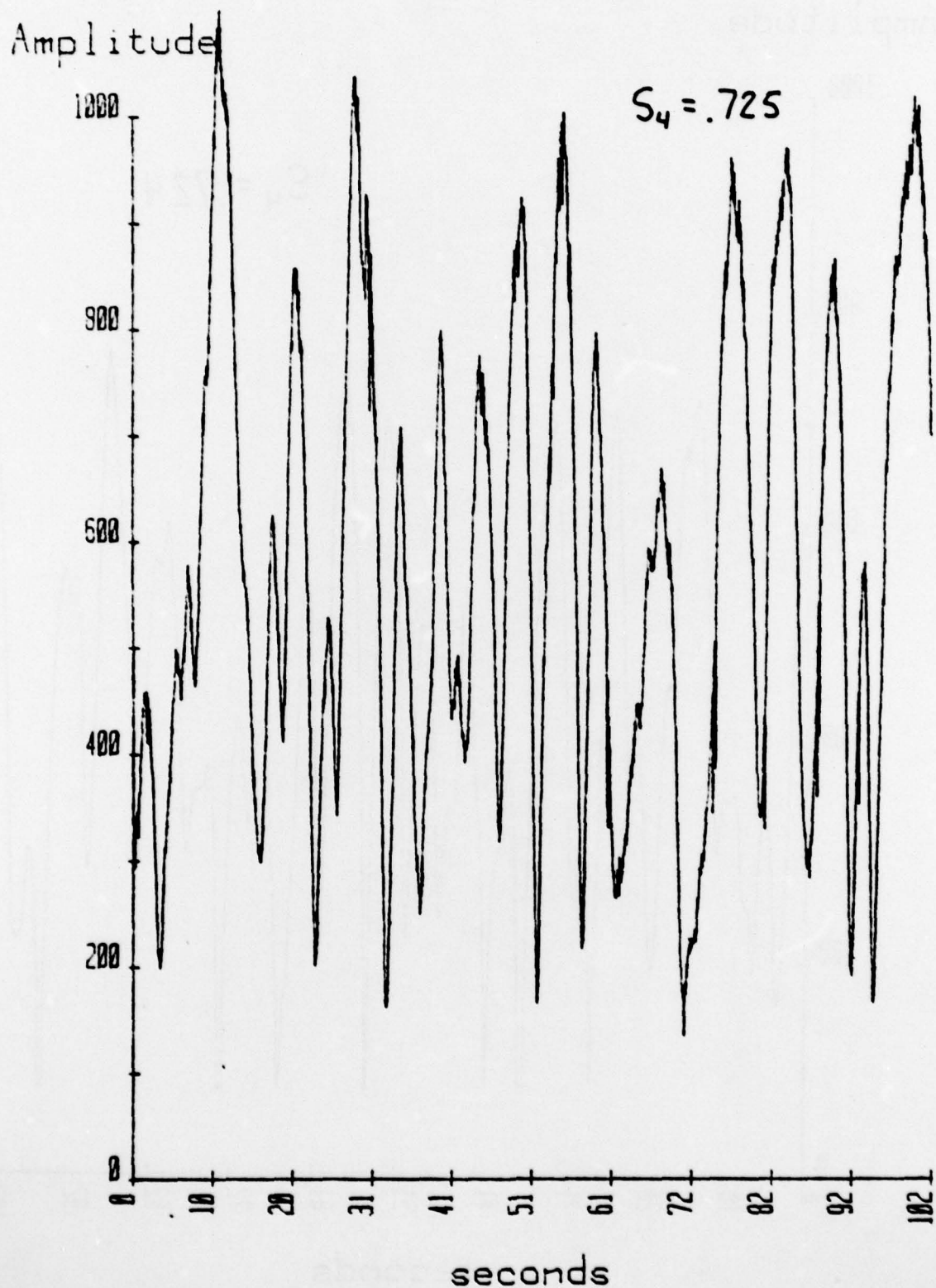


Figure A.9. Scintillation data - Channel 1 (01:22 UT).

SEPT 28 1977

Amplitude

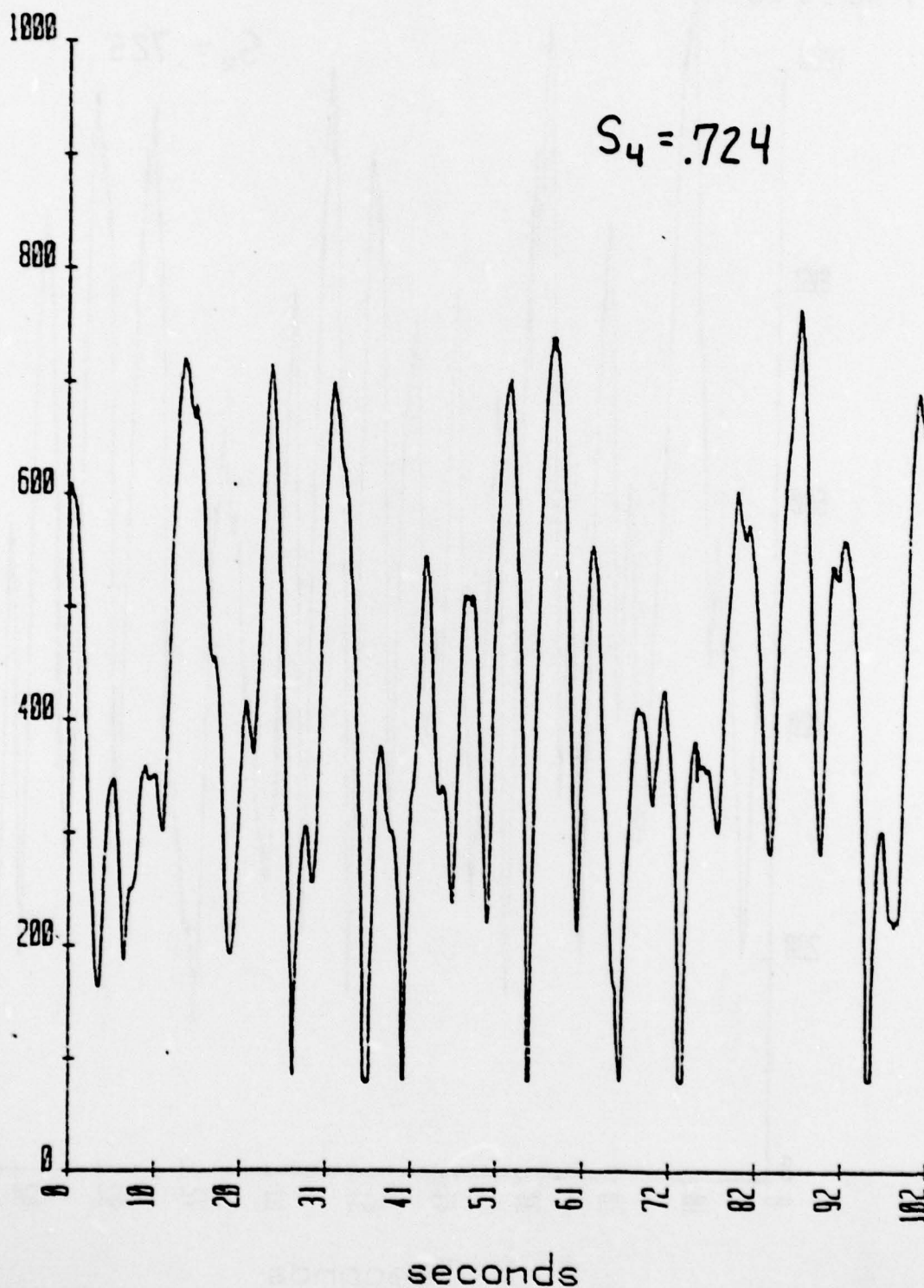


Figure A.10. Scintillation data - Channel 2 (01:22 UT).

SEPT 28 1977

Correlation

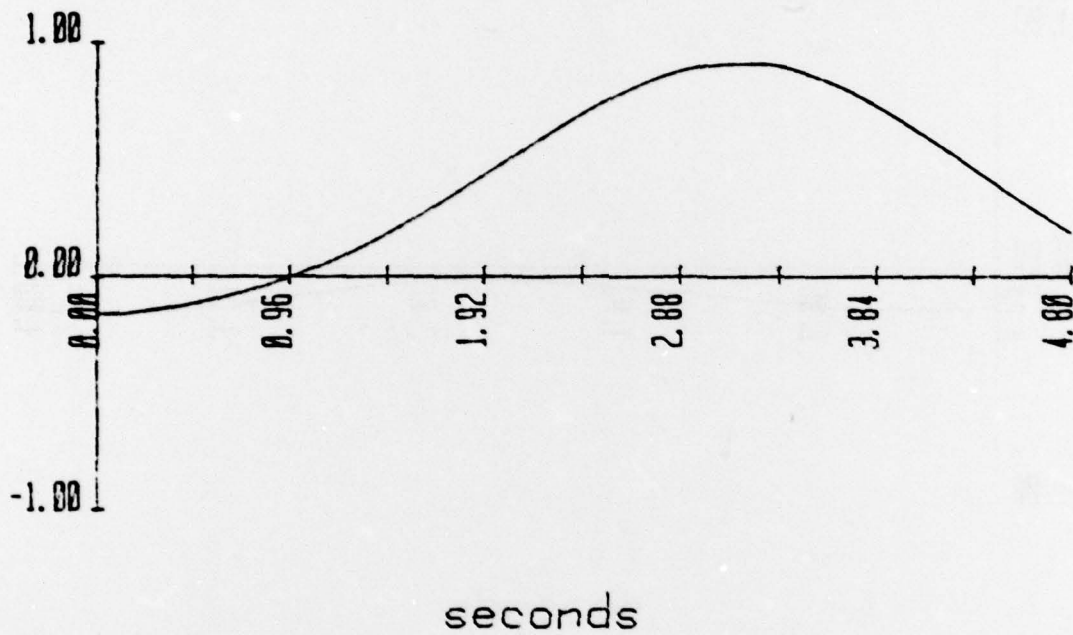


Figure A.11. Cross Correlation - Channel 1, Channel 2.

SEPT 28 1977

Correlation

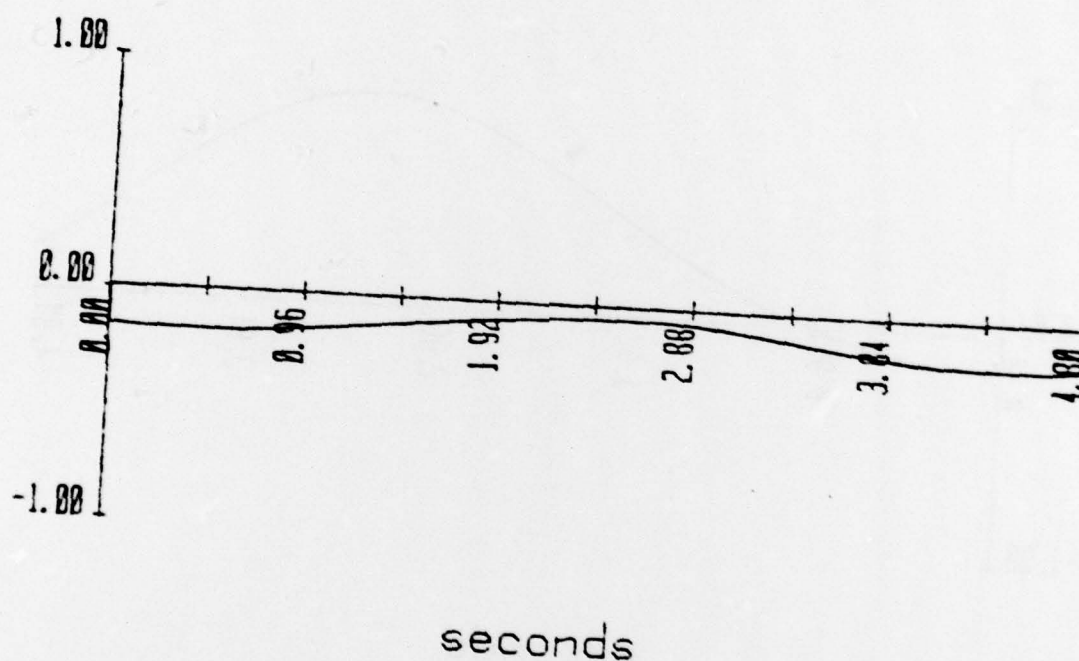
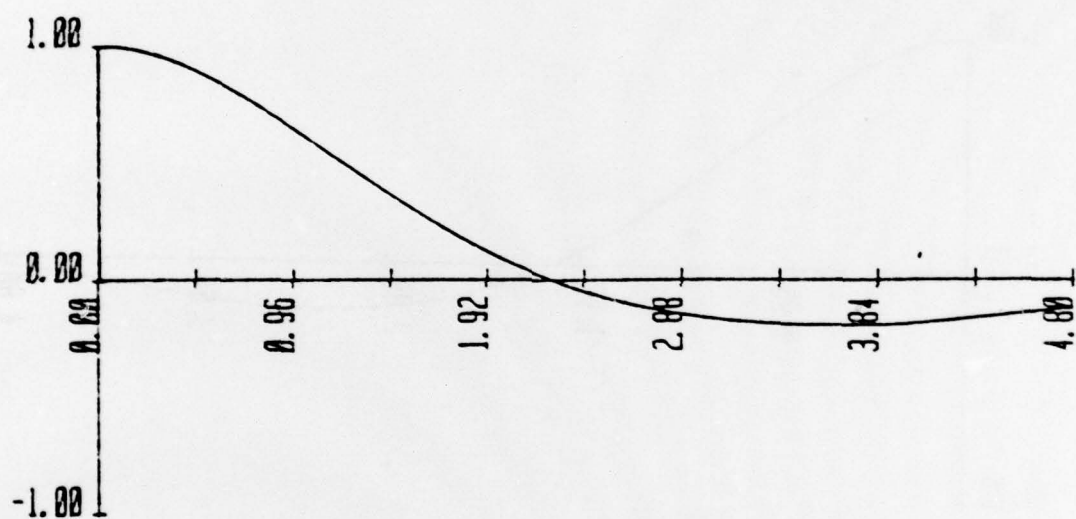


Figure A.12. Cross Correlation - Channel 2, Channel 1.

SEPT 28 1977

Correlation



seconds

Figure A.13. Autocorrelation - Channel 1.

SEPT 28 1977

Correlation

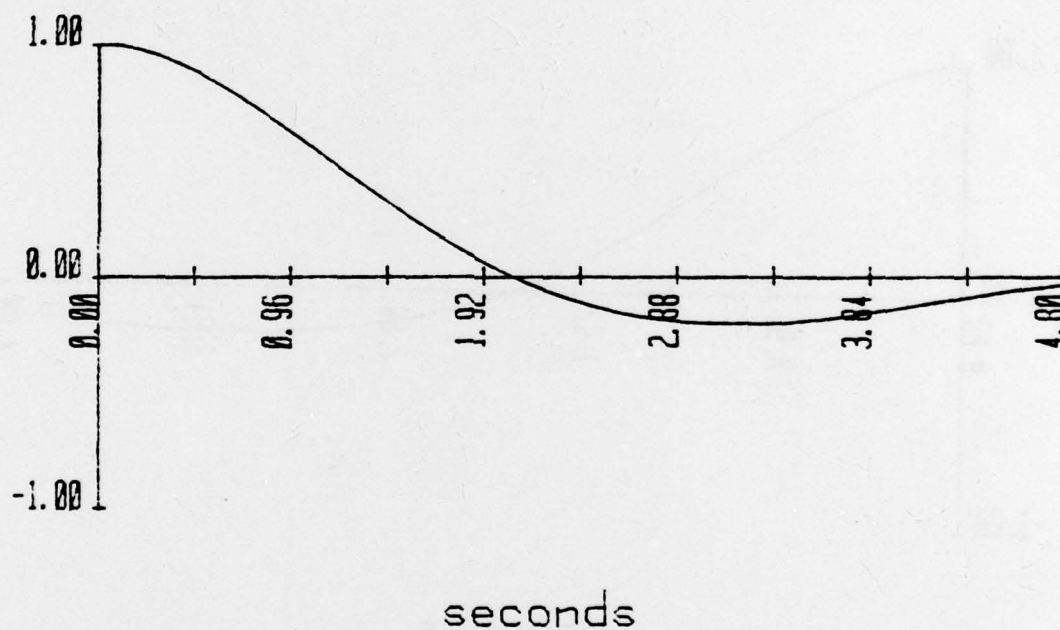


Figure A.14. Autocorrelation - Channel 2.

NORMALIZED POWER SPECTRUM

Magnitude in DB

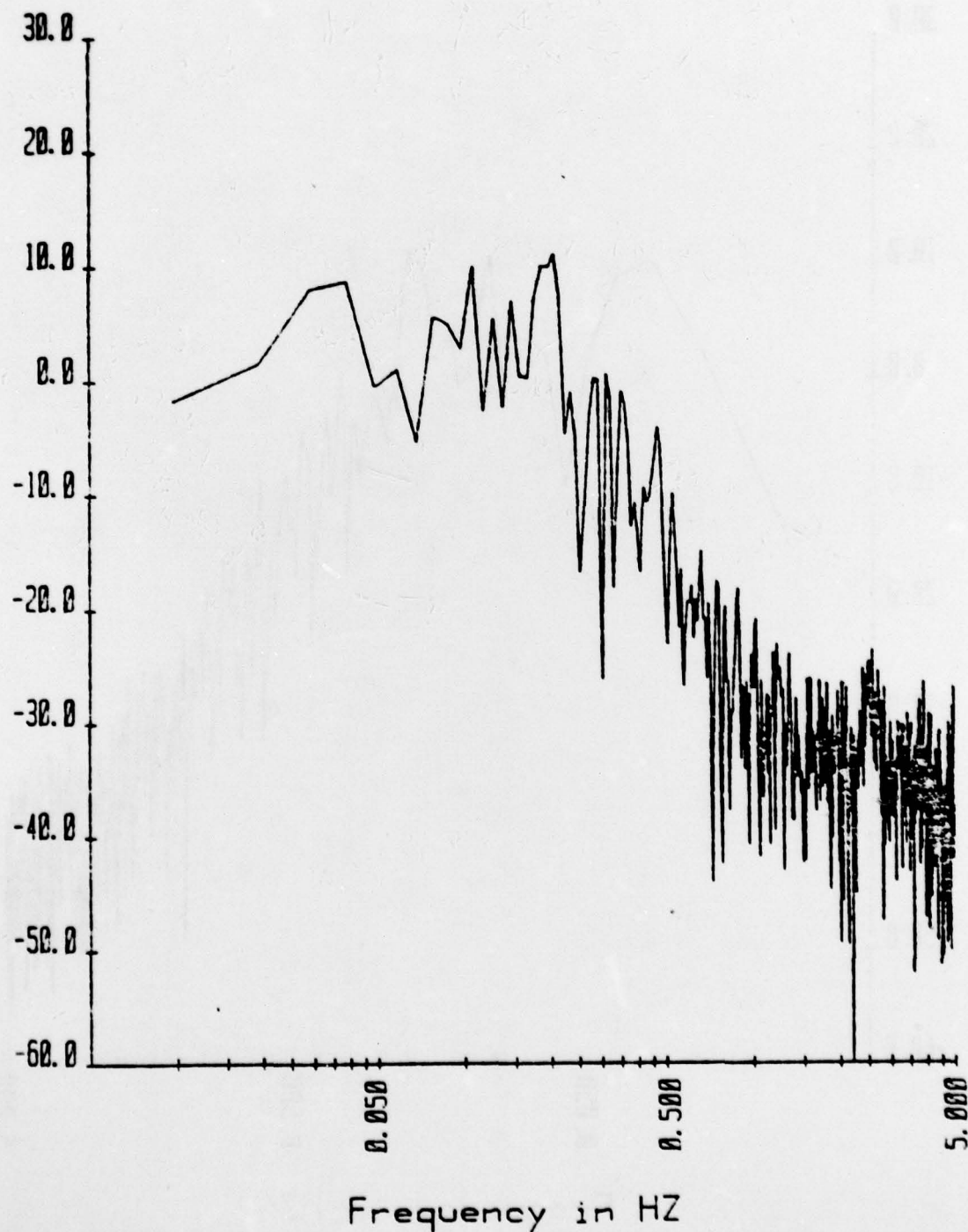


Figure A.15. Normalized Power Spectrum - Channel 1.

NORMALIZED POWER SPECTRUM

Magnitude in DB

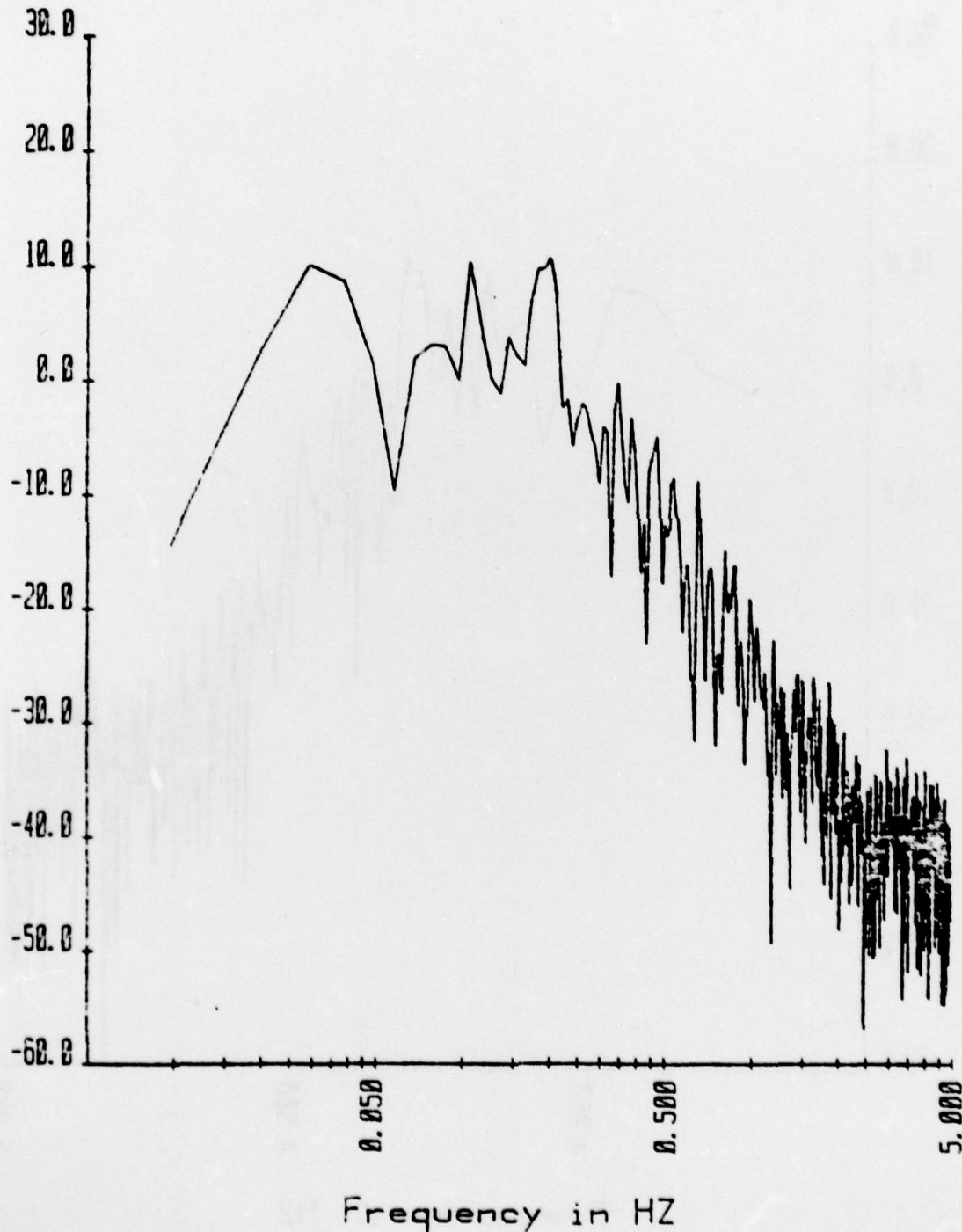


Figure A.16. Normalized Power Spectrum - Channel 2.